Numerical Modeling of Surface Chemistry Processes for Hypersonic Entry Environments

by

Abhilasha Anna

A dissertation submitted in partial fulfillment
of the requirements for the degree of
Doctor of Philosophy
(Aerospace Engineering)
in The University of Michigan
2013

Doctoral Committee:

Professor Iain D. Boyd, Chair
Assistant Professor Krzysztof J. Fidkowski
Assistant Professor Alexandre Martin, University of Kentucky
Professor Johannes W. Schwank

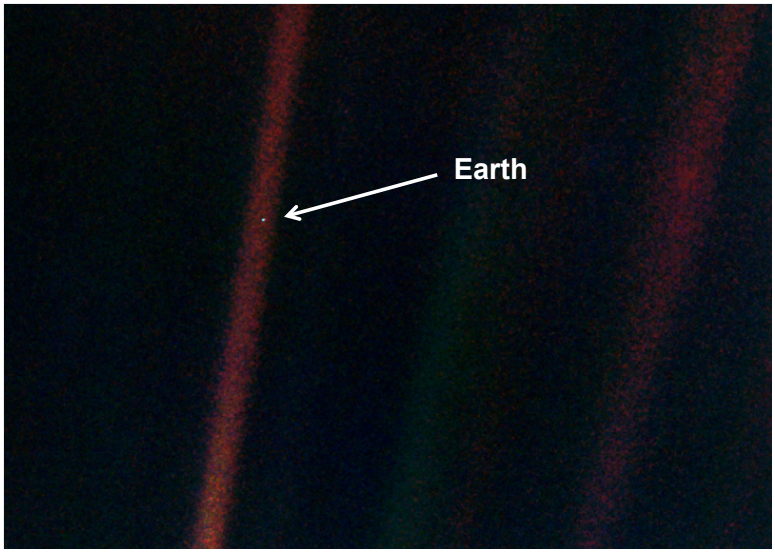

Photograph of planet Earth taken by the Voyager 1 spacecraft in 1990.
Credit: NASA/JPL

"Look again at that dot. That's here. That's home. That's us. On it everyone you love, everyone you know, everyone you ever heard of, every human being who ever was, lived out their lives.

Our posturings, our imagined self-importance, the delusion that we have some privileged position in the Universe, are challenged by this point of pale light. Our planet is a lonely speck in the great enveloping cosmic dark. In our obscurity, in all this vastness, there is no hint that help will come from elsewhere to save us from ourselves.

To me, it underscores our responsibility to deal more kindly with one another, and to preserve and cherish the pale blue dot, the only home we've ever known."

- Carl Sagan, Pale Blue Dot: A Vision of the Human Future in Space.

for Maa - Papa

ACKNOWLEDGEMENTS

I would like to express my sincere gratitude to the people with whose support the work presented in this dissertation was made possible and because of whom my experience in graduate school has been the one that I will cherish forever.

First and foremost, I am extremely grateful to my advisor, Iain Boyd for his exceptional guidance, encouragement and patience throughout my graduate studies at the University of Michigan. I am truly thankful for his immense support throughout these years and I believe I would have done something very good in my life to have the opportunity to work under his guidance. He is the most knowledgeable and kindest person I have met in my life. I would like to thank Professor Johannes Schwank, Professor Krzysztof Fidkowski, and Professor Alexandre Martin for their willingness to serve on my committee and for providing valuable feedback and guidance on my graduate research. I would especially like to thank Professor Douglas Fletcher and his two graduate students, Andrew Lutz and Walt Owens, at the University of Vermont for their tremendous support and the critical information they provided for this research work. I am truly grateful to Andrew Lutz for his immense help in providing information about the working of the experimental facility and the experiments without which it would have been difficult to perform my research work.

I would like to thank all the current members of the Nonequilibrium Gas and Plasma Dynamics Laboratory who have helped me with varied problems from solving bugs in the code to getting the printer working. I am grateful to our group member Jonathan Wiebenga for his help with my research. I would like to thank all my friends

here at the University of Michigan as well as those scattered around the world for making these five years of my life memorable. I am sincerely thankful to my friends who helped me stay sane through these difficult years. I would specially like to thank Hicham Alkandry for being a great friend, an awesome officemate and an extremely helpful lab mate. I would like to thank my officemate Frantisek Sobolic along with Hicham for the great discussions and hearty laughs that I enjoyed in the office. I would like to thank Andrew Crow who helped me through difficult times during graduate school and was always ready to watch an episode of Doctor Who with me whenever my brain needed distractions. Many thanks to my close friends Prasanna Amur Vardarajan, Harish Ganesh, Kringan Saha, Louis Tse, Nupur Maheshwari, Gunjan Upadhyay and Pragati Pandey for keeping my spirits high during graduate school. I am also thankful to our Graduate coordinator Denise Phelps of Aerospace Engineering at the University of Michigan for her support during my graduate study.

Most importantly, I would not have been able to accomplish any of this without the immense love and support of my parents. My maa and papa to whom this dissertation is dedicated have been the constant source of love, concern, strength and support throughout my life. I have been blessed with the most wonderful parents and would like express my deepest heart felt gratitude to them. In the end I am thankful to the Almighty for making all this possible.

I would like to gratefully acknowledge Air Force Office of Scientific Research (AFOSR) Grant FA-9550-11-1-0309 for supporting this work.

TABLE OF CONTENTS

LIST OF FIGURES

Figure

LIST OF TABLES

Table

NOMENCLATURE

D_k	Diffusion coefficient of species k [m^2/s]
E_{ad}	Energy barrier for adsorption, [J/mol]
E_{ER}	Energy barrier for Eley-Rideal recombination, [J/mol]
$\mathbf{J_{sp}}$	Species diffusion flux [$kg/m^2/s$]
k_b	Backward reaction rate, units vary
k_f	Forward reaction rate, units vary
K	Total number of species [dimensionless number]
$\dot{m}$	Mass blowing rate due to surface reactions, [$kg/m^2/s$]
M_k	Molar weight of species k [kg/mol]
N_{nb}	Number of bulk species [dimensionless number]
N_{sp}	Number of species in the mixture [dimensionless number]
N_R	Number of surface reactions [dimensionless number]
R_u	Universal gas constant [J/mol/K]
$\bar{\nu}_k$	Thermal speed of gas phase species k [m/s]
ν'_{ki}	Reactant stoichiometric coefficient for species k in reaction i [dimensionless number]
ν''_{ki}	Product stoichiometric coefficient for species k in reaction i [dimensionless number]
ν_s	Sum of the stoichiometric coefficients of all surface reactants [dimensionless number]
$\dot{w}$	Production rate [$moles/m^2/s$]

h_{sp}	Species enthalpy [J/kg]
k_B	Boltzmann constant
$\mathbf{q}$	Total heat flux [W/m^2]
$\mathbf{q_{conv}}$	Convective heat flux [W/m^2]
$\mathbf{q_{diff}}$	Diffusive heat flux [W/m^2]
S_0	Sticking coefficient [dimensionless number]
T	Translational-rotational temperature [K]
Y	Mass fraction [dimensionless number]
γ	Reaction efficiency [dimensionless number]
κ	Thermal conductivity [W/m/K]
ρ	Density [kg/m^3]
σ	Stefan-Boltzmann constant [W/m^2/K^{-4}]

subscripts

b	bulk phase
∞	reference freestream conditions
sp	species value
tr	translational-rotational energy mode
ve	vibrational-electronic energy mode
w	wall value

ABSTRACT

Numerical Modeling of Surface Chemistry Processes for Hypersonic Entry Environments

by

Abhilasha Anna

Chair: Professor Iain D. Boyd

The high temperatures on a hypersonic vehicle surface caused by heat loads encountered during entry through a planetary atmosphere require a reliable Thermal Protection System (TPS) that makes a good understanding of the physical and chemical processes essential for its design. TPS is a single point of failure system as the prolonged exposure to high temperature can cause the TPS materials to fail. Catalycity of an ablative TPS material and surface-participating reactions that lead to surface recession are key factors that impact the heating of the vehicle surface.

The major objective of this dissertation is to investigate surface chemistry processes (e.g. catalysis, nitridation) using coupled CFD-surface chemistry models. Another objective is to assess surface chemistry models using experimental data. The numerical simulations in this work are conducted using the computational fluid dynamics (CFD) code LeMANS developed at the University of Michigan. The investigation is performed using a finite rate surface chemistry model that incorporates the effects of surface catalysis as well as surface participating reactions. Experimental

data for flow and surface properties from tests conducted in the 30 kW Inductively Coupled Plasma Torch (ICP) Facility at the University of Vermont are used for the evaluations of the computations for different surface chemistry processes.

The effects of surface chemistry processes of a graphite sample exposed to a subsonic high-enthalpy nitrogen flow are investigated. The processes studied are the recombination of nitrogen atoms to molecules at the surface due to catalysis, and carbon nitridation where nitrogen atoms react with the surface carbon to form gaseous CN.

The results show a good agreement of the computations with all experimental measurements if all the flow, surface and material physics are included in the simulations. It is shown that the loss of nitrogen atoms observed in the experiment is caused by a combined effect of nitrogen recombination due to surface catalysis and the carbon nitridation reaction. It is revealed that true validation of the surface chemistry models requires absolute number density measurements. It is also determined that validation of such simulations requires better characterization of the power absorbed by the plasma in the ICP torch.

CHAPTER I

Introduction

Exploration of space has always intrigued mankind and its understanding has come a long way from Democritus proposing that the bright band in the night sky known to us as the *Milky Way* might be constituted of stars. The reasons for exploration have been different for different civilizations [3, 15]. The fundamental reasons for people in science are inspired by questions like "How did planetary systems and life originate?", "How do planets work?" and the eternal question "Are we alone?"

Carl Sagan once said [1], "*Since, in the long run, every planetary civilization will be endangered by impacts from space, every surviving civilization is obliged to become spacefaring–not because of exploratory or romantic zeal, but for the most practical reason imaginable: staying alive... If our long-term survival is at stake, we have a basic responsibility to our species to venture to other worlds.*"

History changed when Sputnik I, the world's first artificial satellite, was launched on October 4, 1957. Since then, an array of missions have been accomplished from the first human spaceflight in 1961 to landing the most advanced rover on Mars in 2012. With time, the missions have become more ambitious that in turn necessitates technological advances. Many of the space exploration missions can only be accomplished with atmospheric entry probes. For manned flights, hypersonic vehicles or capsules are used. Hypersonic conditions relate to speeds of more than five times the speed of

sound (i.e. Mach number > 5) [5]. The probes or vehicles enter the atmosphere of any planet at very high speeds that fall in the hypersonic regime. When a vehicle probe enters the atmosphere of any planet at hypersonic speeds, a bow shock is formed in its front. Figure 1.1 shows the various flow phenomena that occur during a high speed entry [102]. The temperature behind the shock is very high that causes dissociation of gaseous species behind the shock. The goal of this dissertation is to analyze surface chemistry processes. The flow features studied for the analysis of surface chemistry processes are surface recombination and ablation. These processes are explained in detail in Section1.1. Examples of the entry velocities of several probes and vehicles are shown in Fig. 1.2. When returning to Earth or when landing on another planet, a safe entry through the atmosphere is needed. The design of an entry probe or vehicle requires a detailed understanding of each of these flow features.

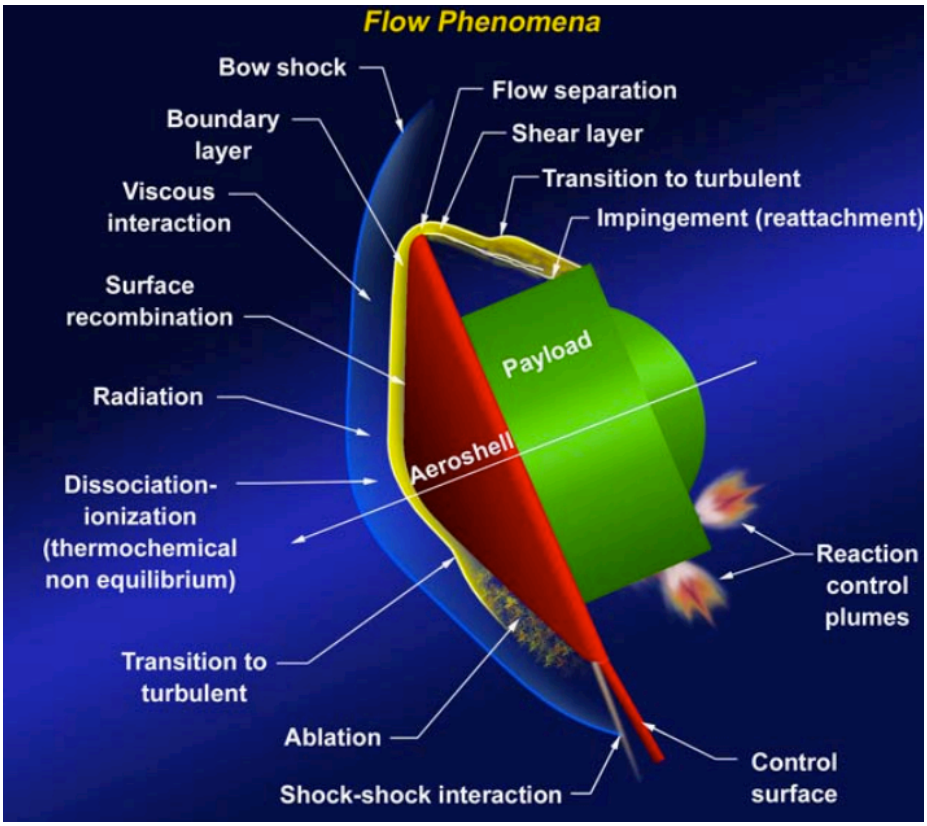

Figure 1.1: Various flow features for a high-speed entry [102].

The kinetic energy of the hypersonic flow is converted into internal energy of the gas that creates very high temperatures in the shock layer [5]. These temperatures are high enough to excite the vibrational energy mode within the molecules as well as cause dissociation chemistry. For air at 1 atm pressure, molecular oxygen, O_2, starts dissociating at 2000 K and is completely dissociated at 4000 K. Molecular nitrogen, N_2, starts dissociating at 4000 K and is completely dissociated at 9000 K. A hypersonic entry vehicle experiences excessive aerodynamic heat loads as a result of these high energy chemically reacting flows. An example of the entry conditions [100] along the flight trajectory for the Stardust sample return capsule is shown Table 1.1.

Table 1.1: Entry conditions along the estimated flight trajectory for Stardust [100].

Time from entry, s	Altitude, km	Velocity, m/s	Density, kg/m^3	Temperature, K	Pressure, N/m^2
34	81	12,385	1.3×10^{-5}	217	0.79
46	66	11,689	1.0×10^{-4}	227	6.87
56	57	9,617	3.8×10^{-4}	243	26.2
66	51	6,504	8.5×10^{-4}	255	62.7
76	46	4,007	1.5×10^{-3}	257	110.0
100	40	1,336	3.9×10^{-3}	244	273.0

The Stardust mission employed a sample return capsule (SRC) that was launched in February 1999 to retrieve samples of interstellar dust from the tail of comet Wild-2. Stardust returned to Earth in January 2006 with an atmospheric entry velocity of 12.8 km/s. It is the fastest Earth reentry and highest-energy reentry of any artificial vehicle to date. In Table 1.1, the time is set to 0 s when the capsule first entered the atmosphere at 120 km altitude [10]. The peak heat flux for this entry occurred at 51 s and the convective heat flux for this time point was 942 W/cm^2 at the stagnation point while the total heat load was 27.6 kJ/cm^2 [100]. Total heat load is the heat flux integrated over time. The temperature in the shock layer reaches approximately

30,000 K. One interesting feature to notice in this data is the variation in the velocity, density, temperature and pressure in just 60 s over a 40 km drop in altitude. This is an example of the challenging nature of the design of an entry vehicle or probe. It must be able to withstand this immense heat generated in a few seconds. To protect the entry probe or vehicle from these high heat loads, a heat shield called the Thermal Protection System is used and is described in the next section.

1.1 Thermal Protection System

The Thermal Protection System (TPS) provides insulation for an atmospheric entry probe or vehicle from the severe aerodynamic heat load encountered during hypersonic flight through a planetary atmosphere. It is a single point of failure system as the prolonged exposure to high temperature can cause the TPS materials to fail [60, 50]. The need to design a reliable TPS necessitates good understanding of the physical and chemical processes that determine the aerothermal heating environment.

Depending on the heat load encountered during hypersonic flight, an ablative or non-ablative TPS may be used [50]. Figure 1.2 shows an example of the mission trajectory and conditions suitable for non-ablative (reusable) and ablative TPS to be used effectively [46].

Non-ablative or reusable materials (e.g., ceramic tiles used on the Space Shuttle with a peak heating of 60 W/cm^2 [45]) are used where the re-entry conditions are relatively mild. In addition to the entry velocity, the heating is also dependent on the entry flight angle that is determined by the trajectory of the vehicle [69]. The entry flight angle is the angle between the local horizontal and the velocity vector. Steep entry angles cause high heating rates whereas shallow entry angles cause relatively low heating rates. The flight path angle for Space Shuttle entry was -1 degree [41]. The Space Shuttle had a glide re-entry where the flight path angle is shallow and thus experiences relatively lower peak heating at entry. There is no change in mass or

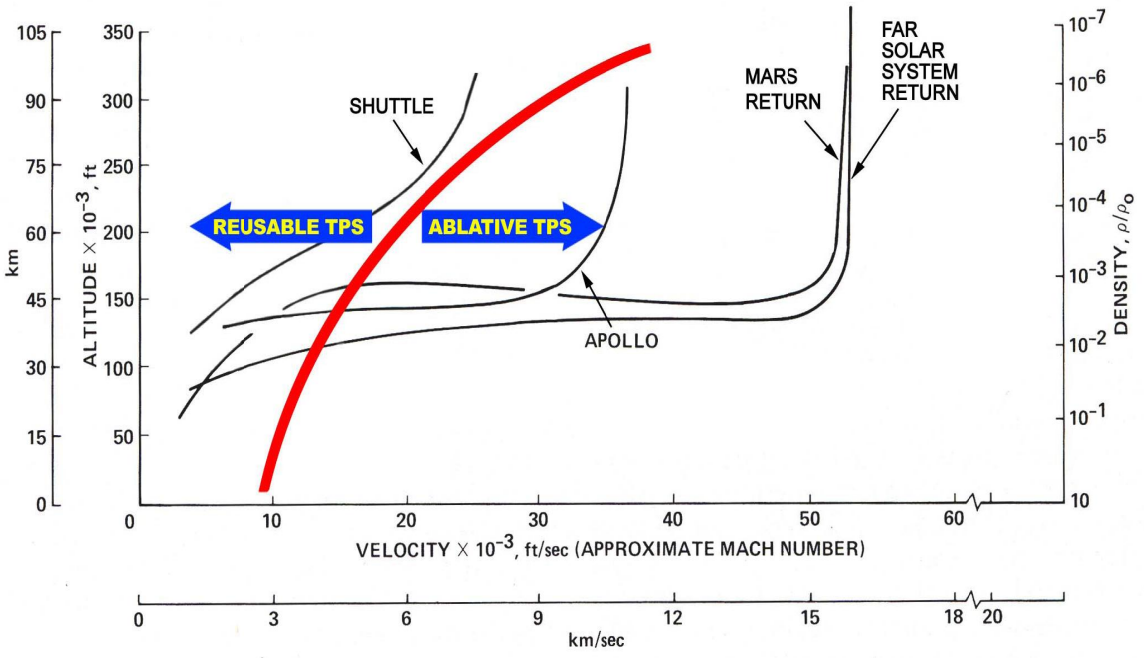

Figure 1.2: Conditions suitable for reusable and ablative TPS [46].

properties of the reusable TPS material when it is exposed to the entry environment conditions. An illustration of the features of a reusable TPS is shown in Fig. 1.3.

It can be seen that the net heat flux experienced by a reusable TPS is the balance of convective and radiative heat flux at the surface. A significant portion of the incident energy re-radiates from the heated surface and the remaining energy is conducted into the TPS material. For a reusable TPS, it is desirable that the surface coating has high emissivity that can increase the amount of re-radiated energy and a low catalytic surface to minimize the heating from recombination of dissociated boundary layer species. The inorganic insulation is also desired to have low thermal conductivity so that less material is required to protect the backup material. This approach will minimize the mass of the TPS.

An ablative TPS is used where relatively high heating rates are generated during reentry (e.g., the heat shield for the Stardust mission with a peak heating of 942 W/cm^2 [100]). The flight path angle for Stardust entry was -8.2 degree [29]. The

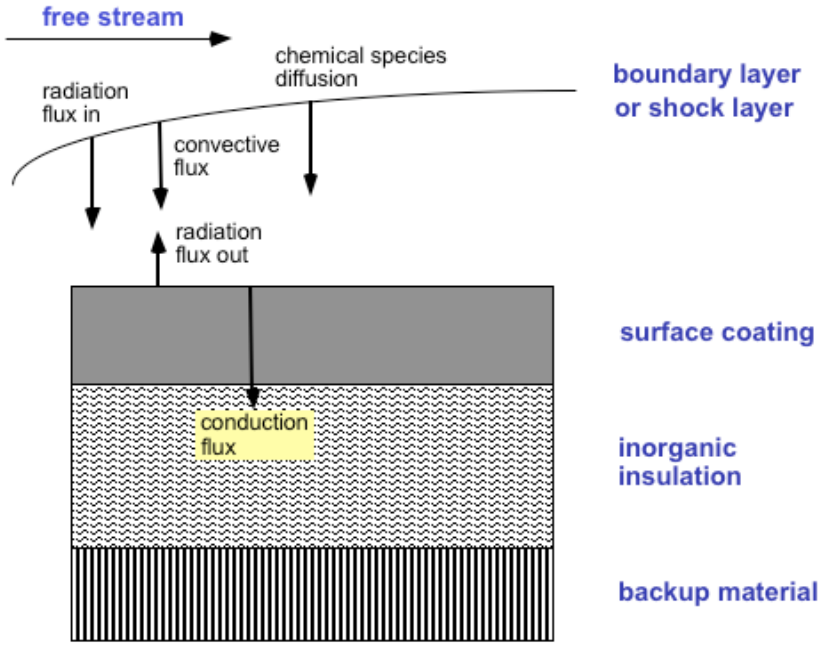

Figure 1.3: Features of a reusable TPS [50].

flight path angle is relatively steep for Stardust entry and thus experiences relatively high peak heating at entry. Ablative TPS materials accommodate high heating rates and heat loads through phase change and mass loss. The ablative material absorbs the heat and leaves the hypersonic vehicle as the material is consumed and ablates away. It is designed to slowly burn in a controlled manner. Ablative TPS has been used for most planetary entry probes and high velocity Earth atmosphere reentry vehicles including Stardust, Mars Science Laboratory, Apollo, etc.. An illustration of the features of a reusable TPS is shown in Fig. 1.4.

The total heat flux [37] imparted to an ablative TPS surface consists of: (1) convective heating as a result of gas particle collisions and their interactions with the surface, and (2) radiative heating as a result of radiation from excited particles in the flow. Ablative TPS materials are usually of two types, viz., pyrolyzing and non-pyrolyzing ablators. Pyrolyzing ablators (also referred to as charring ablators) are reinforced composites that have polymer resins as binders. Examples of charring

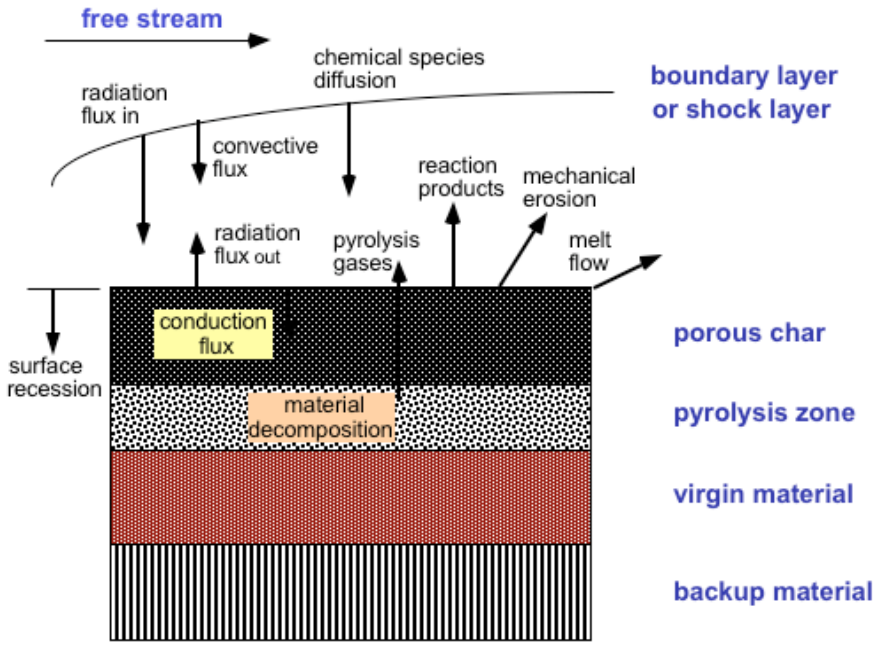

Figure 1.4: Features of an ablative TPS [50].

TPS materials are Phenolic Impregnated Carbon Ablator (PICA). Composite materials are composed of two or more materials that have significantly different physical or chemical properties. These materials when combined form a material that has different properties from the individual materials. The reinforcement material could be carbon, glass or organic polymers that can react with the flowfield gases. The surface is heated by hot gases convectively and from the radiant flux from the shock layer. The heat is either re-radiated out or conducted into the material. A high emittance surface is desirable for both ablative and reusable TPS to increase re-radiation as it is the most effective energy rejection mechanism [12]. It is the most efficient as the heat flux increases. When the material is heated, the resin pyrolyzes consequently that produces gaseous products. These gaseous products percolate through the material into the boundary layer. The carbon remains and the remaining layer is called the "char layer". The char layer acts as an insulator. The pyrolysis process is generally endothermic. The pyrolysis gases are heated and hence carry some energy from the solid to the gas. The gases may chemically react with the boundary layer gases and

effect the resultant heating. The pyrolysis gases that blow into the boundary layer thicken it and hence reduce convective heating.

Non-pyrolyzing ablators (also referred to as non-charring ablators) are those that withstand heat by losing mass only by surface ablation and mechanical erosion [67, 14]. Example of non-charring TPS materials are carbon-carbon and silica. Very high temperatures in the boundary layer may cause the molecular species to dissociate. The TPS material can act as a catalyst and if dissociated atoms diffuse to the surface, recombination of dissociated boundary layer species may occur which increases the convective heating to the surface. Thus, a less catalytic surface is desirable to minimize this additional heating. Also, when the vehicle surface is heated, the surface material may chemically react with the boundary layer gases leading to surface recession as a result of surface material consumption. These chemical reactions can be endothermic (vaporization, sublimation) or exothermic (oxidation, nitration) and will affect the net heating to the surface. Catalycity of an ablative TPS material and surface-participating reactions that lead to surface recession are key factors that impact the heating of the vehicle surface. It can be seen that an ablative TPS has a very complex physical and chemical interaction with the environmental gases in comparison to a reusable TPS. Therefore, detailed studies of these interactions that occur between the surface and the atmosphere gas are required for the accurate prediction of aerothermal heating of the vehicle TPS and in characterizing TPS materials.

1.1.1 History of ablative TPS

TPS is a key element in space exploration missions. These missions are pursued for finding answers to the fundamental questions of the origin of the solar system, origin of life, and the effect of the solar system on Earth. Exploration of the solar system and beyond requires both robotic and manned missions. TPS is required for the solar system objects that have an atmosphere. Both manned and sample return

missions require high-performance TPS. Figure 1.5 shows the composition of each planet along with the dwarf planet Pluto [27]. It also shows the atmospheric pressure and the entry speed of the hypersonic probe. Ablative TPS materials are made to accommodate the needs of a specific entry environment.

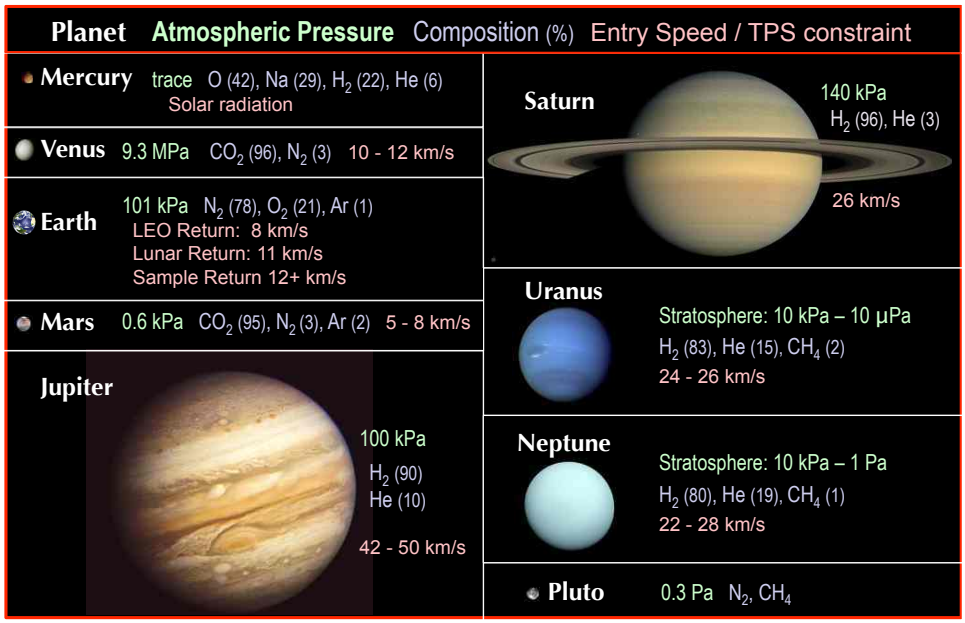

Figure 1.5: Composition of different planets with the respective entry speeds [27].

A few examples of earlier NASA missions that employed an ablative TPS are Apollo, Mars Viking, and Pioneer Venus. Apollo used Avcoat as the TPS. Avcoat is an epoxy-novalac resin reinforced with quartz fibers and phenolic micro balloons. Avcoat is applied in a honeycomb matrix that is bonded to a stainless steel substructure. Mars Viking used a Super Light weight Ablator (SLA) and Pioneer Venus used a carbon phenolic ablator. The TPS material is chosen in order for it to withstand the anticipated aerothermal environment for a specific mission. Figure 1.6 shows the peak heat flux experienced by various NASA entry missions along with the year of the mission. The respective ablative TPS used in each mission is also shown in the figure.

The development of newer ablative materials declined after the Mars Viking Mis-

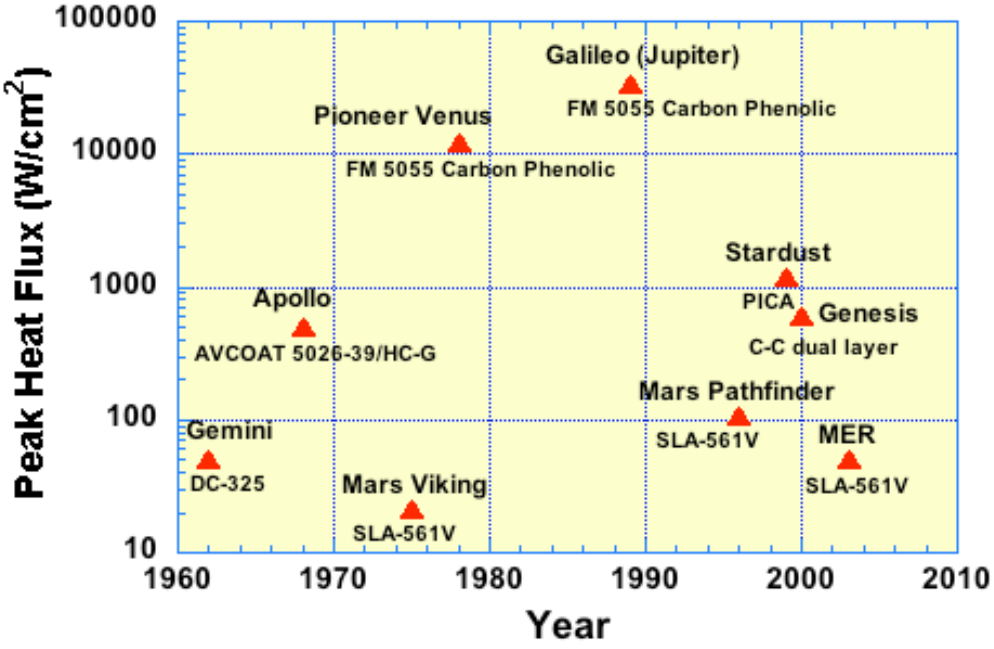

Figure 1.6: Peak heat flux for NASA entry missions [50].

sion due to interest in the development of reusable TPS for Space Shuttle [50]. New ablators were developed for the Stardust and Genesis missions as the existing TPS materials were incapable of fulfilling the mission requirements. Stardust used a light weight ablator PICA that stands for Phenolic Impregnated Carbon Ablator. The most recent Mars exploratory mission MSL (Mars Science Laboratory) also employed PICA as the heat shield. It was launched by NASA in November 2011 and entered the Martian atmosphere in August 2012 with an entry velocity of 5.9 km/s. Genesis was a sample return probe that employed ACC as the heat shield. ACC is an Advanced Carbon Carbon multilayer TPS.

Ablative TPS materials are generally classified by density viz. low, medium and high density. The higher the density, the better the strength. However, the thermal conductivity of the material also increases with density. Therefore, for a modest TPS mass fraction, it is important to optimize between ablation and insulation efficiency. The TPS mass fraction is the fraction of the mass of the entry probe that is devoted to the TPS. Figure 1.7 shows a plot of TPS mass fraction against total heat load for

various entry missions using ablative TPS. The blue solid line in this figure is a curve fit of TPS mass faction with the total heat load. It can be seen that the TPS mass fraction is a strong function of the total heat load rather than the peak heat flux. Peak heat flux is the deciding factor in selecting the TPS material that can sustain the desired level of heating. Integrated heat load is the key factor in determining the required thickness of the TPS [34].

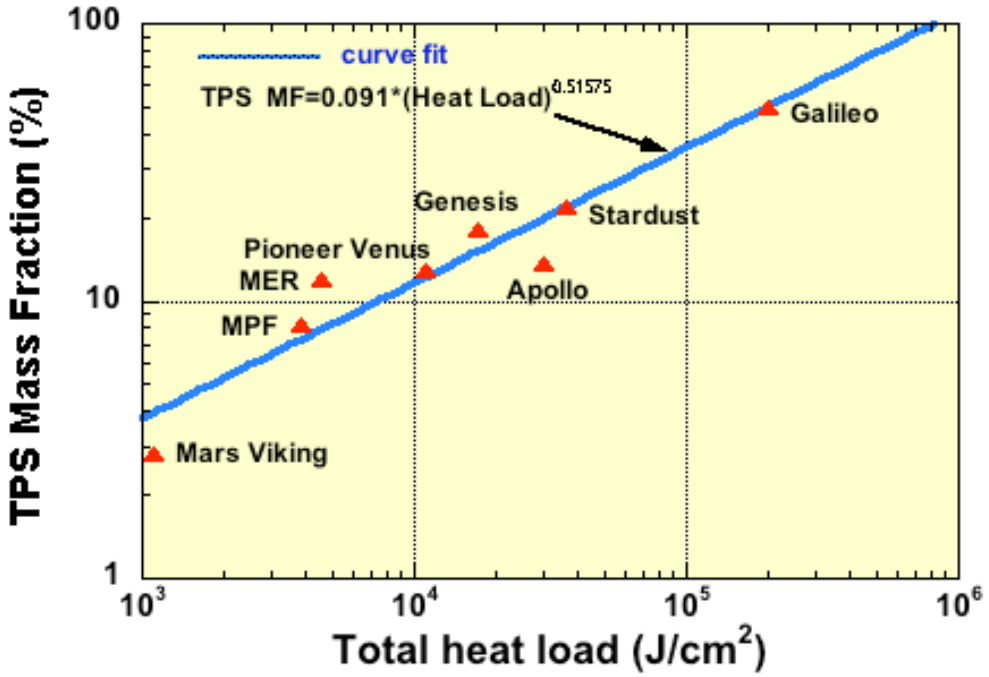

Figure 1.7: TPS mass fraction against total heat load for entry missions using ablative TPS [50].

As seen in Fig. 1.7, the Galileo probe to Jupiter used 50% TPS mass fraction. The probe entered the Jovian atmosphere at a velocity of approximately 47.4 km/s. It had a fully dense carbon phenolic TPS. It is one of the most challenging entry missions with a peak heating of 35 kW/m^2 and a total heat load of 200 kJ/cm^2 [50]. Galileo had ablation sensors installed in the forebody heat shield and Fig. 1.8 shows the heat shield before and after entry. It can be seen from this picture that the stagnation point recession of the TPS is less than the predicted value but the shoulder ablation is greater than the predicted value. A margin thickness was added to the final design.

It is an example of the dependence of a mission on the TPS performance. If the TPS fails to withstand the required peak heat flux and the total heat load, the entire mission will be compromised. One challenge for future missions is the mass fraction of the TPS. Based on the ablation data, the TPS mass fraction for carbon phenolic would probably be more than 50%. If a more ambitious mission is desired with even higher entry velocities, the TPS mass fraction would be even higher. It would leave very little mass for the actual science mission. PICA and Avcoat are not capable for Jovian entry conditions. Therefore, development of new advanced TPS materials is required.

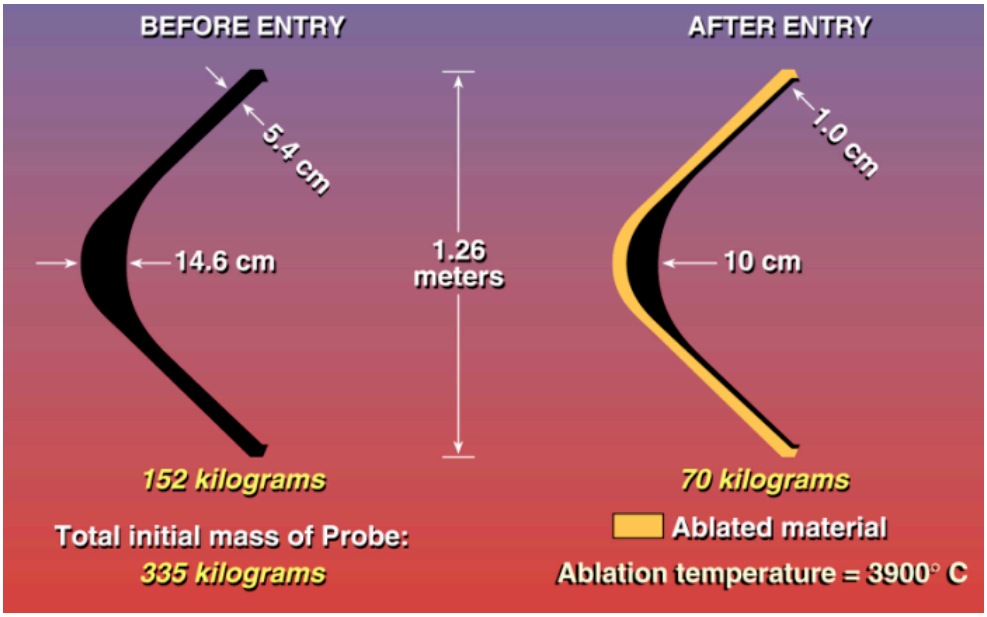

Figure 1.8: Galileo probe heat shield before and after entry into the Jovian atmosphere [50].

Figure 1.9 provides some current TPS materials for forebody heat shield with their entry environment capabilities along with applicability for potential missions. A "fully capable" status means that the material has been successfully employed for actual entry conditions. A status of "potentially capable and qualification needed"

Density	Forebody heat shield	Flight qualified	Heat flux limit, W/cm^2	Pressure limit, atm	Entry velocity, km/s		Potential missions
					< 13	> 13	
Low – Mild	PICA	Stardust, MSL	~ 1200	< 1	●	◔	Sample return, Mars
	Avcoat	Apollo	~ 1000	< 1	●	✖	Venus
	ACC	Genesis	> 2000	> 1	◔	◔	Sample return, Mars
High	Heritage Carbon phenolic	Venus, Jupiter	10,000 – 30,000	>> 1	■	■	Sample return, Venus, Jupiter, Saturn
● Fully capable ◔ Potentially capable, qual needed ■ Capable but heavy ✖ Not capable							

Figure 1.9: Current TPS materials for forebody heat shield and their capability [50].

means that the material has the capability to be employed for the respective entry conditions but its performance needs to be verified through testing in experimental facilities. It needs to be tested over a range of desired heat flux, shear and pressure conditions. A "capable but heavy" status implies that the material has the capability but is prohibitively heavy for a realistic science mission. "Not capable" status implies the material is not suited for the desired entry conditions. It can be stated now that for future missions of space exploration, development and characterization of new TPS materials is necessary. After discussing the need of developing new TPS, the following section presents the existing methods used to characterize and qualify the material for heat shields.

1.1.2 Ground testing

The two important aspects in the development of thermal protection systems are the ground test facilities and the computational models. Flight testing is the best way to fully validate the performance of a full-scale thermal protection system. However, such tests have exceedingly high costs and could only be used (if performed at all) not to learn anything new but to validate the performance of the TPS [107].

The major ground testing facilities are arc jets and inductively coupled plasma (ICP) facilities. Examples of other facilities [101, 50, 88] that could be used are high energy laser facilities, shock tubes and arc heaters. Arcjet facilities are considered to provide the best method of simulating a flight environment for a TPS [102]. Arcjet facilities simulate supersonic, high enthalpy flow conditions. An arc jet uses an electric arc to increase the enthalpy of the gas [79]. The hot gas expands through a conical, converging diverging nozzle at supersonic speeds. Examples of these facilities are the Aerodynamic Heating Facility (AHF) and Interaction Heating Facility (IHF) at NASA Ames Research Center (ARC) and the Arc Jet Complex at the NASA Johnson Space Center (JSC). Although these facilities can create supersonic flow conditions, they have their limitations. These arc jet facilities do not have the capability to operate with a variety of gases, e.g. hydrogen and helium. This poses a problem for testing of TPS materials for atmospheric compositions other than air (as shown in Fig. 1.5). The maximum heating is limited to approximately 2.5 kW/cm^2 which is much less than the peak heat fluxes predicted for some of the future missions. Also, particles eroded from the electrodes can be present as contaminants in the flow stream. The contaminants may affect the chemical processes in the flow stream and in the boundary layer around the test article.

The ICP torch facility is designed to test scaled material samples in high enthalpy gas flows for simulation of planetary atmosphere entry trajectory heating conditions. It is configured for operation with subsonic plasma flow that represents the region behind a normal shock. It helps to study the thermochemical effects of the shock layer plasma on the TPS material. The facility test conditions can be extrapolated to flight conditions by matching three parameters at the edge of the boundary layer, i.e. the enthalpy, the stagnation pressure and the velocity gradient. The stagnation point heat flux in the flight is equal to that in ground tests if these parameters are equal [49]. ICP facilities were developed in the US and Europe in the 1960s [88].

These facilities were also extensively developed and used in Russia and are now also in operation in Europe and Asia [60]. Examples of these facilities are the 30 kW ICP torch at the University of Vermont (UVM), 15 kW and 1.2 MW torches at the Von Karman Institute (VKI), and the 100 kW torch at the Institute for Problems of Mechanics [88, 71]. ICP facilities are electrode-less and hence contamination from electrode materials is not present [60]. ICP facilities are relatively less expensive to operate. They can be used for various gases and are thus appropriate for simulating different atmospheric compositions.

High energy laser facilities can be used to test heat flux failure modes of TPS materials [101]. The drawback with these facilities is that the pressure, flow and chemistry conditions produced are not flight environment relevant. Shock tubes could also be used to simulate high enthalpy shock layer conditions. An example of this facility is the electric arc-driven shock tube (EAST) facility at NASA Ames [42].

The current ground test facilities can not simulate all environmental entry conditions simultaneously. For example, the scale, pressure, aerodynamic shear, heat flux and enthalpy experienced in the flight cannot be recreated simultaneously in an arc jet. Arc jet testing is relatively more expensive than the other available testing techniques. An example of the limitations of arc jets is shown in Fig. 1.10, where the stagnation point heat flux and pressure for the various arc jet capabilities are plotted along with the respective values for Saturn, Titan and sample return missions. In addition to arc jets, the stagnation point heat flux and pressure range of UVM ICP torch facility is also shown in this figure.

It can be seen that some of the conditions for sample return and Saturn missions can not be met in these arc jets. The facilities shown in the figure are AHF, IHF, JSC TP1 and TP2, Boeing Large Core Arc Tunnel (LCAT), USAF Arnold Engineering Development Center (AEDC) H2 Tunnel and the Italian CIRA/Scirocco facility [99, 58, 47, 87, 35]. It should be noted that these facilities can not be operated with

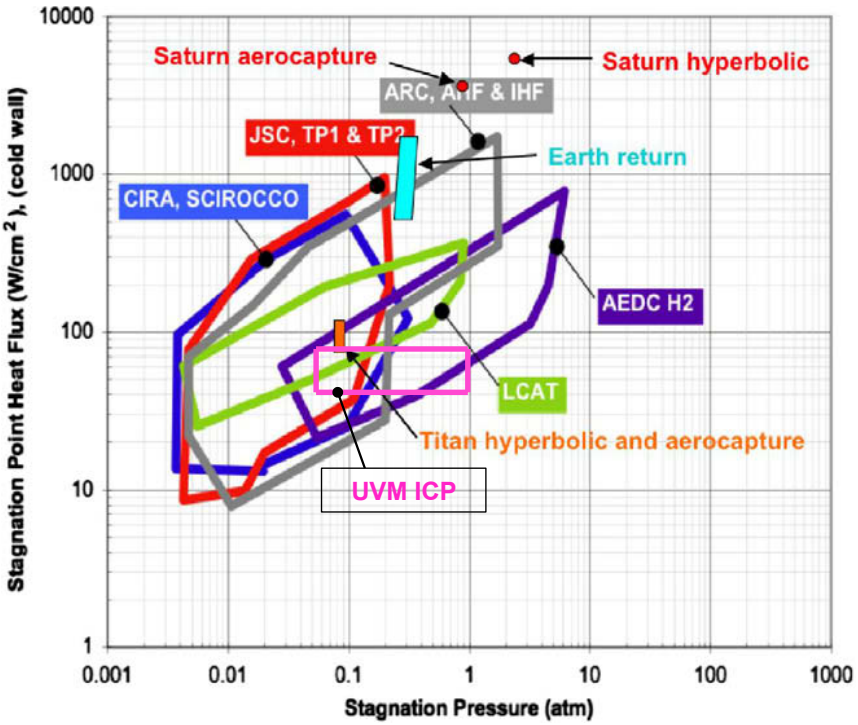

Figure 1.10: Capability of arc jets and ICP facility to stagnation point conditions for various missions [101].

hydrogen and helium that is required for Saturn missions. Lack of adequate ground test facilities for the development of new TPS materials is an issue. To accommodate for these limitations, a piecewise certification strategy is used. Each facility has certain capability of simulating the entry environment conditions. The respective capability of each facility along with computational modeling is used to combine all the pieces together to develop a TPS design process.

1.1.3 Computational Modeling

Computational Fluid Dynamics (CFD) is an important tool for TPS testing, design and development. Experimental testing is expensive and CFD simulations could be used in identifying test article failures and optimized testing conditions. Computational investigations are relatively less expensive in comparison to experimental tests [36]. The current CFD flow solvers can simulate the aerothermal environments

for Earth and planetary atmospheric entries. Examples [38] of such codes are Data Parallel Line Relaxation (DPLR) [109], Langley Aerothermal Upwind Relaxation Algorithm (LAURA) [22], and LeMANS [82, 83, 65]. When these codes are coupled with material response codes and relevant boundary conditions, CFD becomes an important tool in the vehicle TPS design and sizing assessment. Simulations are used to predict the total heat flux and heat load experienced by the TPS.

A full body three dimensional simulation of an entry flight condition is possible using CFD and the calculations from these simulations are used to ensure that the design of the TPS is verified for the desired range of entry conditions. The ground testing facilities that simulate the flight environment are used to validate the simulation codes. As mentioned earlier, no single high enthalpy ground test facility can recreate all flight conditions simultaneously. Each test facility can simulate some aspect of the flight environment. The computational models are validated using a partial simulation of the flight conditions approach. In this approach, a specific component of the flight environment or material response process is simulated and is validated with the data from the facility that generates the respective condition. The development and selection of a TPS material is performed by combining the advantages and capabilities of different test facilities and computational tools. CFD helps to understand the capabilities and short comings of the facility. To be able to use CFD simulations for accurate and confident predictions and analyses, the computational models are required to be verified and validated [42]. A model is verified to ascertain that the implementation of the numerics is correct. A model is validated to ensure that the physics of the process is modeled accurately. There are a lot of parameters that are required to be accounted for in a computational simulation. For example, environment inputs (atmospheric composition, temperature, etc.), surface boundary conditions (catalycity, surface reactions), material properties, thermochemical models, turbulence, etc. It is necessary to validate and verify the

accuracy of each parameter for reliable predictions. The uncertainty predicted in these parameters drives the choice of TPS sizing margins [107]. The physics for entry conditions is still not well understood both in real flight conditions and in ground test facilities [107, 19]. This poses deficiencies for computational models. Some of the key areas are nonequilibrium gas-kinetics, shock layer radiation, gas-surface interactions, transition and turbulent heating, and coupling between the material and the TPS environment. The uncertainties in the input parameters affect the CFD predictions. Input variables include the wall catalytic parameters, free stream conditions, transport property calculations, etc.

1.2 Scope of this dissertation

The surface recombination of gas-phase atoms due to the catalytic nature of the TPS material is a primary source of convective heating. Modeling of catalytic reactions and surface participating reactions in the hypersonic community has been primitive. The limited understanding of gas-surface interaction processes causes an uncertainty in the heating predictions. Improved understanding of these processes will have a significant effect on TPS selection and design. Thermal protection systems are designed with large safety factors. Therefore, minimization of mass is the primary objective. The peak heat flux with shear stress and surface pressure is used to select a thermal protection material whereas the total heat load decides the required thickness of the TPS material [34].

As described earlier, at hypersonic speeds the shock waves that form in front of the probe or vehicle cause high temperatures and enthalpy in the flow that leads to mostly dissociated molecular species in the boundary layer. The recombination of these atoms due to surface catalycity releases heat into the surface and increases the convective heating. The net heat flux encountered by a hypersonic vehicle or probe is the result of chemical and physical interactions between the gaseous flowfield and

the TPS surface [61]. The catalytic reactions mostly determine the amount of surface heating and the surface participating reactions affect material consumption. The catalytic activity of the surface, roughness, emissivity, etc. also change as a result of surface degradation from surface participating reactions. These processes if not included in the analysis could have a considerable effect on the TPS design.

During an Earth entry, molecular oxygen and nitrogen dissociate and diffuse to the TPS surface. The surface catalyzed recombination reactions, e.g. $O + O \rightarrow O_2$ and $N + N \rightarrow N_2$, release recombination energies of approximately 500 and 950 kJ/mole, respectively [61]. The effect of recombination reactions on the surface heating has been shown, for example, for Space Shuttle heating [76, 61, 93].

For Mars entries, the abundant atmospheric carbon dioxide dissociates into CO and O leading to surface recombination through the reactions: $O + O \rightarrow O_2$ and $O + CO \rightarrow CO_2$ releasing 500 and 530 kJ/mol of energy, respectively. The knowledge that the recombination reactions occur on the surface is insufficient to determine the heat transferred to the surface as a result of these reactions. The reaction pathway that these reactions take determines the net heat transferred. Generally, a conservative approach is taken and the reaction that produces the maximum energy is considered. This might result in a heavier heat shield than required. For example, full recombination of CO_2 is considered in computations as it releases the maximum energy but the recombination of atomic oxygen atoms is seen to be the dominant reaction in experiments [59, 61, 85]. Such uncertainties require a dedicated study of these processes.

Reactions between the gases and TPS material surface consume the solid material and in the process transform the surface as well. Most TPS to date are carbon and silicon carbide based. Molecular and atomic oxygen and atomic nitrogen cause oxidation and nitridation reactions that are exothermic. These reactions consume solid material, inject gas in the boundary layer thus changing its composition and

contribute to the aerothermal heating as well. Both the catalytic and surface participating reactions compete and the ratio of each reaction is uncertain. For example, atomic nitrogen can catalytically recombine on the surface or react with the carbon surface to form gaseous CN. Therefore, simultaneous occurrence of these processes needs to be accounted for in the computations.

The surface catalysis has been accounted for in hypersonics computations using conservative approaches that do not use any physics-based mechanisms of surface reactions. The boundary condition at the surface is defined by a catalytic efficiency γ. It is defined as the fraction of the flux of atomic gases that recombines to form molecules to the total flux of atomic gases. Its values are extracted from arc jet and ICP tests for stagnation point heating conditions [23, 89, 90, 91, 92, 61]. The non-catalytic wall assumes $\gamma = 0$ and provides the minimum heating to the vehicle or probe surface. Generally, a material specific constant value of γ or a function of wall temperature that is obtained from curve-fitting experimental data is used. For mission design, usually a fully catalytic wall boundary condition is assumed that is a conservative approach and provides maximum heating to the surface. In this case, all the chemical enthalpy in the dissociated flow is transferred to the wall without considering the actual chemical composition. Here, $\gamma = 1$ assuming that all the atomic species will recombine to form molecules. This approach was used in the design of the Mars Exploration Rover and Phoenix and baselined for MSL as well [108]. There have been some cases for the CO_2 environment where a surface reaction system (e.g. Mitcheltree model) and for air [31] have been incorporated but these cases have been hard coded for specific cases and are not generalized. In the Mitcheltree model [68, 108], the recombination $CO + O$ to CO_2 at the surface is modeled as a two-step reaction using an Eley-Rideal recombination reaction. This approach of hard wiring a model does not make it possible to study the impact of other reaction pathways and thus limits the design process.

1.2.1 Objective

The major objective of this dissertation is to investigate surface chemistry processes (e.g., catalysis, nitridation) using coupled CFD-surface chemistry models. Another objective is to assess the computations for surface chemistry models using experimental data.

The numerical simulations in this work are conducted using the Navier-Stokes computational fluid dynamics (CFD) code LeMANS developed at the University of Michigan. The investigation is performed using a finite rate surface chemistry model (FRSC) that incorporates the effects of surface catalysis as well as surface participating reactions. It can be applied to multiple gaseous species and can account for different surface reactions such as particle adsorption/desorption, the recombination of an atom of the gas with an atom adsorbed on the wall [Eley-Rideal (E-R) reaction], recombination of two adsorbed atoms at the wall [Langmuir-Hinshelwood (L-H) reaction] and reactions leading to surface recession (e.g. carbon nitridation, oxidation). The FRSC model is developed by Marschall and Maclean [61, 57] and is implemented in LeMANS by Alkandry *et.al* [8]. The effects of surface chemistry processes of a graphite sample exposed to a subsonic high-enthalpy nitrogen flow are investigated. In this work, simultaneous occurrence of nitrogen recombination due to surface catalysis and carbon nitridation (formation of CN) due to reaction between surface carbon and gaseous atomic nitrogen is simulated. The process of ablation is also analyzed by using a material response code MOPAR developed at the University of Michigan [62, 63, 7, 105]. MOPAR is coupled to LeMANS and can model heat conduction and pyrolysis process within the material.

A considerable amount of work has been performed to understand the flow physics and characteristics of arc jets through CFD modeling [36, 42]. Modeling of ICP facilities for entry flight conditions application has not been performed extensively [28, 97]. Some work has been performed for simulation of graphite ablation nitrogen

flow [97, 95, 96]. That work only considered the surface participating reaction of carbon nitridation where gaseous nitrogen reacts with surface carbon to form CN. It did not account for surface catalysis for nitrogen recombination which has been observed experimentally [40]. A numerical investigation is performed in the present work to characterize the nature of the gaseous flowfield in the test chamber of an ICP torch facility. The facility used for this investigation is the 30 kW Inductively Coupled Plasma (ICP) Torch Facility at the University of Vermont [53, 71]. Experimental tests conducted in the facility are used for assessment of the computations performed for different gas-surface interaction processes. The experiments are performed for graphite samples exposed to a high enthalpy nitrogen plasma stream. Most ablative heat shields are designed from carbon-based matrix materials impregnated with low temperature phase change polymer resins that pyrolyze leaving a carbon rich char layer. Since the carbon layer continues to interact with the boundary layer gases, reactions between this layer and the gas-phase particles are of immense interest and therefore graphite is used for this study. Graphite is non-charring and therefore pyrolysis gases are not produced. Also, since the goal of this study is to understand the fundamental nature and effects of gas-surface interactions, reaction between nitrogen gas and graphite is studied. If air is used with an ablating material that can pyrolyse, the thermo-chemistry becomes much more complex. It is then difficult to study the contribution and effect of each individual process.

1.3 Dissertation Overview

This section presents the layout of this dissertation. The dissertation is comprised of six chapters, with the introduction being Chapter I. The outline of the remaining chapters is presented as follows.

1.3.1 Outline

Chapter II outlines the technical approach used in this dissertation work. Both computational and experimental methods are used collectively to understand the physical and chemical processes that determine the aerodynamic heating of a probe or hypersonic vehicle during its entry into a planetary atmosphere. This chapter describes the experimental and computational techniques that are used to study the gas-surface interactions that occur on a vehicle surface during its entry into a planetary atmosphere. The chapter first provides a description of the experimental facility at the University of Vermont along with an overview of the experimental techniques employed to obtain flow and surface property measurements. It is followed by an overview of the CFD code used in this work along with the description of gas-surface interaction models implemented in the code.

Chapter III presents a description of the numerical setup used in this study. The conditions in the ICP torch test chamber simulated by LeMANS are based on the conditions used in the experiments at the University of Vermont. The geometry of the the test article used in the experiments is provided. A description of surface reactions investigated to study gas-surface interaction processes is presented along with details on the composition of the gas-mixture considered.

Chapter IV presents an analysis of the various factors that influence the numerical simulations ranging from the mesh of the flow field to the geometry of the experimental facility. The effect of these factors on the gas flow parameters and surface properties is also investigated. In the first section, a grid convergence study is performed to ensure the numerical solution is not affected by the mesh employed. It is followed by an assessment of the sensitivity of the flow around the graphite sample to the area of the test chamber included in the simulations. The second section of the chapter is focussed on a discussion on the effect of the physics of the gaseous flowfield in addition to the impact of a non-uniform inlet profile on the boundary layer parameters.

Chapter V presents the results obtained from the numerical simulations of the experimental configuration performed using the CFD code LeMANS. The main calculated parameters analyzed are translational temperature, normalized nitrogen atom density, surface heat flux, surface temperature and mass removal rate. The comparisons between the numerical results and experimental measurements are presented for translational temperature and normalized nitrogen atom number density in the test sample boundary layer. The numerical simulation results for each configuration (described in Chapter III) are compared with the respective experimentally measured data. The ICP torch exit conditions are not well defined. Therefore, an analysis is performed for sensitivity of boundary layer flow parameters and surface properties to different chemical compositions at the torch exit. First, comparison is performed between the sensitivity to chemical composition based on chemical equilibrium and that calculated from power in the flow. It is then followed by an evaluation of the effect on flowfield parameters and surface properties to varying inlet temperature for constant input power and varying input power for constant inlet temperature. All the calculations have been performed for radiative equilibrium boundary condition at the test article wall. This condition does not include the effects of conduction within the sample. Therefore, the effects of conduction within the sample wall are included in the calculations and compared with the results of radiative equilibrium condition. The results of the comparative analysis are presented in this chapter.

Finally, Chapter VI provides a summary of all the conclusions drawn from each chapter. It lists the major contributions of this dissertation to the investigation and comparison of different gas-surface interaction models for (non-charring) graphite exposed to high-enthalpy nitrogen plasma in an ICP facility.

The results from the study in this dissertation show that good agreement of computations with all experimental measurements is obtained if all the flow, surface and material physics are included in the simulations. It is identified that true validation

of surface chemistry models requires absolute number density measurements. It is also determined that validation of such simulations requires better characterization of the power absorbed by the plasma in the ICP torch. The chapter concludes with a recommendation of possible future directions for this research topic.

CHAPTER II

Technical Approach

2.1 Introduction

Computational Fluid Dynamic (CFD) models can be used for simulating environments that cannot be studied in an experimental test facility. These models can be used for accurately predicting the aerothermal environment of the vehicle TPS during entry, but these models can be used to perform such analysis only after they have been validated for physical accuracy by comparison with experimental measurements. Both computational and experimental methods can be used collectively to understand the physical and chemical processes that determine the aerodynamic heating of a probe or hypersonic vehicle during its entry into a planetary atmosphere.

This chapter describes the experimental and computational techniques that are used to study the gas-surface interactions that occur on a vehicle surface during its entry into a planetary atmosphere. The chapter first provides a description of the experimental facility at the University of Vermont along with an overview of the experimental techniques employed to obtain flow and surface property measurements. It is followed by an overview of the CFD code used in this work along with the description of gas-surface interaction models implemented in the code. The chapter concludes with a summary of the important points.

2.2 Experimental Facility

Experimental tests were conducted by Professor Doug Fletcher and his graduate students in a 30 kW Inductively Coupled Plasma (ICP) Torch Facility at the University of Vermont [53, 71]. Laser diagnostic instrumentation that employs a Laser Induced Fluorescence (LIF) technique is installed at the facility. LIF is capable of measuring various flow parameters such as translational temperature and species number densities at different locations in the flowfield. The facility is equipped with a two-color infrared pyrometer that is used to measure test sample surface temperature. This section describes the facility and techniques that are used to obtain experimental data that will be compared to the numerical results.

2.2.1 Inductively Coupled Plasma Torch Facility

The ICP torch facility is designed to test scaled material samples in high enthalpy gas flows for simulation of planetary entry and Earth atmosphere re-entry trajectory heating conditions. It is configured for operation with subsonic flow to simulate post shock conditions of high enthalpy flight for a stagnation point geometry. The facility test conditions can be extrapolated to flight conditions by matching three parameters at the edge of the boundary layer, i.e., the enthalpy, the stagnation pressure and the velocity gradient. The stagnation point heat flux in the flight is equal to that in ground tests if these parameters are matched [49].

The facility is primarily comprised of the power supply unit, gas injection system and plasma test chamber. The gas injection system provides the nitrogen gas at room temperature that enters into the quartz confinement tube where hot nitrogen plasma is generated through an induced RF magnetic field created by a helical load coil. An illustration of the plasma generating components of the facility is shown in Fig. 2.1.

The hot nitrogen plasma then flows out of the quartz tube from the top into the test chamber of the ICP facility where the sample is tested. The test chamber is

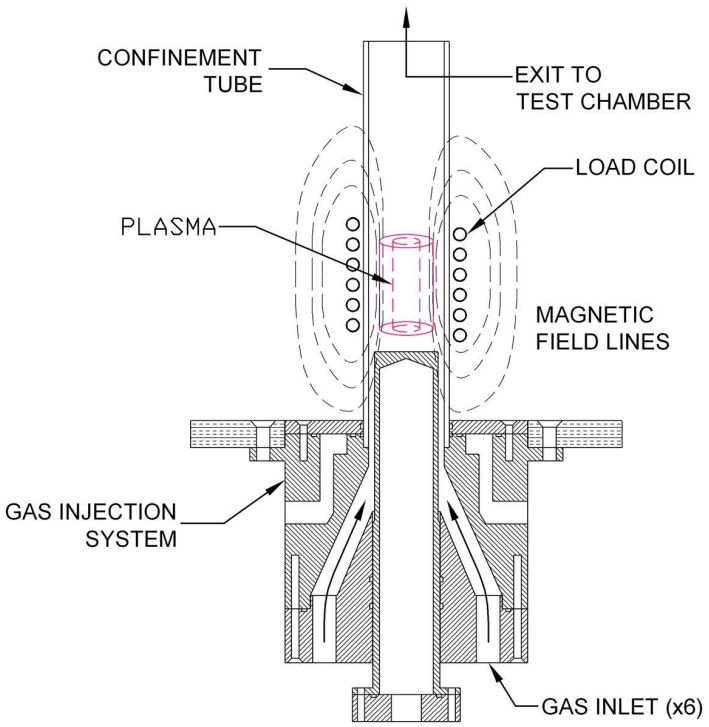

Figure 2.1: Illustration of the plasma generating components of the ICP torch facility

constructed from stainless steel and the torch locations with the highest heat loads are actively cooled with a closed loop water system. The test article is installed in a brass sample holder and the back space side of the sample is water cooled. For this investigation, experimental results from graphite samples tested in the nitrogen plasma stream are used. The test articles are constructed from DFP2 grade graphite, fabricated by POCO Graphite [86]. Most ablative TPS materials are organic composites that make it necessary to study interaction with carbon based materials. Figure 2.2 shows a photograph of the graphite article during exposure to the nitrogen plasma in the test chamber of the ICP Torch Facility.

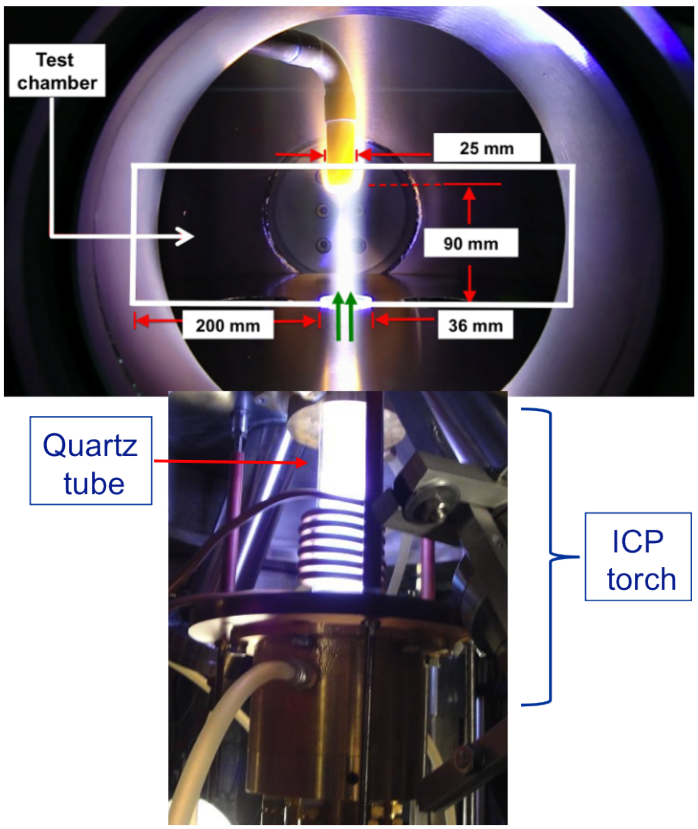

Figure 2.2: Experimental set up with graphite test article in nitrogen plasma in the test chamber of the ICP torch facility (section in box is the portion simulated using the CFD code LeMANS) (Source: Prof. D.G. Fletcher [52]).

2.2.2 ICP Torch Measurements

The quantities measured are the surface heat flux, surface temperature, relative nitrogen atom number density and translational temperature in the reacting boundary layer above the graphite surface [73]. The graphite sample mass loss (ablation) rate is also quantified. The techniques used for measuring these quantities are described next.

2.2.2.1 Heat Flux Measurements

The stagnation region heat transfer is measured with a copper slug calorimeter. A schematic of the slug calorimeter is shown in Fig. 2.3. The copper slug is housed

within a brass holder that is identical in size and shape to the graphite test sample. Pure copper has a high rate of surface catalyzed recombination and therefore the measured heat flux is assumed to be that for a fully catalytic condition, although oxidization of the copper surface is seen in experiments that lowers its catalytic efficiency [70]. Therefore, the heat flux measured should be lower for copper oxide than for pure copper when both are exposed to the same condition. The back space side temperature is measured with a thermocouple. The calculation of the heat flux assumes one-dimensional heat transfer and that the incident heat flux is absorbed at the slug surface [70, 43]. The teflon insulator and an air gap between the slug and the brass holder help to maintain one-dimensional heat transfer through the slug. The steady state heat flux is calculated using Eq. 2.1.

$$q = l\rho C_p \frac{\delta\tau}{\delta t} \tag{2.1}$$

where l is the axial length, ρ is the density of copper, C_p is the specific heat of copper and $\delta\tau/\delta t$ is the temperature gradient on the back surface of the copper slug. The physical properties of the copper slug are known and the time dependent temperature term is determined experimentally.

2.2.2.2 Surface Temperature Measurements

The surface temperature is measured using a two-color infrared optical pyrometer with a temperature range from 1273 to 3273 degrees K.

2.2.2.3 Ablation Rate Measurement

The sample mass loss is quantified from pre- and post-test mass measurements.

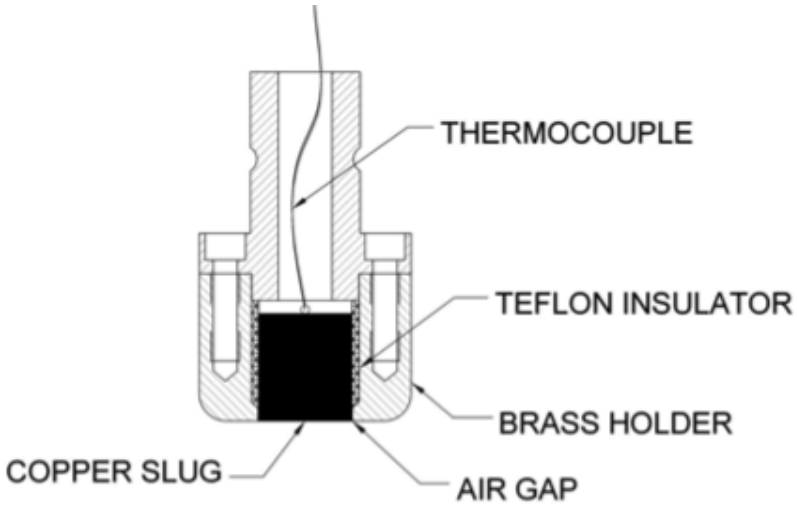

Figure 2.3: Schematic of the copper slug

2.2.2.4 Flow Properties Measurements

The experimental tests measure the gas-phase flow properties, i.e., nitrogen atom number density and translational temperature, in the reacting boundary layer above the graphite surface using a two-photon laser induced fluorescence (LIF) technique.

A microwave discharge flow reactor (MDFR) is used to establish absolute species concentration and translational temperature in the flow in the ICP test chamber. The MDFR is a laser measurement calibration facility that is operated at known conditions, i.e., 0.5 torr pressure and room temperature. A chemical titration process is used to determine the species atom concentration in the flow reactor. It is based on the principle that the absolute flow properties within the ICP test chamber can be calibrated from comparing measurements obtained both from the ICP test chamber and the MDFR. Atomic nitrogen is produced in MDFR as the molecular nitrogen flows through a microwave discharge that creates partially dissociated nitrogen gas.

Experimental data is obtained by measuring the LIF signal within the ICP torch and MDFR simultaneously. For each LIF measurement in the ICP flow, a simultaneous measurement is recorded in the flow reactor. In a LIF measurement, the species

to be examined is excited with a laser at a specific excitation wavelength. The excited species transitions to a lower energy state after some time emitting fluorescent light that is recorded with a photomultiplier tube (PMT). The PMT is the detection optics used to detect the LIF from the ICP and MDFR. A spectral model fit of the two-photon LIF signal for atomic nitrogen both in the ICP torch and MDFR is used to extract species concentrations and temperature. An example [55] of two-photon LIF signals from atomic nitrogen obtained from the subsonic free stream of an ICP flow and from the MDFR are shown in Figure 2.4. The spectral model fit to the data is also shown for both the flow and reactor signals.

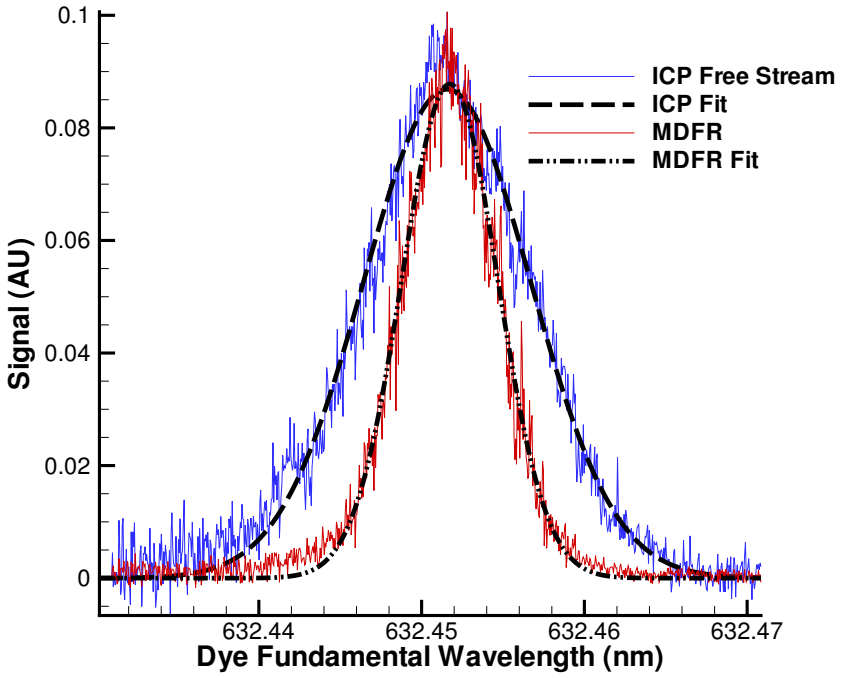

Figure 2.4: Two-photon LIF signals within the ICP test chamber and the microwave discharge flow reactor

The absolute nitrogen atom number density is calculated from Eq. 2.2. Unfortunately, the calibrated absolute atom number density values are not yet available. Therefore, the relative nitrogen atom number density $n_{N_{relative}}$ is used for assessing the computational simulations. The spectrally integrated LIF signal is proportional

to the concentration of the absorbing species.

$$(n_N)_{icp} = (n_N)_{relative}\,(n_N)_{mdfr} \tag{2.2}$$

where

$$\begin{aligned}
(n_N)_{relative} &= \frac{(n_N)_{icp,relative}}{(n_N)_{mdfr,relative}} \\
(n_N)_{icp,relative} &= \int (S/E^2)_{icp} d\omega \; {w^2}_{icp}/(D_{icp}\tau_{icp}) \\
(n_N)_{mdfr,relative} &= \int (S/E^2)_{mdfr} d\omega \; {w^2}_{mdfr}/(D_{mdfr}\tau_{mdfr})
\end{aligned}$$

where, S is the LIF signal, E is the laser pulse energy, τ is the fluorescence lifetime of transition, w is the effective diameter of the beam at the measurement location, and ω is the photon energy $h\nu$.

The translational temperature is determined from the spectral line width of the LIF signals within the ICP and MDFR. The total line width from the LIF signal from each facility ($\Delta\hat{\nu}^2_{T,icp}, \Delta\hat{\nu}^2_{T,mdfr}$) is the sum of the laser line width ($\Delta\hat{\nu}^2_L$) and the Doppler width ($\Delta\hat{\nu}^2_{D,icp}, \Delta\hat{\nu}^2_{D,mdfr}s$) as shown in Eq. 2.3.

$$\begin{aligned}
\Delta\hat{\nu}^2_{T,icp} &= \Delta\hat{\nu}^2_L + \Delta\hat{\nu}^2_{D,icp} \\
\Delta\hat{\nu}^2_{T,mdfr} &= \Delta\hat{\nu}^2_L + \Delta\hat{\nu}^2_{D,mdfr}
\end{aligned} \tag{2.3}$$

As seen in Figure 2.4, the spectral width of the transition measured in the ICP flow is broader than that measured in the MDFR, indicating a higher temperature relative to that in the flow reactor. The laser line width is determined from the flow reactor where the temperature and the Doppler width are maintained at known ambient conditions. The total line widths of the ICP and MDFR flows are obtained

from the respective ICP and MDFR LIF signals. Once the laser line width is obtained, the translational temperature is determined from Eq. 2.4.

$$T_{trans,icp} = \frac{M_N c^2}{8ln(2)k_B n_A \hat{\nu}^2} \left[\Delta\hat{\nu}^2_{T,icp} - (\Delta\hat{\nu}^2_{T,mdfr} - \Delta\hat{\nu}^2_{D,mdfr})\right] \tag{2.4}$$

where M_N is the molecular weight, k is Boltzmann's constant, n_A is Avogadro's number, $\hat{\nu}$ is the transition central wavenumber in cm^{-1}, the $\Delta\hat{\nu}_{I,J}$ are the line width values where the subscripts denote the width for ICP or MDFR and Total or Doppler.

2.3 CFD Modeling

The purpose of this dissertation is to use CFD for the investigation of gas-surface interactions that determine the aerothermal heating of a probe or hypersonic vehicle during its entry into a planetary atmosphere. This section provides a brief overview of the CFD code and a description of the gas-surface interaction models implemented in this code.

2.3.1 LeMANS Overview

The numerical simulations in this work are conducted using the Navier-Stokes computational fluid dynamics (CFD) code LeMANS [82, 83, 65], developed at the University of Michigan. It is a general purpose, parallel, three-dimensional code that solves the laminar Navier Stokes equations including chemical and thermal nonequilibrium effects on unstructured computational grids. The flow is modeled assuming the continuum approximation is valid.

The translational and rotational energy modes of all species can be described by their respective temperatures T and T_r in the code. However, in this work, the translational and rotational modes are assumed to be equilibrated. The translational and rotational energy modes are assumed to be equilibrated as these modes usually

require relatively few collisions to reach equilibrium. Therefore, the translational and rotational energy modes of all species are described by a single temperature T_{tr}. The vibrational and electronic energy modes of all species are described by a single temperature T_{ve}. The governing equations solved by LeMANS are as follows,

mass:

$$\frac{\partial \rho_s}{\partial t} + \nabla \cdot (\rho_s \mathbf{V} + \mathbf{J}_s) = \dot{w}_s \tag{2.5a}$$

momentum:

$$\frac{\partial \rho \mathbf{V}}{\partial t} + \nabla \cdot (\rho \mathbf{V}\mathbf{V} + p - \tau_{i,j}) = 0 \tag{2.5b}$$

total energy:

$$\frac{\partial E}{\partial t} + \nabla \cdot \left((E + p)\, \mathbf{V} - \tau_{i,j} \cdot \mathbf{V} + \mathbf{q} + \sum_s (\mathbf{J}_s h_s) \right) = 0 \tag{2.5c}$$

vibrational-electronic energy:

$$\frac{\partial E_{ve}}{\partial t} + \nabla \cdot \left(E_{ve} \mathbf{V} + \mathbf{q}_{ve} + \sum_s (\mathbf{J}_s e_{ve,s}) \right) = \dot{w}_{ve} \tag{2.5d}$$

where ρ_s is the density of species s, $\mathbf{V}$ is the velocity vector, $\mathbf{J_s}$ is the diffusion flux for species s, the source term $\dot{w}_s$ includes the production and consumption rate of species s as a result of chemical reactions. p is the pressure, $\tau_{i,j}$ is the viscous stress tensor, h_s is the species enthalpy, $e_{ve,s}$ is the vibrational-electron-electronic energy per unit mass and $\dot{w}_{v,e}$ is the vibrational energy source term. E and E_{ve} are the total and vibrational-electron-electronic energies per unit volume of mixture, respectively. The source terms $\dot{w}_s$ are modeled using a finite rate chemistry model developed by Martin and Boyd [64] along with Park's two-temperature model to account for thermal nonequilibrium effects on the reaction rates. The heat flux vector $\mathbf{q}$ is given by,

$$\mathbf{q} = \mathbf{q}_{conv} + \mathbf{q}_{diff} \tag{2.6}$$
$$\mathbf{q}_{conv} = \mathbf{q}_{tr} + \mathbf{q}_{ve}$$

where $\mathbf{q}_{tr}$ is the translational-rotational convective heat flux, $\mathbf{q}_{ve}$ is the vibrational–electron-electronic energy convective heat flux and $\mathbf{q}_{diff}$ is the diffusive heat flux. In this system, the viscous stress tensor components τ_{ij} are modeled assuming a Newtonion fluid and are determined using Stokes' hypothesis [104],

$$\tau_{ij} = \mu \left(\frac{\partial u_i}{\partial x_i} + \frac{\partial u_i}{\partial x_j} \right) + \delta_{ij} \lambda \bigtriangledown \vec{u} \tag{2.7}$$
$$\lambda = -\frac{2}{3}\mu$$

The convective heat fluxes $\mathbf{q}_{tr}$ and $\mathbf{q}_{ve}$ for each energy mode are modeled according to Fourier's law as,

$$\mathbf{q}_{tr,ve} = -\kappa_{tr,ve} \bigtriangledown T_{tr,ve} \tag{2.8}$$

where $\kappa_{tr,ve}$ is the mixture thermal conductivity for each energy mode. The diffusive heat flux $\mathbf{q}_{diff}$ is calculated as,

$$\mathbf{q}_{diff} = \sum_{s=1}^{ns} h_i \mathbf{J}_s \tag{2.9}$$

where $\mathbf{J}_s$ is the species mass diffusion flux modeled using modified Fick's law for multi-component diffusion. The modified equations ensure that the diffusion mass fluxes sum to zero by distributing the residual according to the species mass fraction [94]. $\mathbf{J}_{s,corrected}$ is the species mass diffusion flux used in the calculations and is given

by,

$$\mathbf{J}_{s\neq e,corrected} = \mathbf{J}_s - Y_s \sum_{r\neq e} \mathbf{J}_r \tag{2.10}$$

and,

$$\mathbf{J}_s = -\rho D_s \bigtriangledown Y_s$$

where D_s is the species diffusion coefficient and Y_s is the species mass fraction. The electron diffusion flux $\mathbf{J}_e$ is not included in Eq. 2.10 because its value is small due to the relatively small molecular weight of electrons as compared to atoms and molecules. It is calculated as,

$$\mathbf{J}_e = M_e \sum_{s\neq e} \frac{\mathbf{J}_s C_s}{M_s} \tag{2.11}$$

where M_e is the electron molecular weight and C_s is the species charge. The set of partial differential equations are solved using a finite-volume method on unstructured grids. The inviscid fluxes across cell faces are discretized using a modified form of the Steger-Warming Flux Vector Splitting (FVS) scheme [56] which is less dissipative and produces better results in boundary layers than their original scheme. The viscous terms are calculated using a centered scheme. Time integration is performed using a point implicit or a line implicit method. LeMANS is parallelized using METIS [48] that partitions the computational grid between the processors and the Message Passage Interface (MPI) protocol to communicate information between processors. Turbulent flows could be simulated for simple geometries using a zero equation algebraic Baldwin-Lomax turbulence model [11] implemented in LeMANS. The model is not used for numerical simulation in this dissertation work as the flowfield studied has laminar behavior. The free stream Reynolds number for the two flowfields an-

alyzed in this dissertation are 285 and 295, respectively, indicating that the flow is laminar. The mixture transport properties, i.e., the coefficients of viscosity, thermal conductivity and mass diffusion can be computed using two models. The first model uses Wilke's semi-empirical mixing rule [106] with species viscosities calculated using Blottner's model [18] and the species thermal conductivities are determined using Eucken's relation [103]. The other model uses Gupta's mixing rule [44] with species viscosities and thermal conductivities calculated using collision cross section data. Details on the modeling of these equations can be found in Ref. [81].

LeMANS can simulate two-dimensional/axisymmetric flows using any mixture of quadrilaterals and triangles, and three-dimensional flows using any mixture of hexahedra, tetrahedral, prisms and pyramids. The code has been extensively validated for hypersonic flows [81, 16, 98, 30, 6].

2.4 Numerical Boundary Conditions

2.4.1 Inlet and Outlet Boundary Conditions

In LeMANS, the inflow and outflow boundary conditions are specified for hypersonic flows. For hypersonic flows, all the variables should be specified at the inflow and none should be specified at the outflow when the exit is also at supersonic speeds. The flow in the case of an ICP torch test facility is subsonic in nature. For a subsonic flow, the disturbances propagate upstream against the flow direction and this needs to be accounted for. Therefore, new inflow and outflow boundary conditions are implemented for subsonic flow conditions [78]. For the subsonic inlet boundary, a full state boundary condition calculated using a Riemann solver is implemented. In this condition, all the variables, i.e., velocity, density and temperature, are directly specified.

For the subsonic outlet boundary condition, a constant pressure boundary condi-

tion is implemented in which static pressure is specified at the outlet. The velocity and density variables are solved using zeroth order extrapolation. The specified outlet pressure is used to compute the temperature variable using the equation of state.

2.4.2 Wall Boundary Conditions

In the simplest approach, wall catalycity effects are accounted for in LeMANS by choosing a non-catalytic or a super-catalytic surface as the species boundary condition. The catalycity of a surface in general can be accounted for by four types of conditions at the wall boundary as described in Table 2.1. A super-catalytic boundary condition is inappropriate for the flows that are comprised of dissociated species at the free stream as this condition will lead to the same composition through dissociation/recombination at the wall as in the free stream which is undesirable for conditions where the effect of recombination on the heat transfer is to be studied. In addition to surface catalysis, surface participating reactions are required to be included in the analysis for a thorough understanding of gas-surface interactions. Therefore, a simple binary catalytic recombination model and a complex finite rate surface chemistry model are implemented in LeMANS. A description of the models is presented in this section.

Table 2.1: Species boundary conditions.

Boundary Condition	Description
Non-catalytic	No recombination of atoms on the surface
Super-catalytic	Atoms that strike the surface recombine to the free stream gas composition
Fully-catalytic	All atoms that strike the surface recombine to form molecules
Partially-catalytic	Some atoms reflect and some recombine

2.4.3 Binary catalytic recombination model

For the simulation of the full range of catalycity regimes, from a non-catalytic wall to a fully-catalytic wall, a simplified catalytic atom recombination model, i.e. a binary interaction model with full energy accommodation, [84, 80] is implemented in LeMANS. It is a simple model applied to a binary gaseous mixture of atoms and molecules. It is implemented by balancing the mass flux of the relevant species at the wall. It is applied as a species boundary condition by considering a first order recombination reaction for a binary gas at the wall. The model is presented for the N_2-N binary mixture since the gas used in this investigation is nitrogen.

The boundary condition for the mass fraction Y_N of atomic nitrogen and Y_{N_2} of molecular nitrogen in a binary mixture (N_2-N) is given by the expression shown in Eq. 2.12.

$$\begin{aligned} D_{12}\frac{\partial Y_N}{\partial n} &= k_{wN}Y_N \\ Y_{N_2} &= 1 - Y_N \end{aligned} \tag{2.12}$$

where D_{12} is the binary diffusion coefficient between atomic and molecular species, n is the wall normal direction and k_{w_N} is the catalytic recombination speed given by the Hertz-Knudsen relation shown in Eq. 2.13.

$$k_{wN} = \gamma_N \sqrt{\frac{k_B T_w}{2\pi m_N}} \tag{2.13}$$

where T_w is the wall temperature and m_N is the nitrogen atom mass. In this model, the atoms that impinge on a surface either reflect from the surface and neither gain nor lose energy at the surface, or become adsorbed where an atom reacts with another atom to produce a molecule. In the latter case, the energy released by the reaction, which is highly exothermic, is assumed to be entirely transferred to the wall and this

phenomenon is called full energy accommodation. In this model, a dimensionless surface recombination coefficient γ (also referred to as the catalytic efficiency) is introduced [39, 20, 84]. It is defined as the ratio of the flux of atoms that recombine on the surface $\dot{M}_{rec}$ to the total flux of atoms that impinge on the surface $\dot{M}_{imp}$ and the expression is shown in Eq. 2.14.

$$\gamma = \frac{\dot{M}_{rec}}{\dot{M}_{imp}} \tag{2.14}$$

This coefficient depends on the particular atom and surface involved. If the wall is fully-catalytic, then γ_N and the corresponding boundary condition for the atom becomes,

$$\begin{aligned} &\gamma_N = 1 \\ &Y_N = 0;\ Y_{N2} = 1 \end{aligned} \tag{2.15}$$

This condition provides the maximum heat transferred to the surface as all the atoms that impinge on the surface form molecules. If the wall is non-catalytic, then γ_N is set to zero that implies the species concentration gradient is zero at the wall (Eqn. 2.16). The mass fractions Y_N, Y_{N2} at the wall do not change. The heat transferred to the surface is minimum for this boundary condition. If the wall is partially catalytic, γ_N is set to a value between 0 and 1 based on the catalycity of the surface. The mass fractions at the wall are calculated using Eq. 2.12.

$$\frac{\partial Y_N}{\partial n} = -\frac{\partial Y_{N_2}}{\partial n} = 0 \tag{2.16}$$

2.4.4 Finite rate surface chemistry model

The finite rate surface chemistry (FRSC) model is a general gas-surface interaction model [61, 57, 8]. It can be used to investigate the effects of surface catalysis as well

as surface participating reactions. The FRSC model developed by Marschall and Maclean [61, 57] was implemented in LeMANS by Alkandry *et.al* [8]. The model can simulate the chemical reactions between the hypersonic gas and surface of the vehicle during planetary entry. A simplified binary catalytic atom recombination model can only be used to study the effects of surface catalysis for a constant catalytic efficiency applied to a binary gaseous mixture of atoms and molecules. The FRSC model can be applied to multiple gaseous species and can account for different surface reactions such as particle adsorption/desorption, the recombination of an atom of the gas with an atom adsorbed on the wall [Eley-Rideal (E-R) reaction], recombination of two adsorbed atoms at the wall [Langmuir-Hinshelwood (L-H) reaction] and reactions leading to surface recession (e.g. carbon nitridation, oxidation). The description of these surface reactions is given as:

Adsorption/Desorption:	$A + (s) \rightleftharpoons A(s)$
Eley-Rideal:	$A + B(s) \rightleftharpoons AB + (s)$
Langmuir-Hinshelwood:	$A(s) + B(s) \rightleftharpoons AB + (s)$
Sublimation/Condensation:	$(s) + A(b) \rightleftharpoons A + (s)$
Nitridation/Reduction:	$A + (s) + B(b) \rightleftharpoons AB + (s)$

where (s) is an empty active surface site, A(s) and B(s) are adsorbed particles, and A(b) and B(b) are bulk material species. The FRSC model is based on the concept of simulating surface chemical reactions by competing finite rate processes. It is comprised of three environments viz. gas, surface, and the bulk environment. Each environment can consist of one or more "phases" that correspond to a distinct physical region of the respective environment. The gas environment is a single phase ($N_g = 1$) that contains gas-phase species. All the gas-phase species in this environment must

either be involved in the surface reactions or as a species blown into the gas phase by gas-injection or in-depth pyrolysis.

The surface environment can consist of multiple phases represented by ns ranging from 1 to the total number of surface phases N_s. Each surface phase occupies a fraction Ω_{ns} of the total surface. Each surface phase can be comprised of multiple sets of active sites represented by na ranging from 1 to the total number of active sites for each phase $N_{ns,a}$. Each active site set has a site density $\Phi_{ns,na}$. All the surface reactions take place at active sites. Similarly, the bulk environment can consist of multiple phases (nb = 1,...,N_b). Each phase occupies a volume fraction v_{nb} of the bulk and contains a unique set of species K_{nb}. The total number of phases is:

$$N = 1 + N_s + N_b \tag{2.17}$$

The total number of species is the summation of gas, surface and bulk phase species given by Eq. 2.18. In this formulation, a particular species (for example: atomic nitrogen) is considered a different species if it is in gas phase or in a particular active site in a surface phase or in a bulk phase. The description of all the variables is provided in the nomenclature.

$$K = K_g + \sum_{ns=1}^{N_s} \sum_{na=1}^{N_{ns,a}} K_{ns,na} + \sum_{nb=1}^{N_b} K_{nb} \tag{2.18}$$

For a system with K species and N_R surface reactions, the general form of the surface reaction i can be expressed as,

$$\sum_{k=1}^{K} \nu_{ki}^{'} A_k \rightleftharpoons \sum_{k=1}^{K} \nu_{ki}^{''} A_k \tag{2.19}$$

where $\nu_{ki}^{'}$ and $\nu_{ki}^{''}$ are the respective reactant and product stoichiometric coefficients for species A_k. The net production rate $\dot{w}_k$ of species A_k is the sum of the production

rates from all surface reactions given by Eq. 2.20. It applies to species in any phase at the gas/surface interface.

$$\dot{w}_k = \sum_{i=1}^{N_R} \dot{w}_{ki} \tag{2.20}$$

where the reaction-specific production rate $\dot{w}_{ki}$ is the product of net stoichiometric coefficient ν_{ki} and reaction flux $r_{i,ns}$ for reaction i on phase ns given by the expression in Eq. 2.21.

$$\begin{aligned} \dot{w}_{ki} &= \nu_{ki} r_{i,ns} \\ \nu_{ki} &= (\nu_{ki}^{''} - \nu_{ki}^{'}) \\ r_{i,ns} &= k_{fi} \prod_{k=1}^{K} X_k^{\nu_{ki}^{'}} - k_{bi} \prod_{k=1}^{K} X_k^{\nu_{ki}^{''}} \end{aligned} \tag{2.21}$$

where k_{fi} and k_{bi} are the forward and backward reaction rates for reaction i, respectively. X_k is the concentration of species A_k at the surface and for each phase it can be described as,

$$\begin{aligned} &\text{Gas phase:} && X_k = C_k = \chi_k \frac{P}{RT} \\ &\text{Surface phase:} && X_k = \Phi_{ns,k} = \theta_{ns,k} \Phi_{ns} \\ &\text{Bulk phase:} && X_k = \chi_{nb,k} \end{aligned} \tag{2.22}$$

The forward reaction rate for each surface reaction type can be specified by an Arrhenius function or using a kinetic-based formulation for specific processes like adsorption, Eley-Rideal recombination and Langmuir-Hinshelwood recombination. The FRSC model can account for competing finite-rate processes under a given set of experimental conditions and provides an effective reaction efficiency for a gas-phase reactant consumed in a surface reaction process. For this study, the FRSC model

is used to simulate a constant reaction efficiency by using the appropriate choice of reaction types and parameters. The gas-surface interaction processes studied are the recombination of nitrogen atoms to molecules at the surface due to catalysis, and the carbon nitridation reaction where nitrogen atoms react with the surface carbon to form gaseous CN. The surface reaction types considered are adsorption and Eley-Rideal (E-R) recombination to emulate a constant reaction efficiency for these processes. The E-R mechanism involves the reaction of a gas-phase species with an adsorbed species to form a gas-phase product. The surface reaction for an adsorption process for a particle A can be represented by,

$$A + (s) \rightarrow A(s)$$

where (s) is an empty active site and A(s) is an adsorbed particle. The forward reaction flux for an adsorption process is the product of the sticking coefficient S_0, the impingement flux Γ_A of species A on the surface, and the fraction $\theta_{s,e}$ of available active sites that are empty:

$$r_f = S\ \Gamma_A\ \theta_{s,e} \tag{2.23}$$

where the sticking coefficient is :

$$S = S_0\ exp\left(\frac{-E_{ad}}{RT}\right)$$

The sticking or adsorption coefficient S_0 is the fraction of the gas phase species that hit the surface and become adsorbed.

The impingement flux is given by:

$$\Gamma_A = \frac{\bar{\nu}_A}{4} C_A$$

where the thermal velocity of species A is :

$$\bar{\nu}_A = \sqrt{\frac{8RuT}{\pi M_A}}$$

and the fraction of available empty active sites is :

$$\theta_{s,e} = \frac{\Phi_{s,e}}{\Phi_s}$$

The forward reaction rate for an adsorption process is expressed by the following:

$$k_f = \left[\frac{\bar{\nu}_A}{4\phi_s^{\nu_s}}\right] S_0 exp\left(-\frac{E_{ad}}{R_u T}\right) \tag{2.24}$$

The surface reaction for an Eley-Rideal (E-R) recombination of a particle A with an adsorbed particle B(s) can be represented by,

$$A + B(s) \rightarrow AB + (s)$$

The forward reaction flux for an Eley-Rideal (E-R) recombination process is the product of the Eley-Rideal reaction efficiency γ_{er}, the impingement flux Γ_A of species A on the surface, and the fraction $\theta_{s,B}$ of available active sites that are occupied by adsorbed species B:

$$r_f = \gamma_{er}\ \Gamma_A\ \theta_{s,B}$$

where the Eley-Rideal reaction efficiency is:

$$\gamma_{er} = \gamma_0\ exp\left(\frac{-E_{er}}{RT}\right)$$

and the fraction of available empty active sites is:

$$\theta_{s,B} = \frac{\Phi_{s,B}}{\Phi_s} \tag{2.25}$$

The forward reaction rate for an Eley-Rideal (E-R) recombination process is expressed by the following :

$$k_f = \left[\frac{\bar{\nu}_A}{4\phi_s^{\nu_s}}\right] \gamma_0 exp\left(-\frac{E_{ER}}{R_u T}\right) \tag{2.26}$$

The backward reaction rate for both processes is zero as both the thermal desorption and dissociation with a partial adsorption process (shown by Eq. 2.27) are not considered in this work.

$$\begin{aligned} &A(s) \rightarrow A + (s) : \text{Thermal desorption} \\ &AB + (s) \rightarrow A + B(s) : \text{ Dissociation with partial adsorption} \end{aligned} \tag{2.27}$$

The E-R reaction can also be used to represent a process where a gas phase species impinges on the surface and reacts with the surface. An example is shown in Eq. 2.28, where the gas phase species A impinges on the surface and reacts with the bulk phase species B_b on the surface.

$$A + (s) + B_b \rightarrow AB + (s) \tag{2.28}$$

This equation is used to emulate the carbon nitridation reaction. The species mass fraction at the wall is calculated by balancing the mass flux of the relevant species taking the consumption and production at the wall into account as shown in Eq. 2.29,

$$-\rho_w D_k \frac{\partial Y_k}{\partial n}|_w + \rho_w v_w Y_{k,w} = M_k \dot{w}_k \tag{2.29}$$

Here, the first term "$-\rho_w D_k \frac{\partial Y_k}{\partial n}|_w$" represents diffusion of gas-phase species, the second term "$\rho_w v_w Y_{k,w}$" represents mass flux of species blown from the surface into gas-phase and the term on the right "$M_k \dot{w}_k$" represents production or consumption of species from surface reactions. In the second term, $\rho_w v_w$ is the mass blowing rate $\dot{m}_b$ at the surface due to surface reactions (e.g. oxidation, nitridation and sublimation). It is given by the following expression:

$$\dot{m}_b = \rho_w v_w = -\sum_{nb=1}^{N_{nb}} \sum_{k=1}^{K_{nb}} M_k \dot{w}_k \tag{2.30}$$

2.4.5 Heat flux at the wall

Heat transfer to the surface $\mathbf{q}$ given by Equation 2.6 is composed of convective heat flux $\mathbf{q}_{conv}$ and heat flux $\mathbf{q}_{diff}$ due to diffusion of species to the surface. The convective heat flux is composed of convection due to each energy mode. Eq. 2.6 is used to set the isothermal wall boundary condition where the heat transfer to the wall balances to maintain the assigned wall temperature T_w.

The energy balance on an ablative surface is shown in Fig. 2.5 and the relation is given in Eq. 2.31. The subscript g indicates the terms representing the contribution from pyrolysis gas. These terms are zero as graphite is non-charring, and pyrolysis is not accounted for. The enthalpy of the gas at the wall h_w is assumed to be equal to the enthalpy of the material gained from the bulk (solid) phase $h_{b,w}$. Therefore, the terms involving the enthalpy of ablated material cancel out.

$$\mathbf{q}_{conv} + \mathbf{q}_{diff} + \dot{m}_b h_{b,w} + \dot{m}_g h_{g,w} + \mathbf{q}_{rad-in} = (\dot{m}_b + \dot{m}_g) h_w + \mathbf{q}_{rad-out} + \mathbf{q}_{cond} \tag{2.31}$$

$$\mathbf{q}_{rad-out} = \sigma \epsilon {T_w}^4$$

If the radiative $\mathbf{q}_{rad-in}$ and conductive heat flux $\mathbf{q}_{cond}$ into the material are ne-

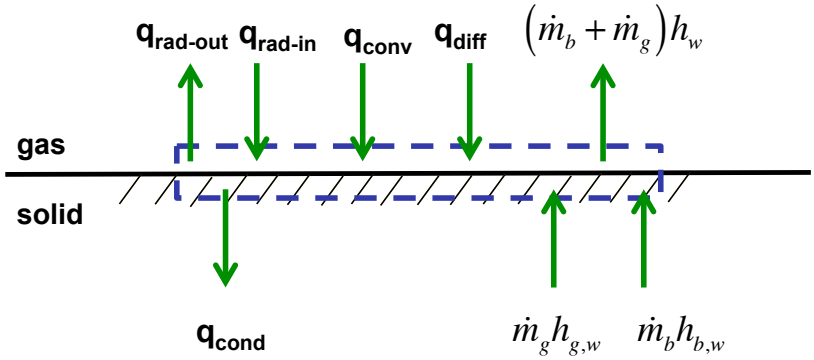

Figure 2.5: Energy balance at the ablating surface

glected, a radiative equilibrium boundary condition results as shown in Eq. 2.32. The wall temperature T_w is set by this boundary condition with emissivity ϵ for graphite set to 0.83 [86].

$$\mathbf{q}_{conv} + \mathbf{q}_{diff} = \sigma \epsilon {T_w}^4 \tag{2.32}$$

The contribution of conductive heat transfer is also evaluated by using a material response code MOPAR developed at the University of Michigan [62, 63, 7, 105]. MOPAR is coupled to LeMANS and can model heat conduction and pyrolysis processes within the material. It solves the energy equation shown in Eq. 2.33 using a Control Volume Finite Element Method (CVFEM)[9, 17].

$$\int_{cs} \dot{q''} dA - \int_{cs} \rho h v_{cs} dA + \frac{d}{dt} \int_{cs} \rho e dV = 0 \tag{2.33}$$

where $\dot{q''}$ is the internal heat flux, A is the area, e is the total energy, V is the volume, v_{cs} is the velocity of the grid and cs is the control surface. The second term in this equation, i.e., the grid convection term, allows for mesh movement that simulates surface recession of the ablating material. The grid convection term is set to zero for the purpose of this study. The reason for this is the negligible surface recession due

to the very low rate of carbon mass loss of graphite measured in the experiments. The carbon mass loss values are presented in Chapter V. The energy balance at the surface for this material response code is calculated using the boundary condition shown in Eq. 2.34.

$$q_{cond} + \rho_w h_w v_w = q_{conv} - \epsilon\sigma({T_w}^4 - {T_\infty}^4) - \dot{m}_b h_w \tag{2.34}$$

where T_∞ is the constant reservoir temperature. The grid convection $\rho_w h_w v_w$ and the ablation term $\dot{m}_b h_w$ are set to zero due to negligible surface recession. The coupled simulations begin with the converged flowfield solution obtained from LeMANS. LeMANS first calls MOPAR and an initial $\mathbf{q}_{cond}$ is calculated based on the total heat flux $\mathbf{q}$ from LeMANS (i.e. initial heat flux) from Eq. 2.34. Equation 2.33 is then solved for a user defined time and the wall temperature is calculated. MOPAR passes this wall temperature value to LeMANS and then the fluid equations are solved for a user-defined number of iterations. The temperature along the wall remains constant during this computation. MOPAR is then called again and the updated value along with the initial value of conductive heat flux are used as temporal boundary conditions to solve the time accurate energy equation. The process is repeated until a converged steady-state solution is obtained. In this study, the criterion for convergence is when the wall temperature values are the same between final and previous calls of MOPAR.

2.5 Summary

This chapter described the experimental and numerical techniques employed to study the gas-surface interactions that determine the aerothermal heating of a probe or hypersonic vehicle during its entry into a planetary atmosphere. The experiments

were conducted in a 30 kW Inductively Coupled Plasma (ICP) Torch Facility at the University of Vermont. The facility is designed to test scaled material samples in high enthalpy gas flows for simulation of planetary entry trajectory heating conditions. It is configured for operation with subsonic flow to simulate post shock conditions of high enthalpy flight. The gas-phase flow properties, i.e., the relative nitrogen atom number density and translational temperature, in the reacting boundary layer above the test article surface are measured using a two-photon laser induced fluorescence (LIF) technique. The stagnation region heat transfer is measured with a copper slug calorimeter and the surface temperature is measured using a two-color infrared optical pyrometer. Total mass removal rate from the sample is also quantified from pre- and post-test mass measurements.

A description of the numerical method along with the gas-surface interaction models used in this work is also presented. The numerical simulations are conducted using the Navier-Stokes CFD code LeMANS. The gas-surface interaction models implemented in LeMANS are a simplified binary catalytic atom recombination model and a general finite rate surface chemistry (FRSC) model. The catalytic atom recombination model can be used to study the effects of surface catalysis but could only be applied to a binary gaseous mixture of atoms and molecules. The FRSC model can be used to investigate the effects of surface catalysis as well as surface participating reactions and can be applied to multiple gaseous species.

The various wall temperature boundary conditions implemented in LeMANS were also discussed. The wall temperature could be set for isothermal condition i.e. heat transfer to the wall balances to maintain the prescribed wall temperature. It could be set for radiative equilibrium boundary condition where the convective and diffusive heat flux balance with the radiative heat flux to determine the wall temperature. It could also be calculated using a material response code MOPAR developed at the University of Michigan. MOPAR is coupled to LeMANS and can model heat

conduction and pyrolysis processes within the material.

CHAPTER III

Numerical Set Up

3.1 Introduction

The conditions in the ICP torch test chamber simulated by LeMANS are based on the conditions used in the experiments at the University of Vermont. This chapter presents a description of the numerical setup used in this study. The geometry of the the test article used in the experiments is provided. A description of surface reactions investigated to study gas-surface interaction processes is presented along with details on the composition of the gas-mixture considered.

3.2 Description of Test Conditions

The test conditions, i.e., facility inlet (ICP Torch exit) conditions and the graphite sample wall temperature simulated by LeMANS are based on the experiments conducted at the University of Vermont in order to compare the computational results with the experimental measurements. The simulations are performed for two sets of experimental conditions that are shown in Table 3.1. The experimental set up with the graphite test article in the nitrogen plasma in the test chamber of the ICP torch facility is shown in Fig. 2.2.

The test article for Configuration 1 is a 19 mm diameter graphite sample mounted

at a distance of 116 mm from the quartz tube exit. The article has an iso-q shape and is shown in Fig. 3.1. As the name suggests, an iso-q shape is designed to ensure uniform heat flux [33] across the face of the article. The free stream Knudsen number for these conditions is calculated to be 5.6 x 10^{-4} indicating that the flow is in the continuum regime. The diameter of the test sample is chosen to be the characteristic length. The free stream Reynolds number for this flow is 285 indicating that the flow is laminar. The characteristic length chosen is the length of the test article plus the length of the brass holder.

Table 3.1: Freestream and wall boundary conditions.

	Mass flow rate (kg/s)	Temperature, T_∞ [K]	Pressure [kPa]	Wall Temperature, T_{wall} [K]
Configuration 1	0.79x10^{-3}	7000	12.5	1591
Configuration 2	0.82x10^{-3}	7000	21.3	1598

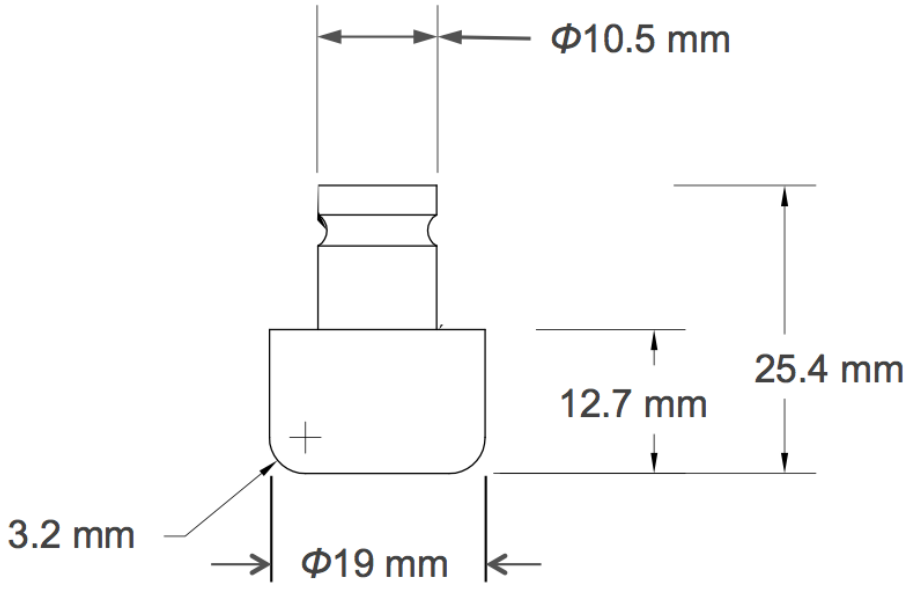

Figure 3.1: Test article geometry for experimental Configuration 1 listed in Table 3.1.

The test article for Configuration 2 is a 25 mm diameter graphite sample mounted at a distance of 90 mm from the quartz tube exit. The iso-q geometry of the test article for Configuration 2 is shown in Figure 3.2. The free stream Knudsen number for these conditions is calculated to be 2.5 x 10^{-4} indicating that the flow is in the continuum regime. The free stream Reynolds number for this flow is 295 indicating that the flow is laminar.

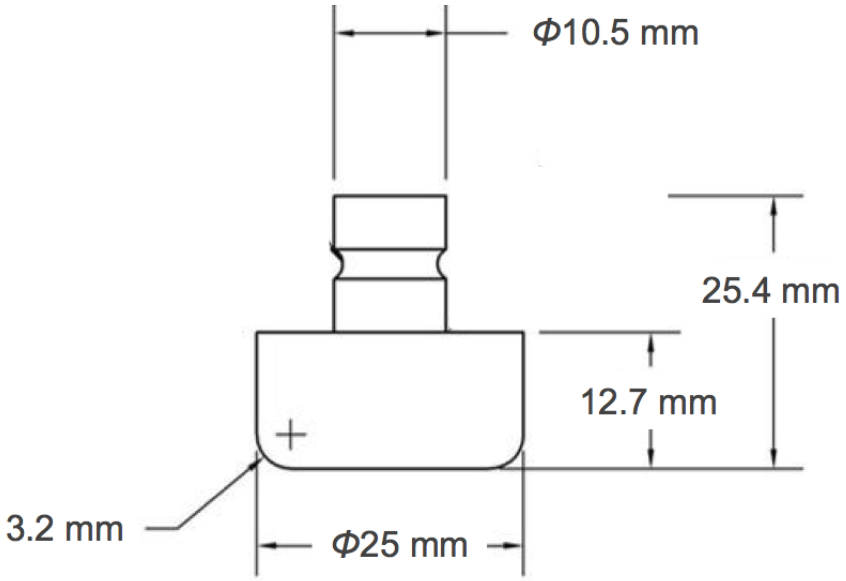

Figure 3.2: Test article geometry for experimental Configuration 2 listed in Table 3.1.

The equilibrium composition of the nitrogen gas mixture at the quartz tube exit for the given temperature and pressure [53] are calculated using the NASA program Chemical Equilibrium with Applications [66] (CEA). The prominent species present in the gas mixture for Configuration 1 are molecular and atomic nitrogen with mole fractions of 0.11 and 0.89, respectively. The species present in the gas mixture for Configuration 2 are again molecular and atomic nitrogen with mole fractions of 0.15 and 0.85, respectively. The results of the computations for both Configurations 1 and 2 show a significant level of nitrogen dissociation when chemical equilibrium is assumed at the quartz tube exit. A sensitivity study on inlet gas mixture composition is performed to analyze its effects on the parameters in the boundary layer and the

surface properties and is presented in Chapter V. A uniform velocity, temperature and density profile at the facility inlet, i.e., the quartz tube exit, is specified in the simulations for Configurations 1 and 2.

The flow at the inlet of the test chamber is non-uniform. It is difficult to measure the non-uniform inlet flow conditions experimentally. Therefore, the non-uniform inlet flow conditions were calculated at the University of Bologna using an ICP torch simulation code that models the plasma flow in the experimental tests. The code developed at the University of Bologna simulates the behavior of ICP torches using the commercial CFD code FLUENT© along with customized User Defined Scalar routines [13, 25, 24]. The simulation is performed under the assumption of laminar, chemical equilibrium flow and LTE conditions. It takes as input the facility geometry, details of the coils, and flow rate. The contours of translational temperature (left half) and stream function (right half) in the quartz confinement tube of the ICP torch obtained from the Bologna simulations are shown in Fig. 3.3. A comparison is performed to assess the effects of different inlet profiles, i.e., uniform and non-uniform, and is presented in Chapter IV.

3.3 Surface Reactions

The gas-surface interaction processes studied are the recombination of nitrogen atoms to molecules at the surface due to catalysis, and carbon nitridation where nitrogen atoms react with the surface carbon to form gaseous CN. Carbon nitridation is studied as sample mass loss is observed in the experiment and results for the surface recession are reported in the work by Lutz *et al*[53, 51]. Therefore, two sets of surface reactions are taken into account using the FRSC model. The first set is the surface reaction (shown in Eq. 3.1) that accounts only for the nitrogen atom recombination on the wall due to surface catalysis. Here, a gaseous nitrogen atom is adsorbed onto an available active site on the surface through an adsorption reaction. Then, another

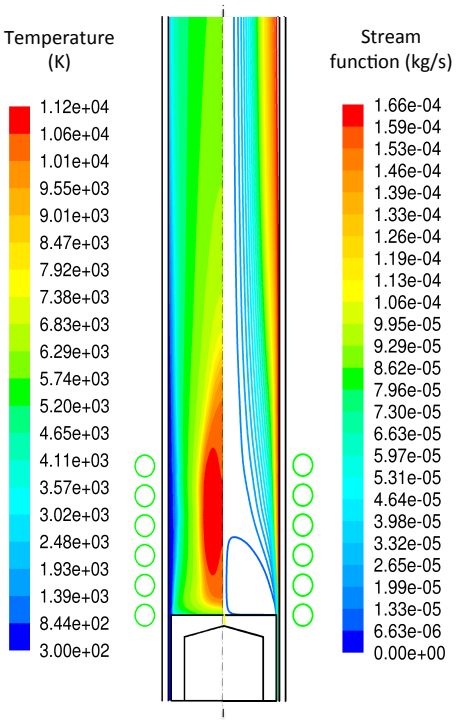

Figure 3.3: Translational temperature and stream function contours in the quartz confinement tube of the ICP torch obtained from the University of Bologna simulations.

nitrogen atom from the gas phase recombines with the adsorbed nitrogen atom to form a gaseous nitrogen molecule and leaves the active site. k_{f1} and k_{f2} in these reactions are the respective forward reaction rates.

$$
\begin{aligned}
&N + (s) \xrightarrow{k_{f1}} N(s)\text{: Adsorption } (E_{ad} = 0 \text{ J/mol}) \\
&N + N(s) \xrightarrow{k_{f2}} N_2 + (s)\text{: Eley-Rideal recombination } (E_{ER} = 0 \text{ J/mol})
\end{aligned} \tag{3.1}
$$

The second set of surface reactions (shown in Eq. 3.2) takes into account the nitrogen atom recombination on the wall due to surface catalysis along with the carbon nitridation reaction where the carbon from the surface reacts with the impinging nitrogen atoms. The Eley-Rideal recombination reaction is used to represent the process of carbon nitridation. k_{f1}, k_{f2} and k_{f3} in these reactions are the respective forward

reaction rates.

$$
\begin{aligned}
&N + (s) \xrightarrow{k_{f1}} N(s)\text{: Adsorption } (E_{ad} = 0 \text{ J/mol}) \\
&N + N(s) \xrightarrow{k_{f2}} N_2 + (s)\text{: Eley-Rideal recombination } (E_{ad} = 0 \text{ J/mol}) \\
&N + (s) + C_b \xrightarrow{k_{f3}} CN + (s)\text{: Eley-Rideal recombination } (E_{ad} = 0 \text{ J/mol})
\end{aligned} \tag{3.2}
$$

All the test cases are investigated using a constant reaction efficiency γ. The effective reaction efficiency for a gas phase reactant consumed in a surface reaction process is the net result of competing finite-rate processes. An analytic expression for constant reaction efficiency γ is derived both for the surface reaction set shown in Eq. 3.1 as well as for Eq. 3.2.

The constant reaction efficiency γ for a gas phase reactant k is defined as the fraction of collisions that it experiences with the surface resulting in its loss from the gas phase environment:

$$\gamma = \frac{-\dot{w}_k}{\Gamma_k} \tag{3.3}$$

where $\dot{w}_k$ is given by Eq. 2.20 and Γ_k is the impingement flux given by Eq. 2.23. The negative production rate $\dot{w}_k$ represents the consumption of the gas phase reactant at the wall. The constant reaction efficiency γ for the surface reactions in Eq. 3.1 can be calculated using Eq. 2.20, Eq. 2.22 and Eq. 2.23 as,

$$
\begin{aligned}
\gamma &= \frac{-\dot{w}_N}{\Gamma_N} \\
\gamma &= \frac{k_{f1} C_N \Phi_{s,e} + k_{f2} C_N \Phi_{s,N}}{(\bar{\nu}_N/4) C_N}
\end{aligned} \tag{3.4}
$$

The surface concentration of the adsorbed N atoms is obtained by equating Eq. 2.20

to zero for steady state conditions as,

$$\dot{w}_{N(s)} = 0 \tag{3.5}$$
$$k_{f1} C_N \Phi_{s,e} - k_{f2} C_N \Phi_{s,N} = 0$$
$$\Phi_s = \Phi_{s,e} + \Phi_{s,N}$$

Substituting for k_{f1} and k_{f2} from Eq. 2.24 and 2.26

$$\Rightarrow \Phi_{s,N} = \frac{\Phi_s S_0}{S_0 + \gamma_0}$$

Solving Eq. 3.4 and 3.5, the net constant reaction efficiency γ is given by,

$$\gamma = \frac{2 S_0 \gamma_0}{S_0 + \gamma_0} \tag{3.6}$$

The constant reaction efficiency γ for the surface reactions in Eq. 3.2 can be calculated using Eq. 2.20, Eq. 2.22 and Eq. 2.23 as,

$$\gamma = \frac{k_{f1} C_N \Phi_{s,e} + k_{f2} C_N \Phi_{s,N} + k_{f3} C_N \Phi_{s,e} \chi_{b1,c}}{(\bar{\nu}_N/4) C_N} \tag{3.7}$$

The bulk phase surface concentration $\chi_{b1,c}$ is one for a single bulk phase. Solving Eqs. 3.7 and 3.5, the net constant reaction efficiency γ is given by,

$$\gamma = \frac{2 S_0 \gamma_0 + \gamma_{CN} \gamma_0}{S_0 + \gamma_0} \tag{3.8}$$

The reaction efficiency γ_0 for surface catalysis, also referred to as catalytic efficiency of nitrogen atoms, is denoted by γ_N. It is defined as the ratio of the flux of

nitrogen atoms that recombine on the surface to form nitrogen molecules to the total flux of nitrogen atoms that impinge on the surface. A constant catalytic efficiency is achieved by setting S_0 equal to γ_0. The reaction efficiency for carbon nitridation, also referred to as carbon nitridation efficiency, is denoted by γ_{CN}. It is defined as the ratio of nitrogen atoms reaching the surface and combining with surface carbon atoms to the ratio of the total flux of nitrogen atoms that impinge on the surface. It is assumed in this investigation that all the carbon mass loss occurs due to the carbon nitridation reaction.

3.4 Description of Test Cases

The test cases considered in this study to determine the effects of gas-surface interaction processes are shown in Table 3.2.

Table 3.2: Test cases.

Case	Catalytic efficiency γ_N	Carbon nitridation efficiency γ_{CN}	Effective reaction efficiency γ
Case 1	0	0	0
Case 2	0.07	0	0.07
Case 3	0.07	0.005	0.0725
Case 4	1	0	1

The catalytic efficiency γ_N is set to zero for a non-catalytic wall and is set to 1 for a fully catalytic wall. The partially catalytic wall condition of $\gamma_N = 0.07$ is based on an experimentally determined value [40] for pure carbon. The catalytic efficiency was obtained from the comparison of measured data of heat transfer to the carbon specimen in subsonic jets of dissociated nitrogen with the numerical computations of heat transfer. The value $\gamma_{CN} = 0.005$ for Case 3 is set based on a value determined by Driver and Maclean [**?**]driver. It is obtained from a comparison between data from arc jet tests performed for Phenolic Impregnated Carbon Ablator (PICA) in nitrogen and results from computational simulations. The nitridation efficiency of γ_{CN} pro-

duces good predictions of both heat transfer and recession rate when both reactions, i.e., carbon nitridation and nitrogen atom recombination to nitrogen molecules due to catalysis, are included in the computations [32]. It should be noted that γ_{CN} is dependent on the type of carbon used as well as the experimental conditions.

Case 1 represents a wall where no surface chemistry is accounted for and is treated as non-catalytic. The surface chemistry for Cases 2 and 4 is defined by the reactions shown in Eq. 3.1 and for Case 3, it is defined by Eq. 3.2. The effective reaction efficiency γ for Cases 2 and 4 is calculated using Eq. 3.6 and for Case 3, Eq. 3.8 is used.

3.5 Flowfield Thermochemical model

For the analysis where only catalytic nitrogen atom recombination at the surface is considered, the gas mixture is composed of atomic and molecular nitrogen and only the following dissociation-recombination reaction is considered:

$$\begin{aligned} N_2 + M &\rightleftharpoons 2N + M \\ M &= N, N_2 \end{aligned} \tag{3.9}$$

The mixture transport properties can be calculated using either Gupta's mixing rule [44] or Wilke's semi-empirical mixing rule [106]. A comparison is performed between the two models for Eq 3.9 and the results are presented here. Figures 3.4 and 3.5 present the stagnation line profiles for translational temperature and nitrogen atom number density, respectively. The total heat flux for these cases is plotted in Fig. 3.6. The total heat flux is the summation of the translational convective heat flux, vibrational convective heat flux and diffusive heat flux. The simulation is performed for a fully catalytic wall ($\gamma_N = 1$) for the test conditions for Configuration 1.

It can be seen that the temperature and nitrogen atom number density along the

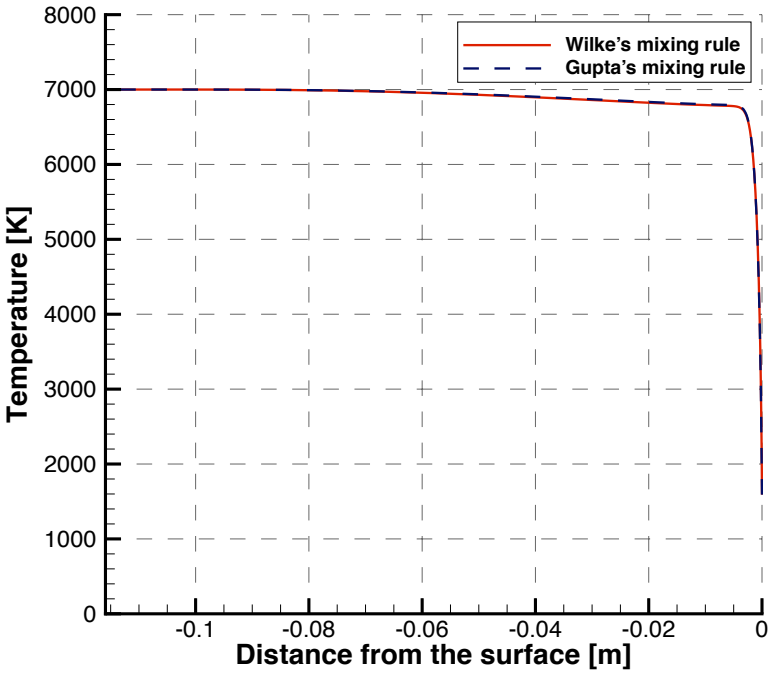

Figure 3.4: Comparison of translational temperature along the stagnation line.

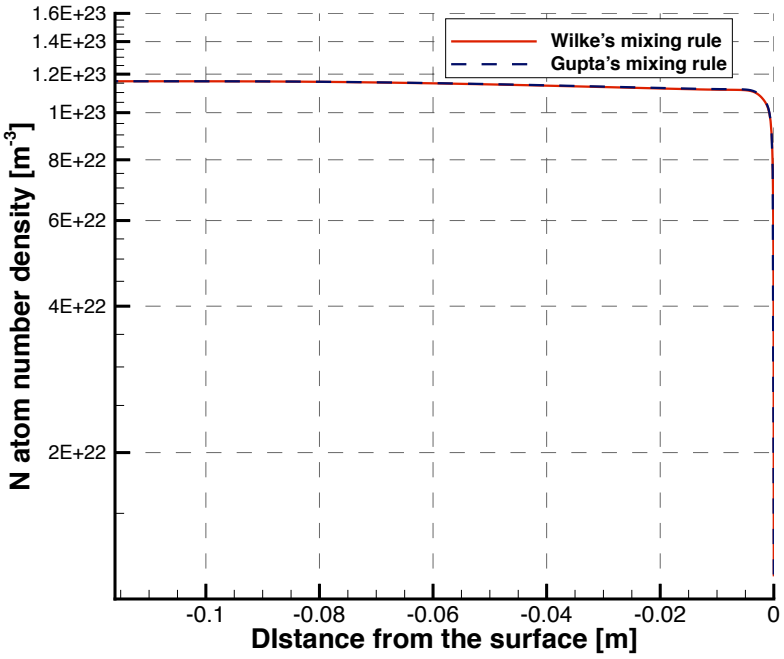

Figure 3.5: Comparison of N-atom number density along the stagnation line.

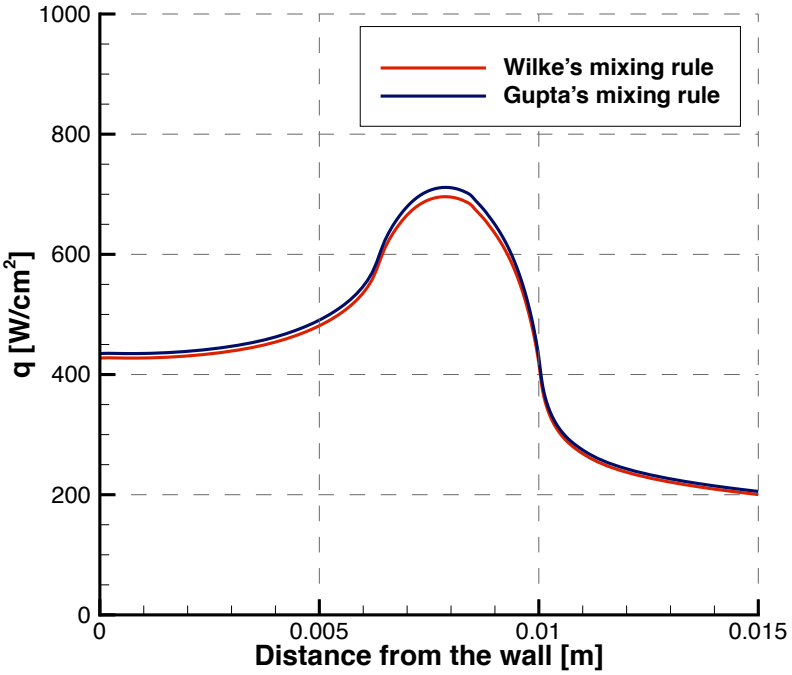

Figure 3.6: Heat flux.

stagnation line are similar for both mixing rules. The heat transfer for the Wilke's mixing rule is within 2% of the results for the Gupta's mixing rule. A negligible difference is seen in the results of the two models. Therefore, Wilke's semi-empirical mixing rule is used in the remainder of study.

For the analysis where both catalytic nitrogen atom recombination and carbon nitridation reaction at the surface is considered, the gas mixture is composed of atomic nitrogen, molecular nitrogen, atomic carbon and the CN molecule and considers the following dissociation-recombination reactions:

$$\begin{aligned} N_2 + M &\rightleftharpoons 2N + M \\ CN + M &\rightleftharpoons C + N + M \\ M &= N, N_2, C, CN \end{aligned} \tag{3.10}$$

3.6 Summary

A description of the test conditions used by LeMANS to simulate the high enthalpy flow in the test chamber of the ICP torch facility is presented. The conditions are based on the experiments conducted at the University of Vermont for comparison of computed results with the experimental measurements. The flow at the inlet of the test chamber i.e. the ICP torch exit, is non-uniform and it is difficult to measure the non-uniform inlet flow conditions experimentally. Therefore, the non-uniform inlet flow conditions were calculated at the University of Bologna using an ICP torch simulation code that models the plasma flow in the ICP torch used in the experimental tests. A detailed description of the Bologna simulations is provided in this chapter. This non-uniform profile is used to obtain the numerical solution and is compared with that computed using the uniform inlet values in this study. The results of this comparison are provided in Chapter IV.

The surface chemical reactions along with the reaction efficiencies used in this study are also presented. This chapter provided the formulation of the effective reaction efficiency γ for the respective surface reactions. The gas mixture considered along with the respective dissociation-recombination reactions is presented. The results are presented from a comparison performed between two models for calculating mixture transport properties, i.e., Gupta's mixing rule and Wilke's semi-empirical mixing rule. The results show a negligible difference between the two models. Wilke's semi-empirical mixing rule is used in the rest of this thesis for calculating transport properties.

CHAPTER IV

Flowfield Analysis

4.1 Introduction

The numerical simulations are influenced by various factors ranging from the mesh of the flow field to the geometry of the experimental facility. This chapter presents an analysis of these factors and their effect on the gas flow parameters and surface properties analyzed in this investigation. In the first section, a grid convergence study is performed to ensure the numerical solution is not affected by the grid of the flowfield. It is followed by an assessment of the sensitivity of the flow around the graphite sample to the area of the test chamber included in the simulations. The second section of the chapter is focussed on discussing effects of the physics of the gaseous flowfield in addition to the impact of a non-uniform inlet profile on the boundary layer parameters.

4.2 Grid convergence study

A grid convergence study is performed to ensure the grid independence of the numerical solutions. The size of the grids used in the study are shown in Table 4.1 along with the run time and the number of processors used for each simulation. Grid 1 is the finest grid followed by a coarser Grid 2 and the coarsest Grid 3. The grids are

coarsened by reducing the number of nodes in each segment by a factor of $\sqrt{2}$. The size of the first cell away from the wall is $10^{-6}m$. The boundary conditions assigned for these simulations are shown in Fig. 4.1.

Table 4.1: Different grids used.

Grid	Number of cells	Run time (hours)	Number of processors
Grid 1	56000	107	48
Grid 2	28000	41	48
Grid 3	14000	22	48

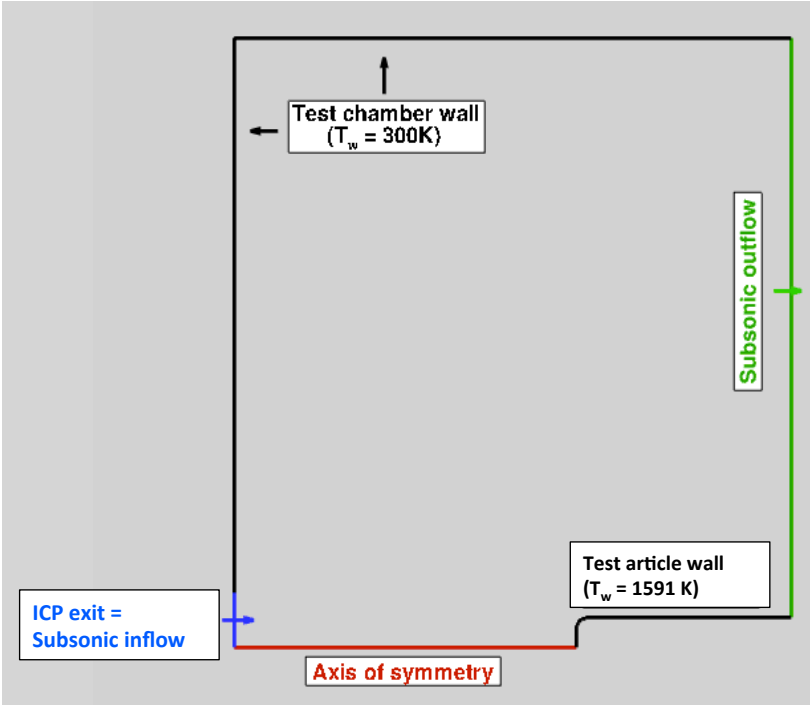

Figure 4.1: Boundary conditions for the grids listed in Table 4.1.

All the results are obtained for a thermal equilibrium flowfield (explained in Section 4.3.1), with for a non-catalytic test article and test chamber wall ($\gamma = 0$). The simulations for this study are performed for the experimental configuration 1 listed in Table 3.1. The stagnation line profiles for translational temperature and nitrogen atom number density for each grid are shown in Figs. 4.2 and 4.3, respectively. The radial profile results for translational temperature and nitrogen atom number

density are shown in Figs. 4.4 and 4.5, respectively. The radial profiles are plotted at a distance of 1.52 mm from the test article surface to coincide with experimental measurements. The temperature profiles for all three grids overlap in the boundary layer, both for the axial and radial profiles as shown in Figs. 4.2 and 4.4, respectively. The variation in the axial and radial profiles for both Grids 2 and 3 is within 1% of the respective translational temperature profile for Grid 1. The variation in both the axial and radial nitrogen atom number density profiles (Figs. 4.3 and 4.5) for Grid 2 is within 1% of the results for Grid 1. The variation in both the axial and radial profiles for Grid 3 is within 2% of the nitrogen atom number density results for Grid 1.

The heat transferred to the surface is plotted in Fig. 4.6. The variation in the results for Grid 2 is within 1% of the results for Grid 1. The variation in the results for Grid 3 is within 3% of the results for Grid 1. Based on these results, Grid 2 is chosen for further analysis.

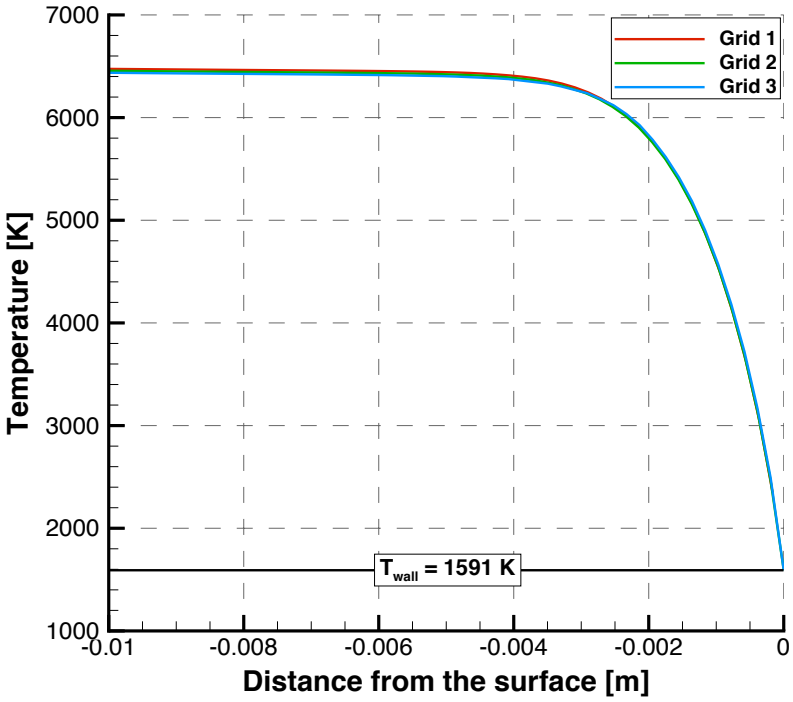

Figure 4.2: Comparison of translational temperature along the stagnation line for the simulations on the grids listed in Table 4.1 .

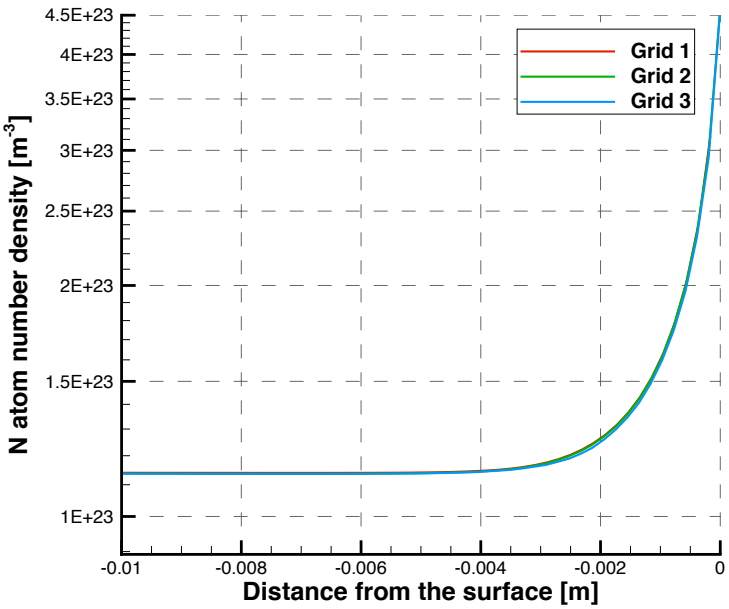

Figure 4.3: Comparison of N-atom number density along the stagnation line for the simulations on the grids listed in Table 4.1 .

4.2.1 Effect of the test chamber side wall

In this section, the effect of the sidewall of the test chamber on the flowfield and boundary layer parameters is investigated. This study is performed to assess the sensitivity of the flow around the graphite sample to the size of the test chamber included in the simulations. The entire width of the test chamber is included in Grid 1 whereas only part of the test chamber is considered in Grid 2. The size of the grids used are listed in Table 4.2 along with the run time and the number of processors used for each simulation. The boundary conditions for Grid 2 are shown in Fig. 4.7. In addition, the stagnation point is also shown where the heat flux and the surface temperature are measured. The stagnation point is the point on the surface where the flow velocity is zero. All the results are obtained for a thermal equilibrium flowfield for a non-catalytic test article and test chamber wall ($\gamma = 0$).

The stagnation line translational temperature and nitrogen atom number density profiles are presented in Figs. 4.8 and 4.9, respectively. The corresponding radial

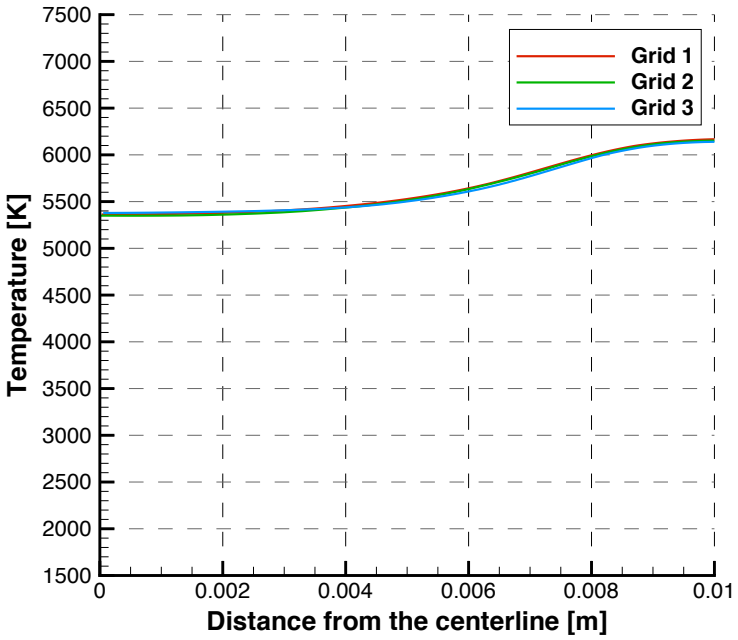

Figure 4.4: Comparison of translational temperature in the radial direction for the simulations on the grids listed in Table 4.1.

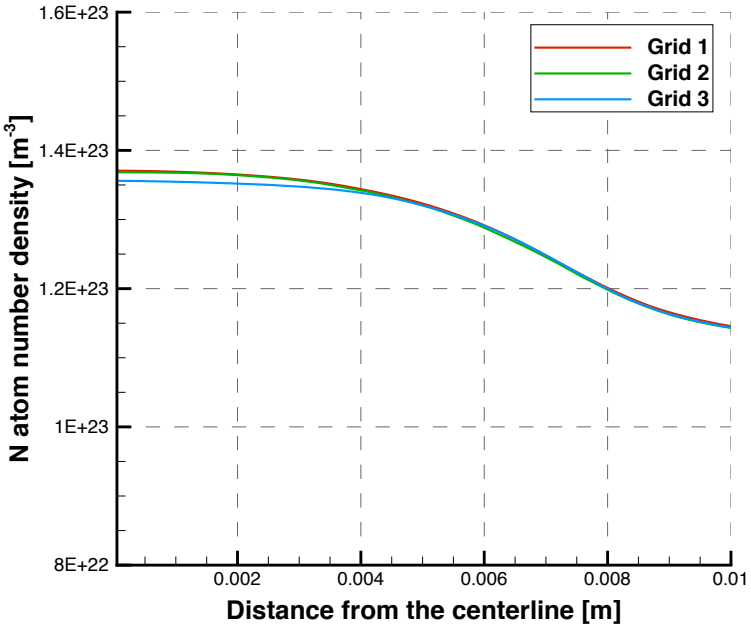

Figure 4.5: Comparison of N-atom number density in the radial direction for the simulations on the grids listed in Table 4.1.

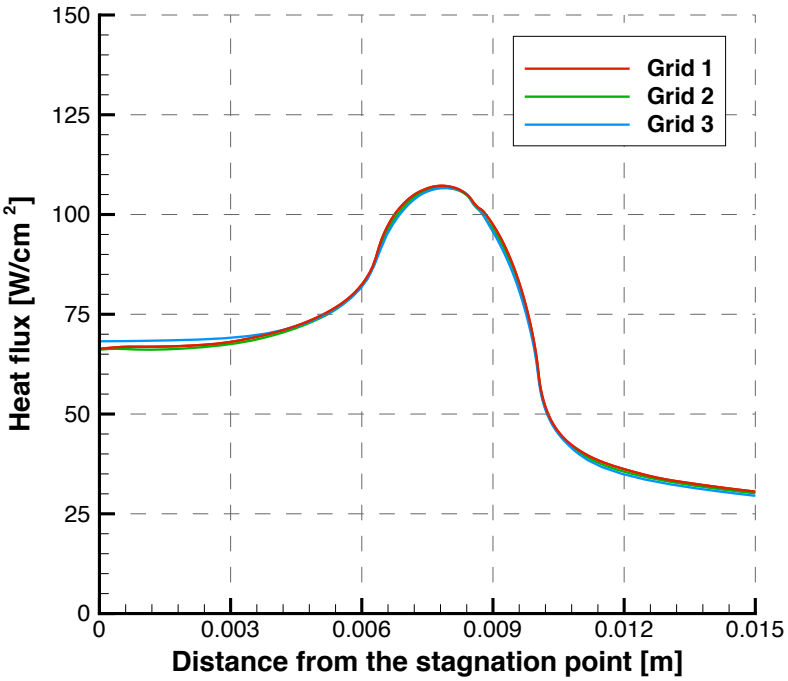

Figure 4.6: Heat flux for the simulations on the grids listed in Table 4.1.

Table 4.2: Grid size.

Grid	Number of cells	Run time (hours)	Number of processors
Grid 1	28000	41	48
Grid 2	20000	4	48

profiles are shown in Figs. 4.10 and 4.11, respectively. The variation in both the axial and radial translational temperature profiles for Grid 2 is within 1% of the respective results for Grid 1. The variation in both the axial and radial nitrogen atom number density profiles for Grid 2 is within 1% of the respective results for Grid 1. The heat transferred to the surface is plotted in Fig. 4.12. The results for both the grids overlap. The variation in results for Grid 2 is within 1% of the heat flux results for Grid 1.

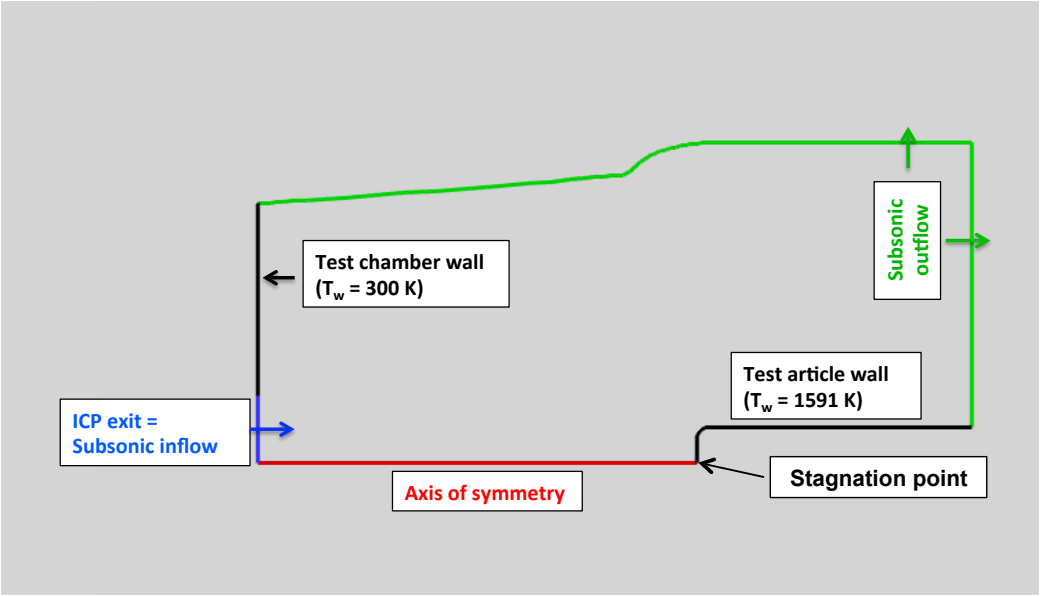

Figure 4.7: Boundary conditions for Grid 2.

Therefore, it can be concluded that excluding the side wall from the simulations does not affect the flow parameters and the surface properties for the graphite sample. It can be seen in Table 4.2 that the run time for Grid 2 is 4 hours, more than 10 times smaller than that for Grid 1, i.e., 41 hours. The simulations are much faster when Grid 2 is used even though there is only a minor reduction (8000 cells less than Grid 1) in number of cells for Grid 2 as compared to Grid 1. The reason for this is the different boundary conditions. For the case of Grid 1, the side test chamber wall is included in the simulations (Fig 4.1) whereas for the case of Grid 2, it is not included in the simulations and a subsonic outflow boundary is set instead (Fig 4.7). Therefore,

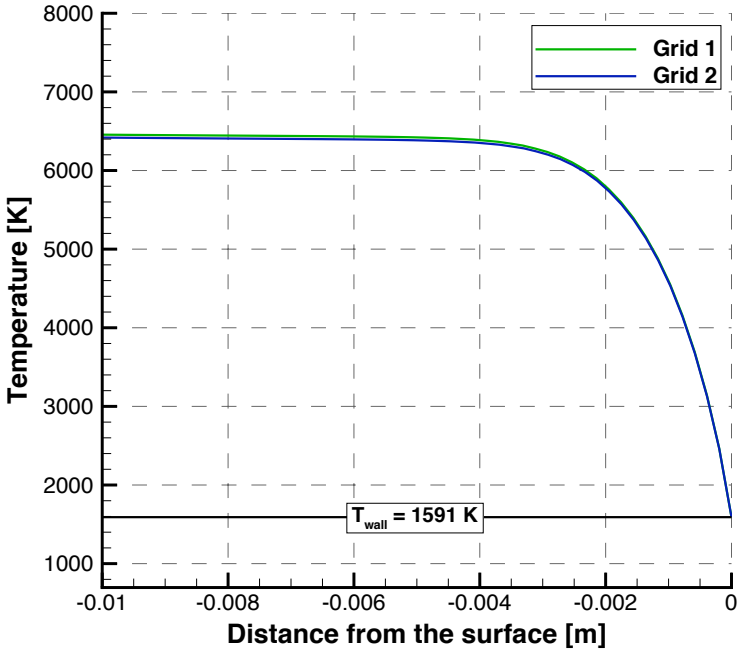

Figure 4.8: Comparison of translational temperature along the stagnation line for the simulations on the grids listed in Table 4.2.

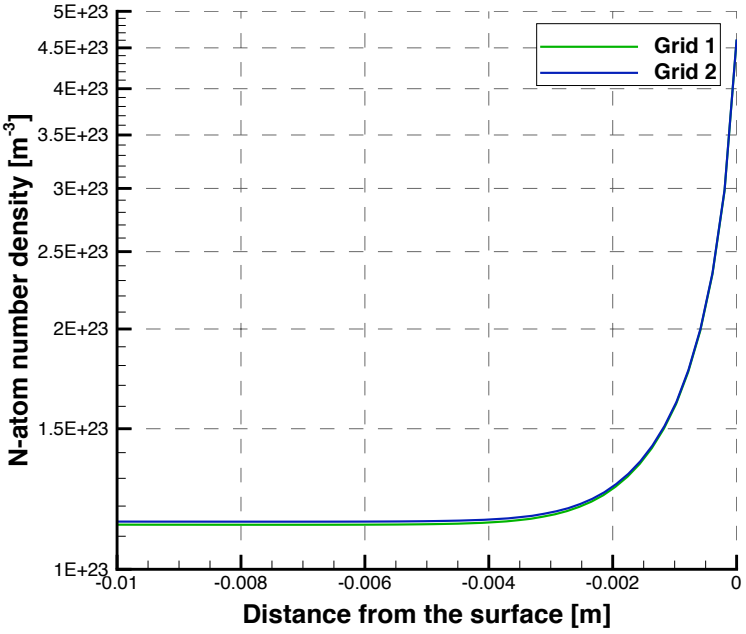

Figure 4.9: Comparison of N-atom number density along the stagnation line for the simulations on the grids listed in Table 4.2.

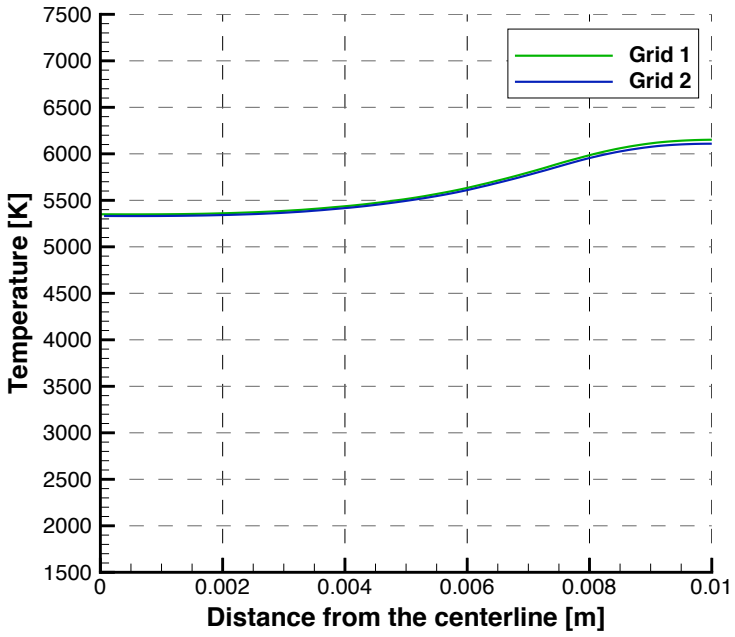

Figure 4.10: Comparison of translational temperature in the radial direction for the simulations on the grids listed in Table 4.2.

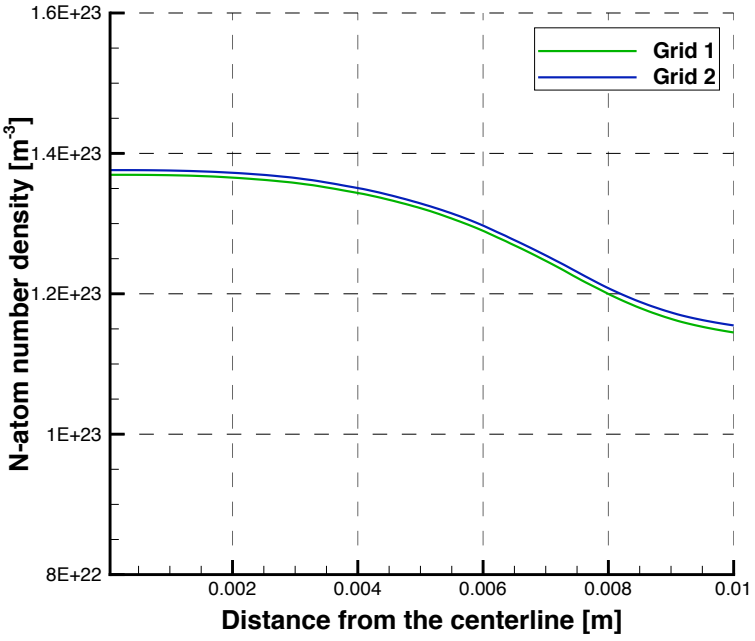

Figure 4.11: Comparison of N-atom number density in the radial direction for the simulations on the grids listed in Table 4.2.

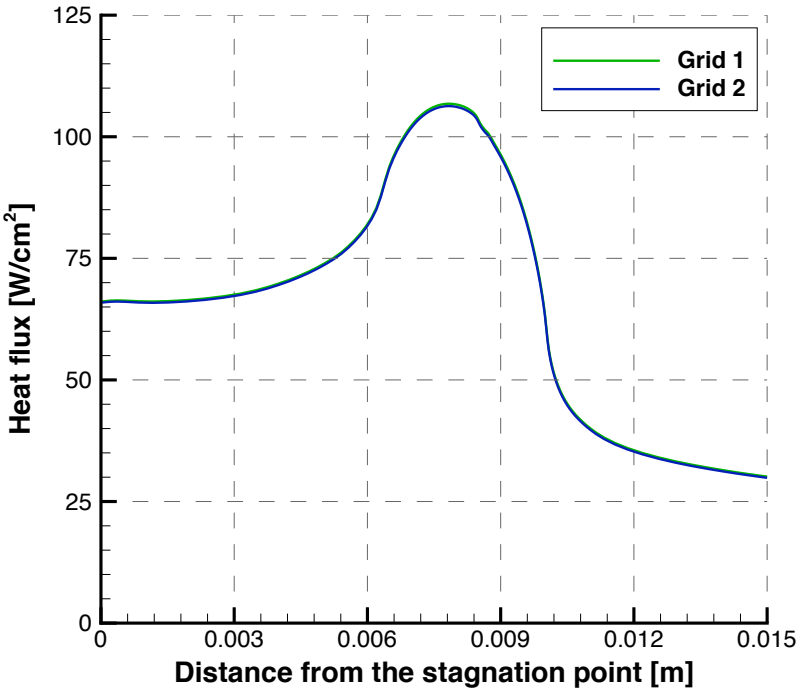

Figure 4.12: Heat flux for the simulations on the grids listed in Table 4.2.

for the simulation using Grid 1, there is a recirculation region that develops as the flow progresses. This recirculation region is contained by the test chamber wall and takes a long time to leave the test chamber. For the simulation using Grid 2, there is no test chamber wall at the side to constrict the flow as it progresses. Therefore, the simulations for Grid 2 take significantly less time for the flow to develop. Therefore, Grid 2 is used for the rest of the analysis for configuration 1. A picture of Grid 2 is shown in Figure 4.13. A similar grid with 22,000 cells is created for configuration 2 and is used for the analysis with its respective conditions.

4.3 Sensitivity to nature of flowfield

Computational models can be used for accurately predicting the aerothermal environment of the vehicle TPS during (re)-entry but they can be used to perform such analysis only after they have been validated to accurately predict the flow in the test facility and are validated with experimental results from the facility [107]. In order to

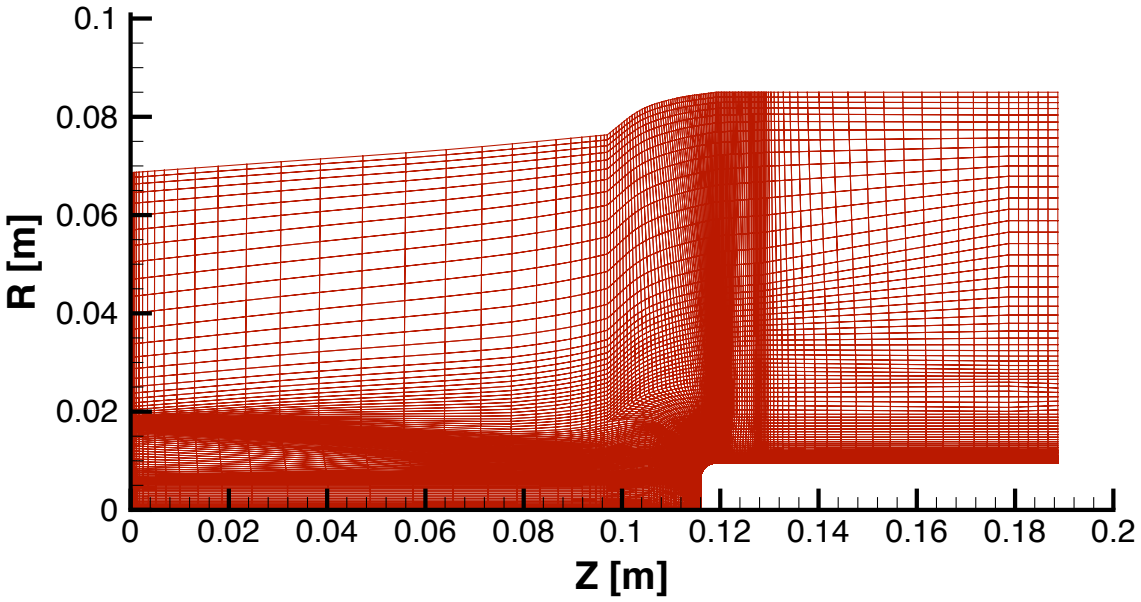

Figure 4.13: Computational grid for configuration 1.

predict the flow in the test chamber of the ICP torch facility accurately, it is required to simulate flow in the test facility as closely as possible. This section identifies the flow components of the experimental tests that could influence the properties of the parameters in the region of interest. In the first section, the effect of different physics of the flowfield is investigated. The effect of the nature of the inlet profile on the flowfield and boundary layer parameters is analyzed in the second section.

4.3.1 Effect of Themochemical Non-Equilibrium

An investigation is performed in this section to characterize the nature of the gaseous flowfield in the test chamber of the ICP torch facility. To maintain thermal equilibrium in a gas for a given thermodynamic state (e.g. temperature and pressure), the molecules collide and exchange energy continuously without change in total energy [75]. For a gas mixture to be in chemical equilibrium, the forward and backward reactions occur such that the composition of the mixture does not change for a given thermodynamic state. If there is a change in the thermodynamic state of the flowfield, the gas readjusts to a new equilibrium state through a redistribution

of energy within the internal modes. This requires a certain number of molecular collisions for each energy mode and therefore, the establishment of equilibrium takes some time referred to as the relaxation time. For a molecule, the internal modes are the translational, rotational, vibrational and electronic modes whereas an atom possesses translational and electronics modes. The number of collisions required for each energy mode to reach equilibrium is called the collision number $Z_{process}$ for each process [21]. The general relation between collision numbers for each process is given by,

$$Z_{translational} < Z_{rotational} < Z_{vibrational} < Z_{electronic} < Z_{dissociation}$$

The translational and rotational energy modes usually require relatively fewer collisions to reach equilibrium [77]. All the internal modes are at the same temperature for a gas in equilibrium. Translational and rotational modes are assumed to be equilibrated in this study and are described by the same temperature. For nitrogen at room temperature, the rotational collision number is approximately 3 to 6 [75]. The vibrational and chemical processes respond slowly to a change in the flowfield and can be in nonequilibirium. A nonequilibrium state for a process exists in any reference volume in the flowfield if the molecule does not undergo $Z_{process}$ collisions before leaving that volume. The respective internal energy modes and the chemical process need to be excited to contribute towards the total energy of a molecule [75, 4]. The rotational modes are excited for nitrogen at a characteristic rotational temperature of 2.9 K and hence these modes are fully excited at room temperature. The vibrational modes for the nitrogen molecule are excited for a characteristic vibrational temperature of 3390 K. For 1 atm pressure, molecular nitrogen N_2 starts dissociating at 4000 K and is completely dissociated at 9000 K making the flow in this temperature range conducive for chemical reactions [5]. For this study, the temperature of the

nitrogen gas at the ICP torch exit is 7000 K and the pressure is in the range of 12 to 20 kPa. These conditions are favorable to excite the vibrational energy mode within the molecules as well as cause dissociation.

Therefore, the flowfield is investigated for flow in thermal equilibrium, thermal nonequilibrium, and thermochemical nonequilibrium. Table 4.3 presents the flow physics models simulated along with the surface boundary conditions, the run time and the number of processors for each simulation. The respective flow physics models for each state are defined as follows. A flow in thermal equilibrium (TE) refers to the simple condition where only equilibrated translational and rotational energy modes are considered. It is assumed for this condition that the vibrational energy mode is not excited and the flow is not chemically reacting. Thermal nonequilibrium (TNE) means that the flow considers vibrational nonequilibrium and the flow is not chemically reacting. In this case, the finite rate of vibrational relaxation is accounted for. The translational and rotational modes are assumed to be equilibrated. Thermochemical nonequilibrium (TCNE) means that the flow considers both vibrational and chemical nonequilibrium. With these assumptions, the finite rate of chemical relaxation is included, along with vibrational relaxation. The analysis is performed for test conditions of configuration 1 with a non-catalytic wall boundary condition for the test chamber as well as the test article wall. Figure 4.14 presents the stagnation line profiles with translational temperature in Fig. 4.14(a) and nitrogen atom number density in Fig. 4.14(b), respectively. The radial profiles for translational temperature and nitrogen atom number density are shown in Fig. 4.15. The total heat flux for these cases is plotted in Fig. 4.16(a) along with the vibrational convective heat flux in Fig. 4.16(b). The total heat flux is the summation of the translational convective heat flux, vibrational convective heat flux and diffusive heat flux. For Case 1, the translational convective heat flux is the total heat flux. The total heat flux for Cases 2 and 3 is the summation of the translational convective heat flux and vibrational con-

vective heat flux. The diffusive heat flux is zero for all cases as the wall is considered non-catalytic.

Table 4.3: Flow physics models.

Case	Flow field condition	Catalytic efficiency γ	Run time (hours)	Number of processors
Case 1	Thermal equilibrium (TE)	$\gamma = 0$	4	48
Case 2	Thermal nonequilibrium (TNE)	$\gamma = 0$	6	48
Case 3	Thermochemical nonequilibrium (TCNE)	$\gamma = 0$	8	48

It can be seen from these results that simulations for Cases 1 and 2 show no significant difference both for translational temperature and nitrogen atom number density. The reason for this agreement between the two cases is that at this high temperature of 7000 K, the flow is mostly dissociated. The fraction of total energy contained in the vibrational mode of the molecules is therefore small, and hence the vibrational nonequilibrium effects are negligible for a non-catalytic wall. The heat transferred is higher for Case 2 in comparison with Case 1 due to the contribution from vibrational heat flux. For the case of thermochemical nonequilibrium, i.e., Case 3, a higher temperature is observed in both the axial and radial profiles. The nitrogen atom number density profiles for this case show a lower level of nitrogen atoms in comparison with Cases 1 and 2. The reason for this loss is explained by a small but finite net rate of recombination reactions in the chemically reacting nonequilibrium flow. Since the flow is chemically reacting, the dissociation-recombination reaction given by Eq. 3.9 is taken into account. Due to the high concentration of nitrogen atoms in the freestream, the recombination process dominates over dissociation. The influence of this chemical nonequilibrium can be seen in the increased wall heat flux. As a result of recombination, some energy is transferred into the vibrational mode because of the addition of nitrogen molecules. Its effect can be seen in the increased

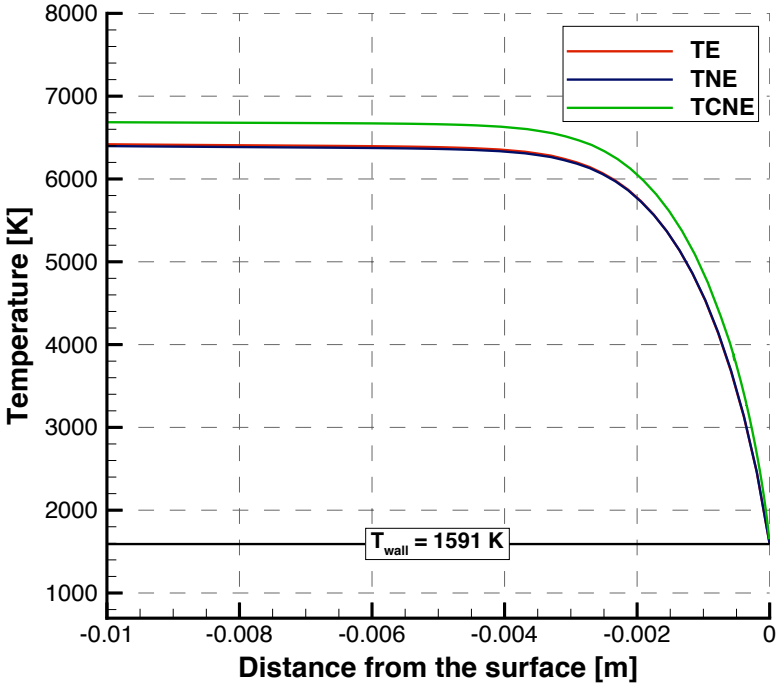

(a) Translational temperature

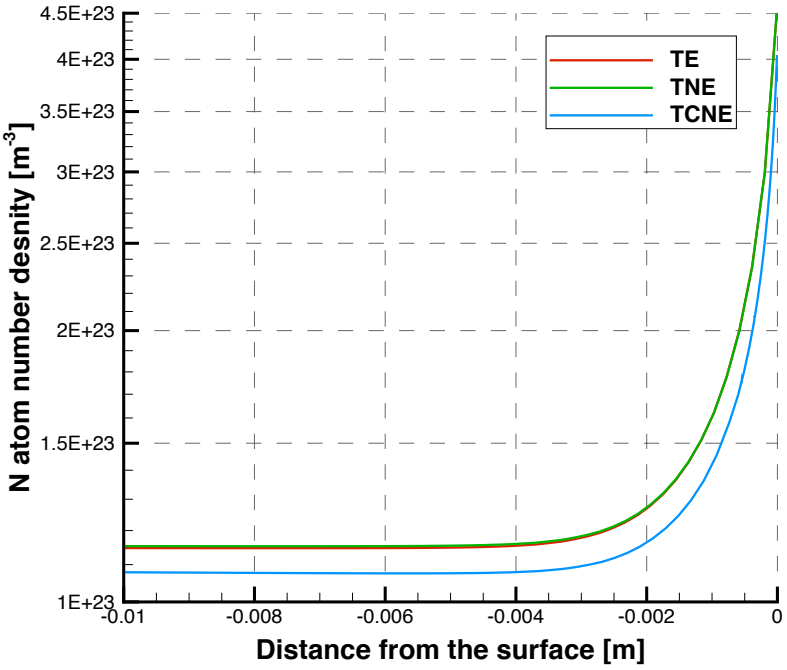

(b) N-atom number density

Figure 4.14: Comparison of translational temperature and N-atom density along the stagnation line for different physical models listed in Table 4.3.

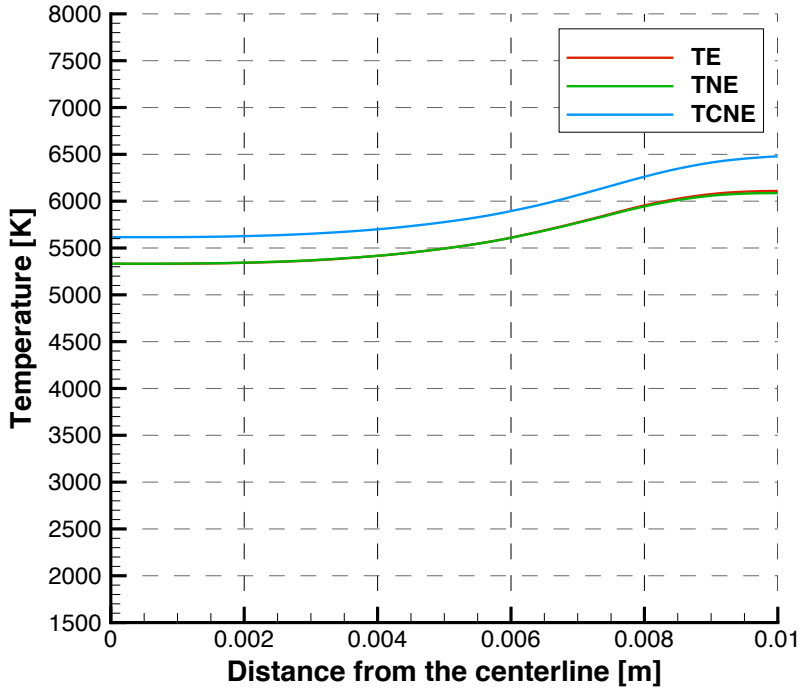

(a) Translational temperature

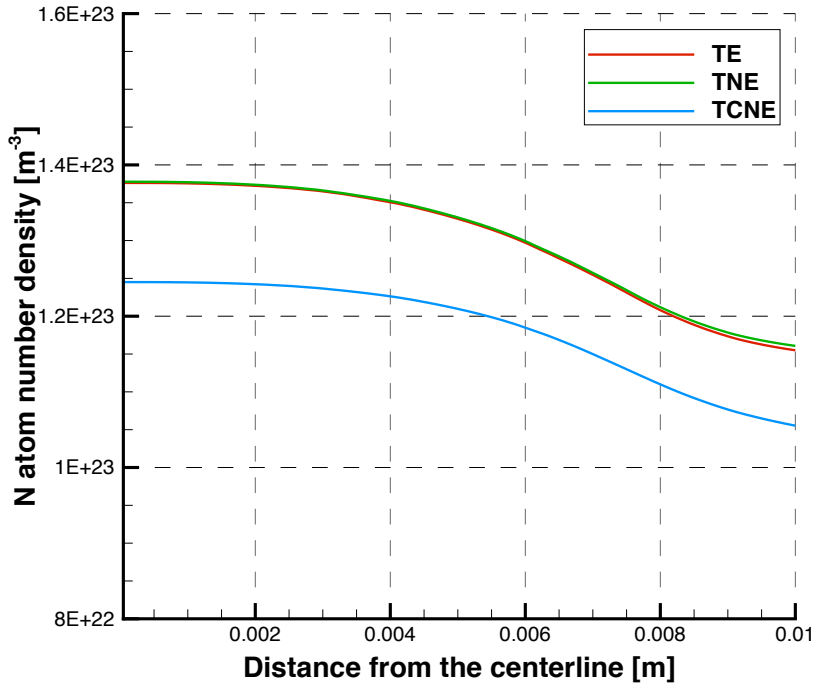

(b) N-atom number density

Figure 4.15: Comparison of translational temperature and N-atom density in the radial direction for different physical models listed in Table 4.3.

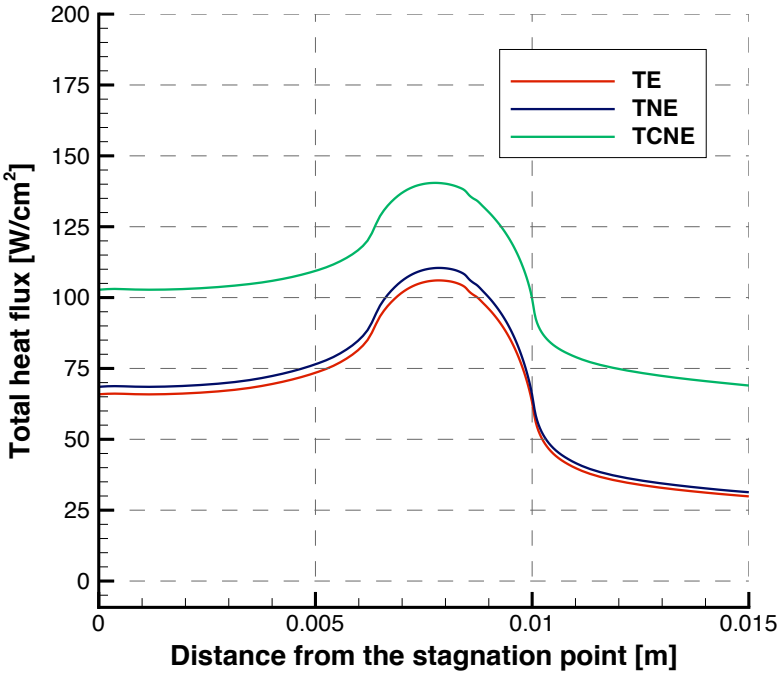

(a) Total heat flux

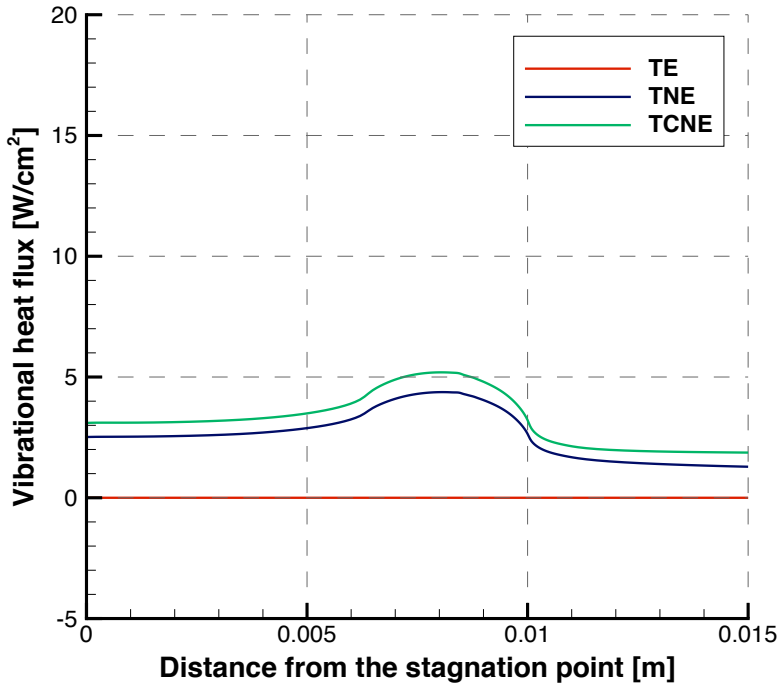

(b) Vibrational convective heat flux

Figure 4.16: Heat flux for the simulations for different physical models listed in Table 4.3.

vibrational convective heat flux for thermochemical nonequilibrium as compared to thermal nonequilibrium. The results from this analysis show that it is important to include the effects of vibrational and chemical nonequilibrium for the given flowfield conditions. Therefore, the thermochemical nonequilibrium flow physics model is used for the rest of the analysis in this thesis.

4.3.2 Effect of uniform and non-uniform inlet conditions

In this section, the results are discussed for the study performed to assess the effects of different inlet profiles, i.e., uniform and non-uniform, on the species concentration and temperature gradients near the material surface, and on the heat transfer to the material surface. As described in Chapter II, hot nitrogen plasma is generated in the ICP torch and flows into the test chamber of the facility through the ICP torch exit. The exit of the ICP torch is the inlet to the test chamber of the facility flow where the sample is tested. A more accurate non-uniform flow profile is used for the ICP torch exit, to obtain the numerical solution. This solution is compared with that computed using the uniform inlet values.

Table 4.4: Inlet and wall boundary conditions.

	Mass flow rate (kg/s)	Temperature, T_∞ [K]	Pressure [kPa]	Wall Temperature, T_{wall} [K]
Inlet 1	1x10^{-3}	7000	12.5	1591
Inlet 2	1x10^{-3}	Non-uniform profile	12.5	1591

The simulations are run for the two inlet profiles shown in Table 4.4. Inlet 1 corresponds to the estimated uniform inlet conditions based on experimental measurements. The equilibrium composition of nitrogen gas mixture at the quartz tube exit for the given temperature and pressure [53] of Inlet 1 are calculated for the uniform inlet using the NASA program Chemical Equilibrium with Applications (CEA) [66]. Inlet 2 corresponds to the non-uniform inlet conditions calculated at the Uni-

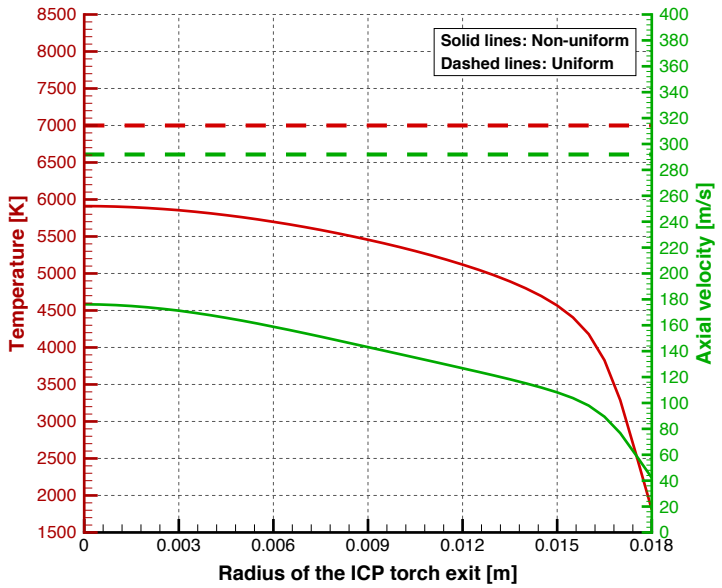

(a) Translational temperature (red) and Axial velocity (green)

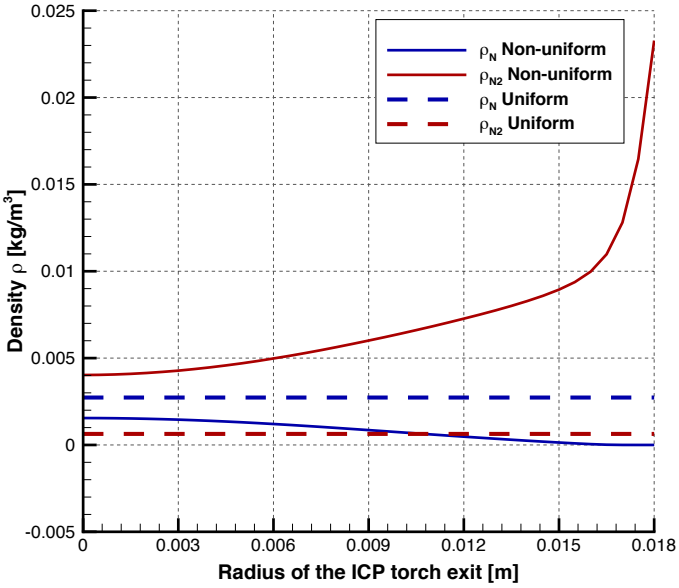

(b) Species density

Figure 4.17: Uniform and non-uniform inlet profiles of temperature, axial velocity and species density for Inlet 1 and 2 listed in Table 4.4.

versity of Bologna using an ICP torch simulation code as described in Chapter III. The non-uniform inlet values are computed for a pressure of 10 kPa in the Bologna simulations. The results have been scaled to a pressure of 12.5 kPa as the experimental tests were conducted at this pressure. The scaled non-uniform density profile is calculated using CEA for 12.5 kPa and temperature profile obtained through the Bologna simulation results. The uniform and non-uniform profiles for Inlet 1 and 2 listed in Table 4.4 are shown in Fig. 4.17 with temperature and axial velocity in Fig. 4.17(a) and species density in Fig. 4.17(b), respectively. Only the axial velocity is used in the computations as the radial velocity is negligible. It can be seen from the species density profiles for the non-uniform inlet shown in Fig. 4.17(b) that molecular nitrogen is the predominant species in the mixture with small amounts of atomic nitrogen resulting from weak dissociation. Molecular nitrogen is present in small amounts in the mixture for the uniform inlet with atomic nitrogen being the predominant species as a result of strong dissociation of nitrogen due to a higher inlet temperature as shown in Fig. 4.17(a).

The flow physics model used is thermochemical nonequilibrium and a fully catalytic wall is used for the species boundary condition. Figure 4.18 shows a comparison of translational temperature contours between the results for the non-uniform (top half) and the uniform inlet profiles (bottom half). These contours show the effect of the inlet profiles, on the flow field around the graphite sample. The front of the graphite sample is exposed to a varying temperature for the non-uniform inlet whereas the uniform temperature is maintained in front of the graphite sample for a uniform inlet. The velocity streamlines show that the flow enters from the ICP torch exit on the left and impinges on the graphite sample at the right. The translational temperature contours in the quartz confinement tube of the ICP torch obtained from the Bologna simulations and in the test chamber of the facility obtained from facility simulations using LeMANS are shown in Fig. 4.19.

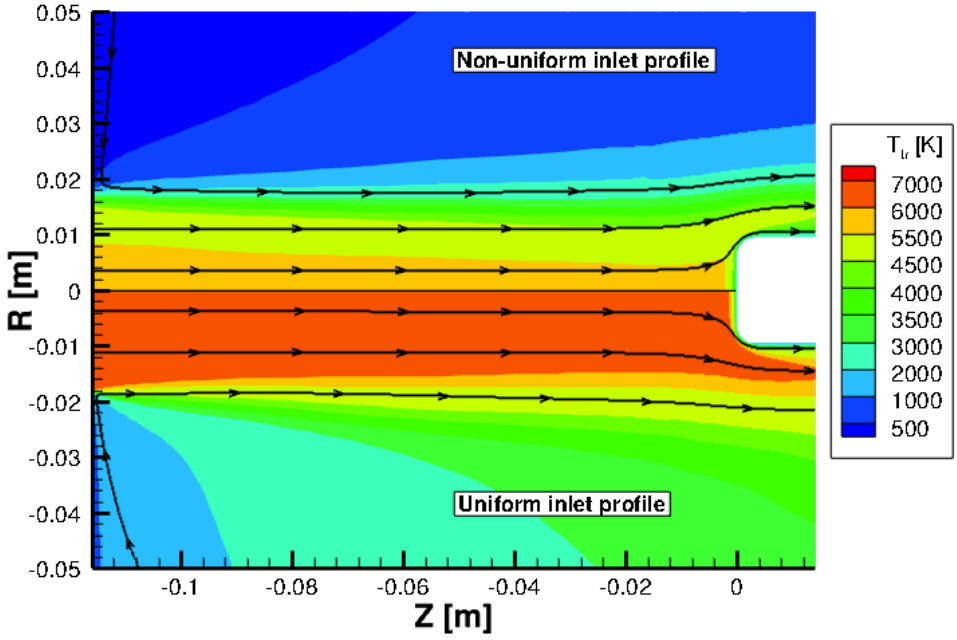

Figure 4.18: Comparison of translational temperature contours between simulation for non-uniform and uniform inlet profiles.

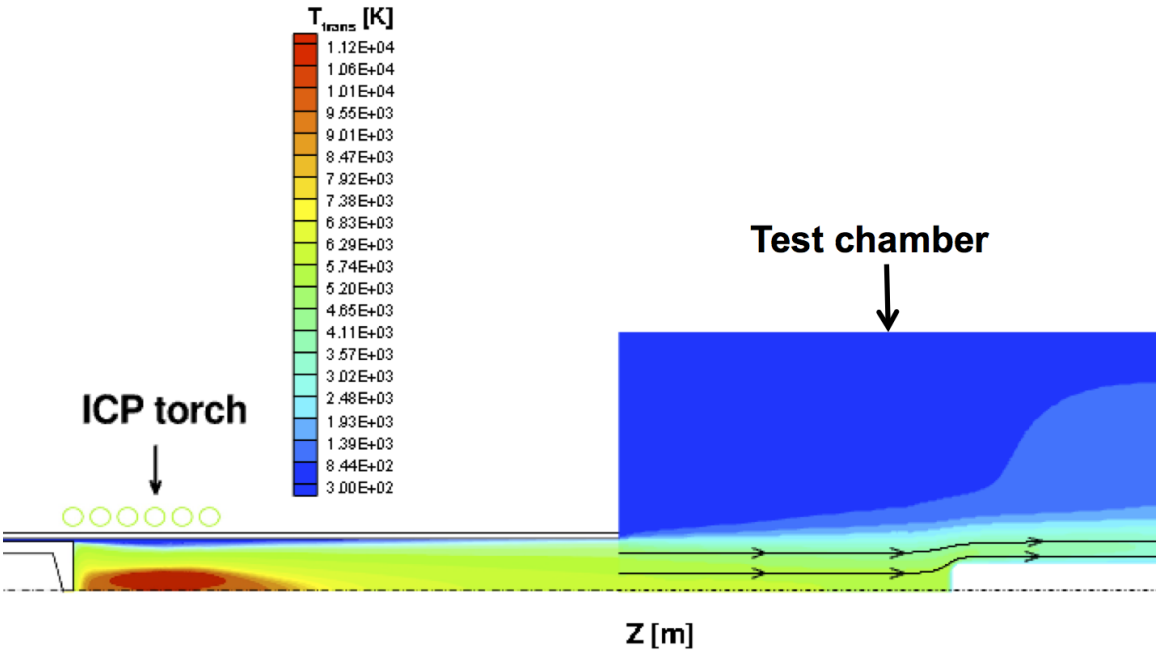

Figure 4.19: Translational temperature contours in the quartz confinement tube of the ICP torch obtained from the ICP torch simulations and in the test chamber of the facility obtained from facility simulations.

Figure 4.20 presents the results along the stagnation streamline in the boundary layer for translational temperature and normalized nitrogen atom number density in Figs. 4.20(a) and 4.20(b), respectively. Radial profiles for translational temperature and normalized nitrogen atom number density at a distance of 1.52 mm from the surface are shown in Figs. 4.21(a) and 4.21(b), respectively. The normalized nitrogen atom density is calculated by scaling the nitrogen atom number density value for each case with the respective value at the location of the measurement at the largest distance from the test sample.

It can be seen in Fig. 4.20(a) that the temperature profile for a uniform inlet shows better agreement with the experimental values as compared to the temperature profile for a non-uniform inlet. This occurs because the uniform inlet has a higher temperature of 7000 K as compared to the lower peak temperature of 6000 K for the non-uniform inlet that results in a higher temperature in the boundary layer for the uniform inlet profile. The temperature is related to the power absorbed from the ICP torch. Higher power absorbed from the torch may lead to a higher peak temperature that can provide better agreement with the temperature measurements [26]. Also, the high temperatures measured in the experiment could be a result of thermal nonequilibrium effects. The ICP torch simulation performed assumes thermal equilibrium. The radial temperature profile shown in Fig. 4.21(a) shows a similar trend with a higher temperature for the uniform inlet as compared to the non-uniform inlet, although the trend in the shape of the profile for the non-uniform inlet is in better agreement with the experimental values as compared to that of the uniform inlet. Figures 4.20(b) and 4.21(b) show that the normalized nitrogen atom density profile has a better agreement for the non-uniform inlet with the experimental measurements in comparison with that for the uniform inlet, both in the axial and radial directions. The relative heat flux shown in Fig. 4.22 shows that the total heat flux for the non-uniform inlet is lower than that of the uniform inlet. This is

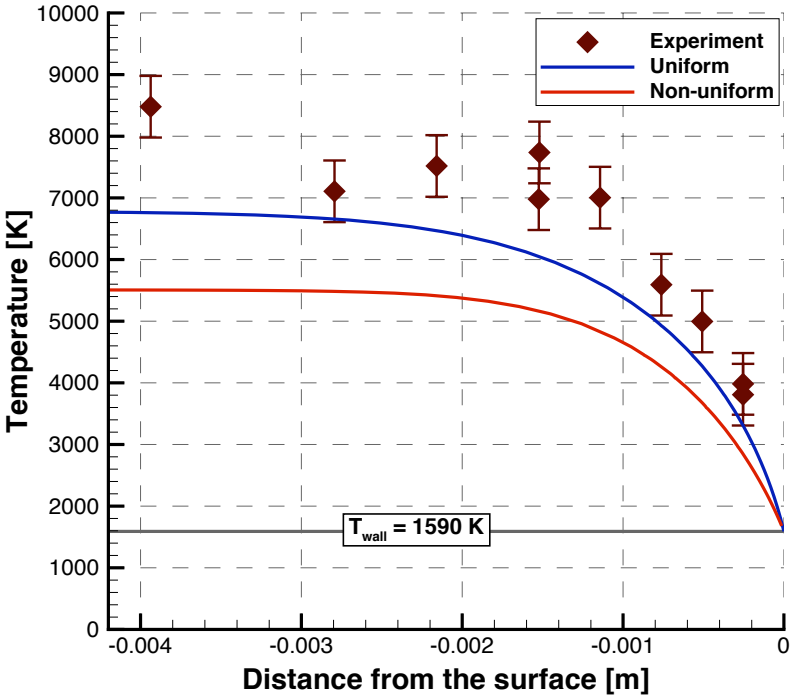

(a) Translational temperature

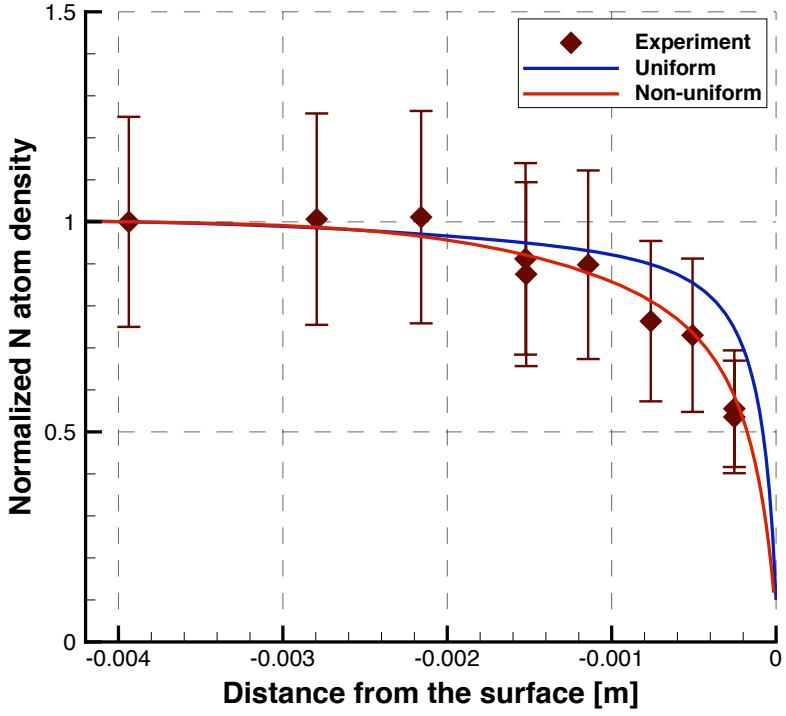

(b) Normalized N-atom density

Figure 4.20: Comparison of translational temperature and normalized N-atom density along the stagnation line between the computational results for uniform and non-uniform inlets and experimental data.

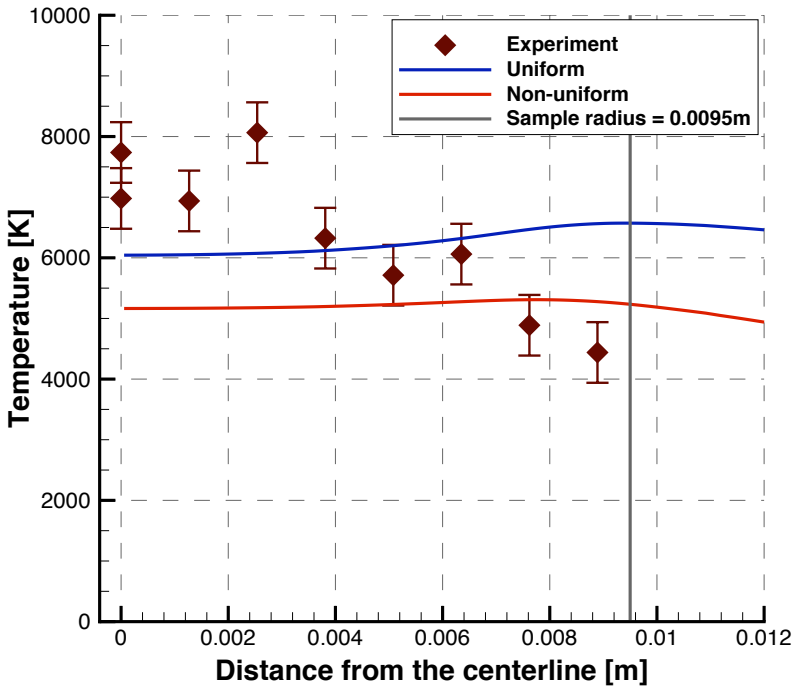

(a) Translational temperature

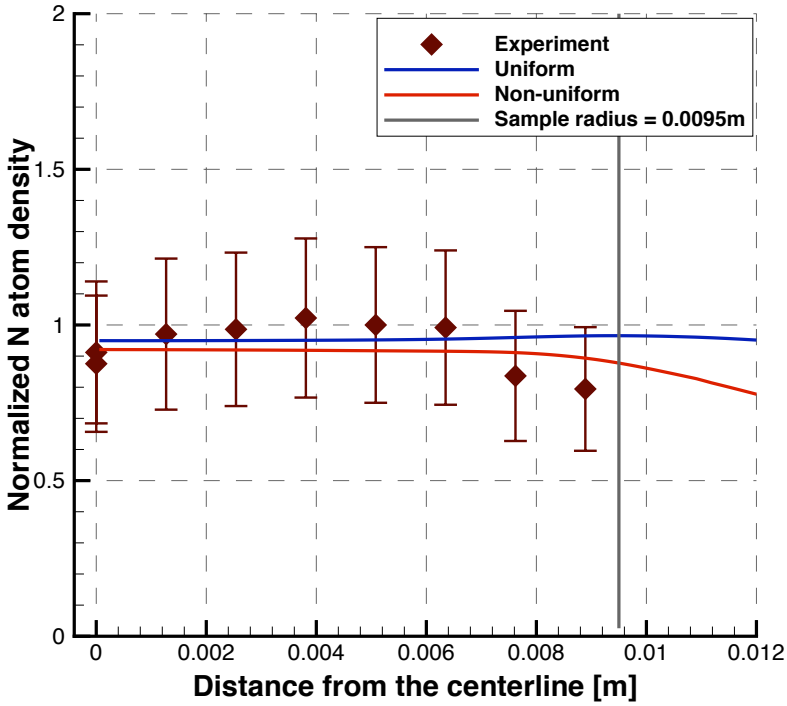

(b) Normalized N-atom density

Figure 4.21: Comparison of translational temperature and normalized N-atom density between the computational results for uniform and non-uniform inlets and experimental data in the radial direction at a distance of 1.52 mm from the stagnation point.

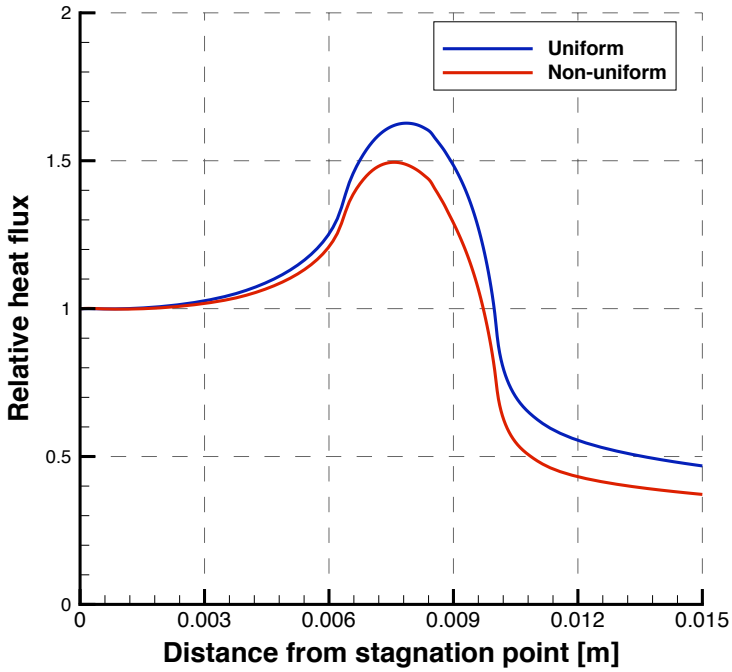

Figure 4.22: Relative heat flux

because of the lower enthalpy of the non-uniform inlet flow which results in the lower temperature of the flow. The relative heat flux is the ratio of the local heat flux to the stagnation point heat flux for each case. It is concluded that the profile trends in the results for the uniform inlet provide better agreement with the experimental measurements for translational temperature whereas the non-uniform inlet provides better agreement with the experimental measurements for normalized atom number density. It can be concluded from the results of this analysis that the non-uniform inlet does not significantly affect the solution and therefore, a uniform inlet profile is used for the rest of the computations in this thesis.

4.4 Summary

An analysis of the factors that could affect the simulation of fluid flow parameters and surface properties is presented. The results of a grid independence study are presented along with the description of the grids used for the simulations. A study is

performed to assess the effect of simulating a part of the test chamber as opposed to including its entire width in the simulation. The results of the comparison between the two configurations showed that excluding the side wall from the simulations does not affect the flow parameters and the surface properties for the graphite sample.

An investigation is performed to identify the nature of the flow in the test chamber for thermal equilibrium, thermal nonequilibrium and thermochemical nonequilibrium. The results show that the flow studied is in a state of weak thermochemical nonequilibrium. The effects of uniform and non-uniform inlet profiles on the flow around the graphite sample are also evaluated. The results of the comparison between the two show that the uniform profile provides better agreement with the experimental measurements of translational temperature whereas the non-uniform inlet profile provides better agreement with the experimental measurements of number density. It is also concluded that the non-uniform inlet profile does not significantly affect the solution.

CHAPTER V

Results

5.1 Introduction

Numerical simulations of the experimental configuration are performed using the CFD code LeMANS. This chapter presents the results obtained from the simulations. The main calculated parameters analyzed are translational temperature, normalized nitrogen atom density, surface heat flux, surface temperature and mass removal rate. The comparisons between the numerical results and experimental LIF measurements are presented for translational temperature and normalized nitrogen atom number density in the test sample boundary layer. The numerical simulation results for each configuration (described in Chapter III) are compared with the respective experimentally measured data. The results for Configuration 1 are presented in Section 5.2 followed by the results for Configuration 2 in Section 5.3. The ICP torch exit conditions are not well defined. Therefore, an analysis is performed for sensitivity of boundary layer flow parameters and surface properties to different chemical compositions at the torch exit. First, comparison is performed between the sensitivity to chemical composition based on chemical equilibrium and that calculated from power in the flow. There then follows an evaluation of the effect on flowfield parameters and surface properties to varying inlet temperature for constant input power and varying input power for constant inlet temperature. All the calculations are performed using

a radiative equilibrium boundary condition at the test article wall. This condition does not include the effects of conduction within the sample. Therefore, the effects of conduction within the sample wall are included in the calculations and compared with the results from the radiative equilibrium condition. The results of the comparative analysis are presented in this chapter. Finally, a summary of the major conclusions drawn from this study are presented.

5.2 Results for configuration 1

The comparisons of computational results with the measured experimental data for configuration 1 are presented here. The test cases considered to determine the effects of gas-surface interaction processes using the finite rate surface chemistry model are shown in Table 5.1. The description of these test cases is presented in Section 3.4. The boundary conditions used for the simulation are shown in Fig. 4.7. The test article wall is set to a radiative equilibrium boundary condition defined by Eq. 2.32. The test chamber wall is set as an isothermal wall with a wall temperature of 300 K.

Table 5.1: Test cases.

Case	Catalytic efficiency γ_N	Carbon nitridation efficiency γ_{CN}
Case 1	0	0
Case 2	0.07	0
Case 3	0.07	0.005
Case 4	1	0

The main calculated parameters analyzed are translational temperature, normalized nitrogen atom density and surface heat flux. The comparisons between the numerical results and experimental LIF measurements are presented for translational temperature and normalized nitrogen atom density in the test sample boundary layer along the stagnation streamline and in the radial direction at an axial distance of 1.52 mm from the test article surface. The boundary layer is the layer of fluid in

the immediate vicinity of a surface where the effects of viscosity are significant. The thickness of this layer is defined as the point where the velocity is 99% of the free stream velocity [104]. The normalized nitrogen atom density is calculated by scaling the nitrogen atom density value for each case with the respective value at the location of the measurement at the largest distance from the test sample. The stagnation line profiles for translational temperature and normalized nitrogen atom number density in the boundary layer are shown in Figs. 5.1 and 5.2, respectively. The radial profiles for translational temperature and normalized nitrogen atom number density are shown in Figs. 5.3(a) and 5.4(a), respectively. The region where the radial measurements are taken is shown in the temperature and normalized nitrogen atom density contours for Case 4 in Figs. 5.3(b) and 5.4(b), respectively. The experimental temperature and normalized nitrogen atom density values have uncertainties of about $\pm$ 500 K and $\pm$ 25%, respectively [52]. The simulation run time for each case is approximately 6 hours using 32 processors.

It can be seen in Figs. 5.1 and 5.3(a) that the temperature in the boundary layer rises both axially and radially for cases where surface chemistry is included as compared to Case 1 for a non-catalytic wall. The comparisons between Cases 2, 3 and 4 show that the temperature in the boundary layer is not significantly altered for different surface chemistry models. The computed values for temperature in the boundary layer are lower than the experimentally measured values. It can be seen that there is no trend in the experimentally measured values. The measurement location at a distance of 1.52 mm from the test article surface has two data points. One point is from the radial scan and the other is from the axial scan. The temperature at this location lies within the range from approximately 6500 K to 8200 K. This suggests that the uncertainty in the measured values is higher than the estimated value of $\pm$ 500 K.

The effect of gas-surface interactions on nitrogen atom density in the boundary

layer can be seen in Figs. 5.2 and 5.4(a), respectively. It can be seen in Fig. 5.2 that nitrogen atom density increases in the boundary layer for Case 1 whereas it is depleted for all other cases. The nitrogen atom loss is due to surface catalysis i.e. catalytic recombination of nitrogen atoms to molecules for Cases 2 and 4. As expected, the nitrogen atom density for a partially catalytic surface, i.e. for $\gamma = 0.07$, lies between the profiles for non-catalytic and fully catalytic walls. The nitrogen atom loss seen for Case 3 is both due to surface catalysis as well as carbon nitridation. The nitrogen atom removal for Case 3, i.e. for $\gamma_N = 0.07$ and $\gamma_{CN} = 0.005$, is largely due to surface catalysis with negligible carbon nitridation. The nitrogen atom density for all cases except Case 1 shows good agreement with the experimental measurements.

The total heat flux for these simulations is shown in Fig. 5.5(a) along with the diffusive heat flux in Fig. 5.5(b). The total heat flux is the summation of the translational convective heat flux, vibrational convective heat flux and diffusive heat flux. As expected, there is an increase in the total heat flux for all the cases with surface reactions as compared to the non-catalytic wall. The heat flux transferred to the surface is increased approximately by a factor of 4 when the surface is fully-catalytic as opposed to a non-catalytic surface. This increase is explained by the contribution from diffusive heat flux for the cases with surface reactions which is zero for a non-catalytic wall as shown in Fig. 5.5(b).

5.2.1 Comparison between the surface chemistry models

A comparison is performed between the simple binary catalytic recombination (BCR) model (described in Section 2.4.3) and the complex finite rate surface chemistry (FRSC) model (described in Section 2.4.4). The simulations for the two models are performed for configuration 1 with the test article surface catalytic efficiency γ_N of 0.07. The test article and chamber walls are set as isothermal with a wall temperature of 1591 K and 300 K, respectively. Species diffusion coefficient D_k is used in the

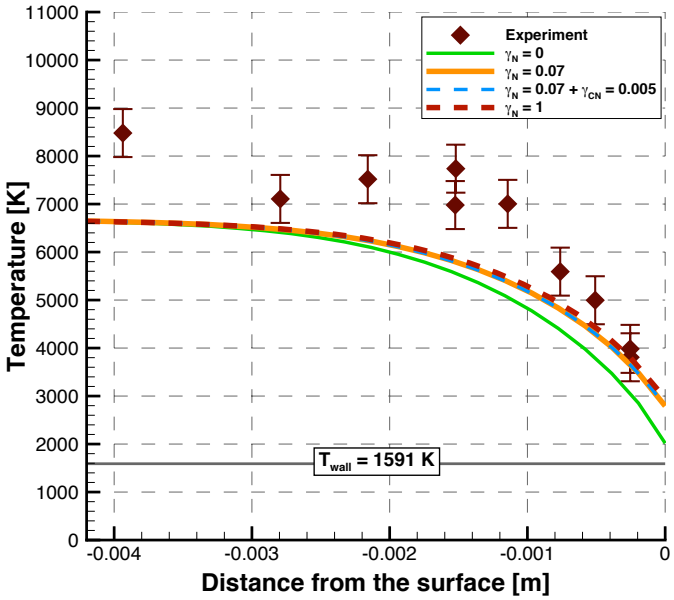

Figure 5.1: Comparison of translational temperature along the stagnation line for Configuration 1 for different test conditions listed in Table 5.1.

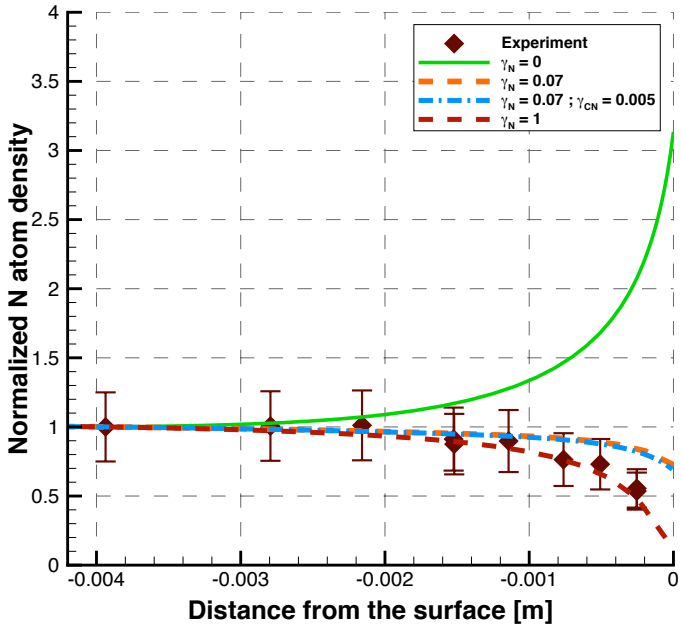

Figure 5.2: Comparison of normalized N-atom density along the stagnation line for Configuration 1 for different test conditions listed in Table 5.1.

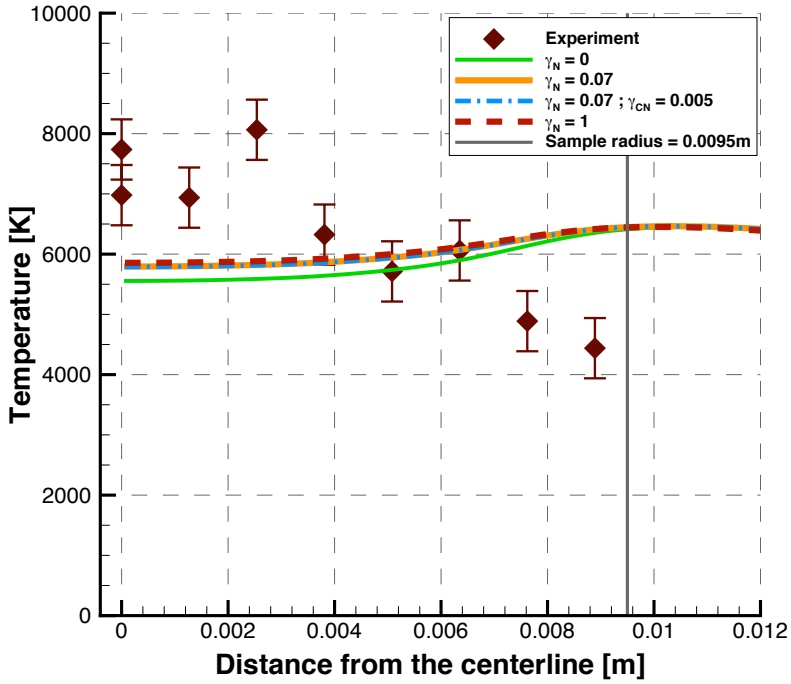

(a) Translational temperature

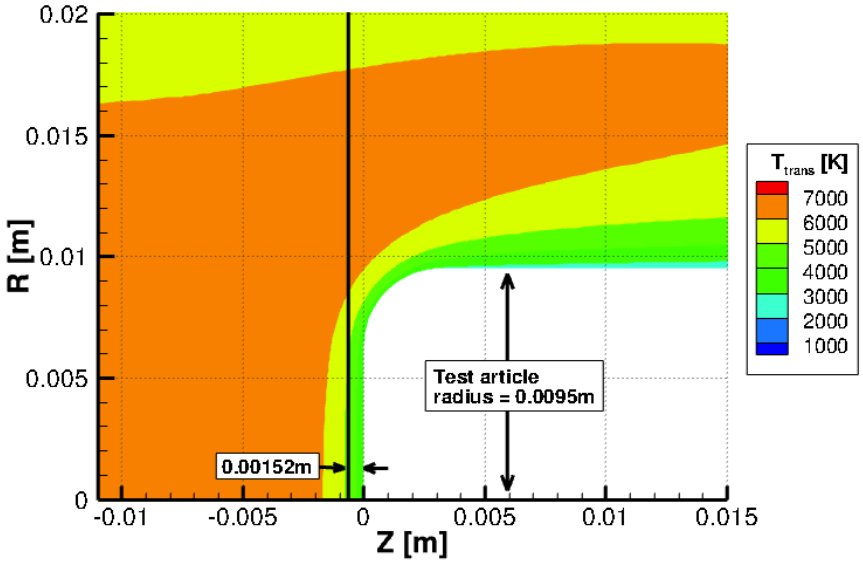

(b) Translational temperature contours

Figure 5.3: (a) Comparison of translational temperature between the computational and experimental data in the radial direction at a distance of 1.52 mm from the surface. (b) Translational temperature contours for Case 4 (γ_N=1) showing the region of radial measurement.

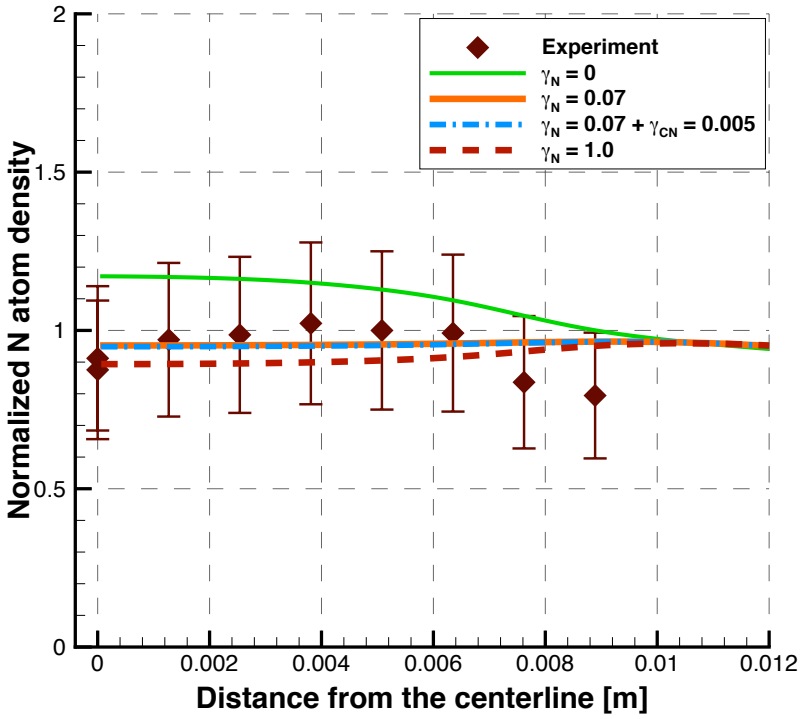

(a) Normalized N-atom density

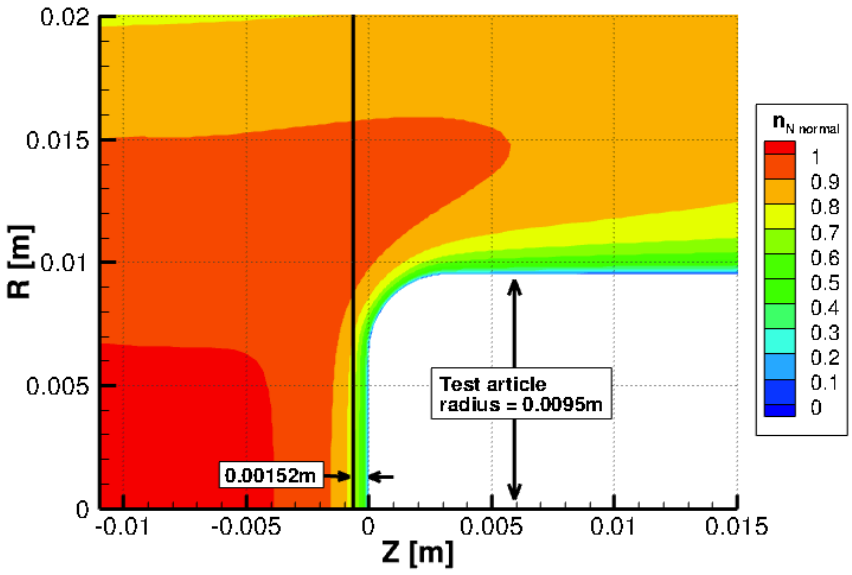

(b) Normalized N-atom density contours

Figure 5.4: (a) Comparison of normalized N-atom density between the computational and experimental data in the radial direction at a distance of 1.52 mm from the surface. (b) Normalized N-atom density contours for Case 4 (γ_N=1) showing the region of radial measurement.

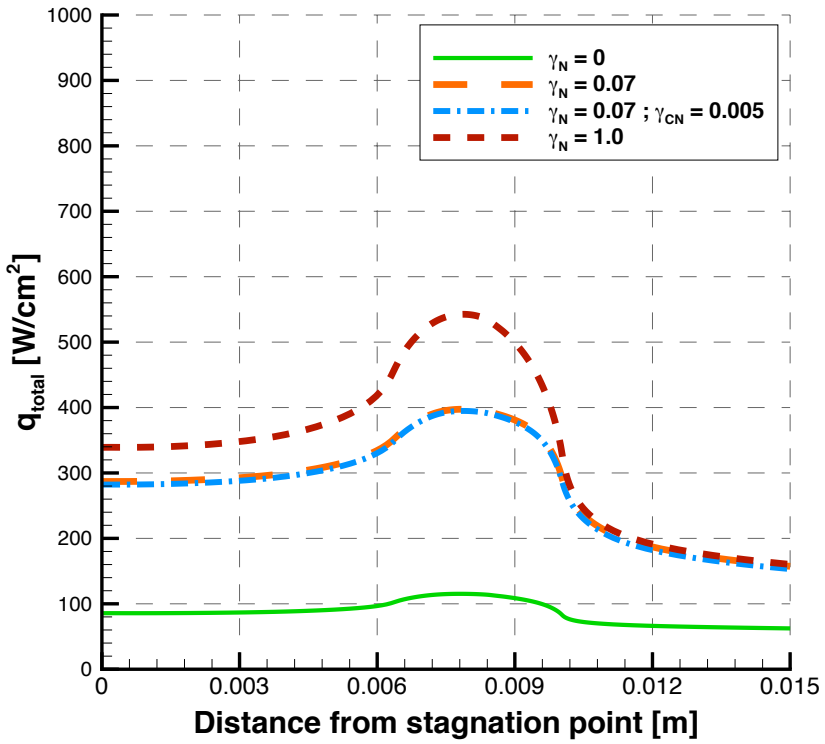

(a) Total heat flux

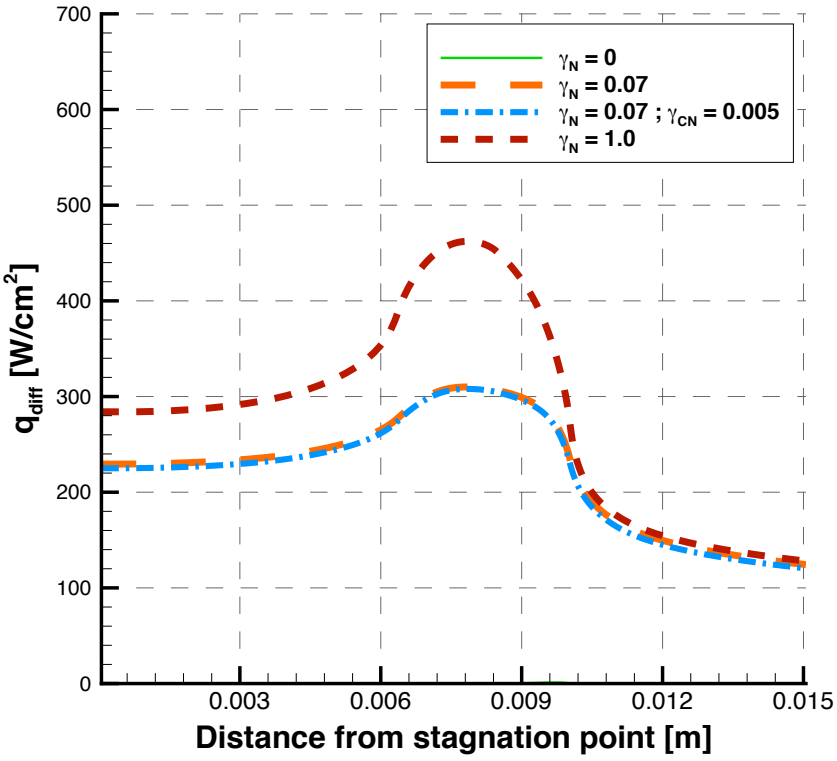

(b) Diffusive heat flux

Figure 5.5: Comparison of wall heat flux between the computational results for different test conditions listed in Table 5.1.

calculation for both models. The comparison between the translational temperature and the normalized nitrogen atom number density in the stagnation line boundary layer is shown in Figs. 5.6(a) and 5.6(b), respectively. It can be seen that both the models produce the same results. It can be concluded from these results that the BCR model can be successfully used to quantify the effects of surface catalysis in an investigation involving a binary gaseous mixture consisting of one atomic and one molecular species. It can be used as a baseline model in the preliminary investigation of surface catalycity effects for different species on different materials before a rigorous investigation involving surface chemical reactions that requires the use of the FRSC model.

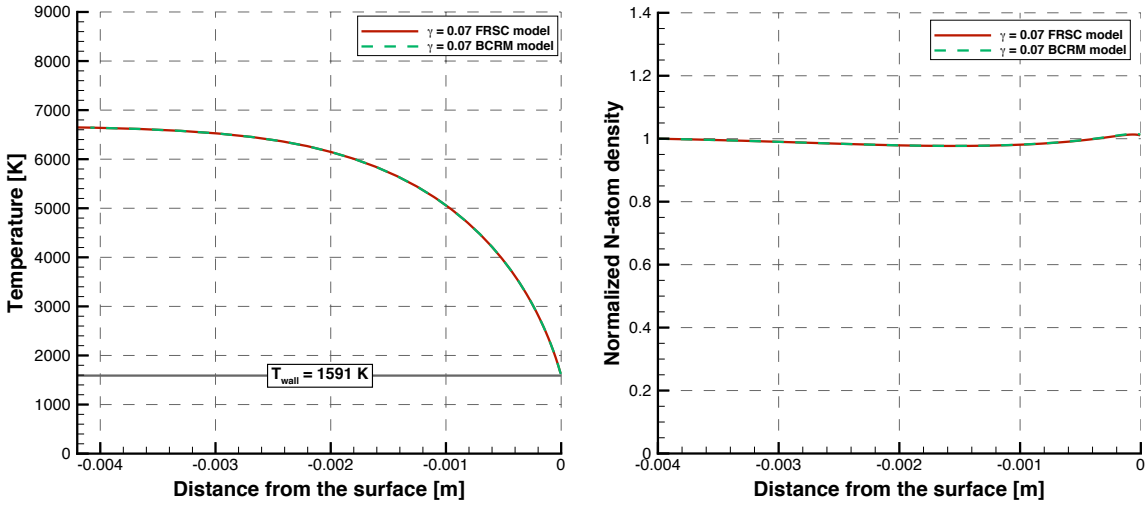

(a) Translational temperature

(b) Normalized N-atom density

Figure 5.6: Comparison of translational temperature and normalized N-atom density along the stagnation line for the two surface chemistry models

5.3 Results for configuration 2

The comparisons of computational results with the measured experimental data for configuration 2 are presented here. The test cases considered to determine the effects of gas-surface interaction processes are shown in Table 5.1. The boundary

conditions set for the simulation are shown in Fig. 4.7. The test article wall is set to a radiative equilibrium boundary condition and the test chamber wall is set as an isothermal wall with a temperature of 300 K. The simulation run time for each case is approximately 6 hours using 32 processors.

The comparisons between the numerical results and experimental LIF measurements are presented for translational temperature and normalized nitrogen atom density in the test sample boundary layer along the stagnation streamline. The flow property measurements were taken only along the stagnation line in the boundary layer for this configuration. The stagnation line boundary layer results are shown for the translational temperature in Fig. 5.7 and the normalized nitrogen atom density in Fig. 5.8.

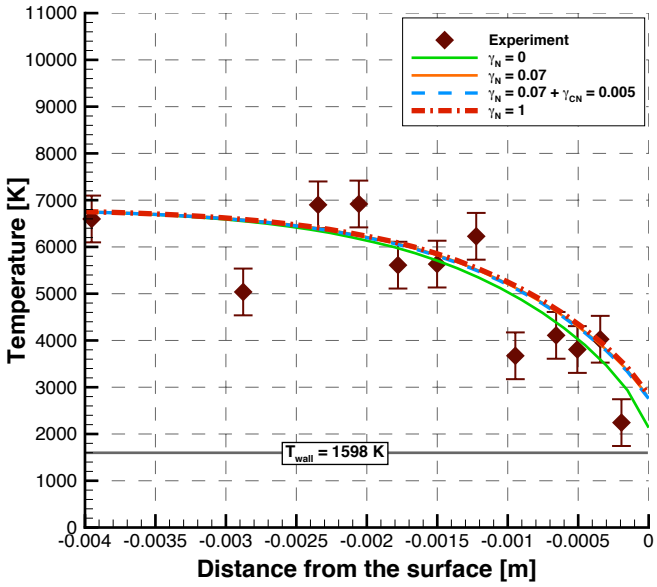

Figure 5.7: Comparison of translational temperature along the stagnation line for Configuration 2.

Similar to the results for configuration 1, there is a rise in temperature (Fig. 5.7) in the boundary layer for cases where surface chemistry is included as compared to Case 1 a for non-catalytic wall. The comparisons between Cases 2, 3 and 4 show that temperature in the boundary layer is not significantly affected for different surface

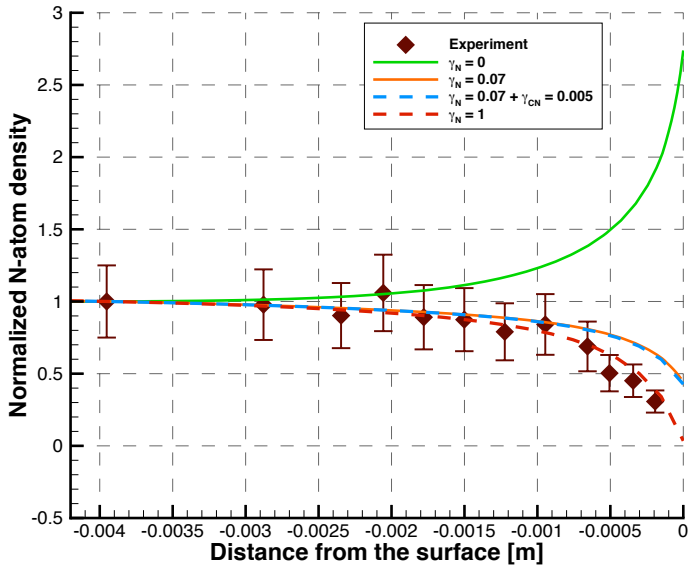

Figure 5.8: Comparison of normalized N-atom density along the stagnation line for Configuration 2.

chemistry models. There is an increase in nitrogen atom density (5.8) in the boundary layer for Case 1 whereas it is consumed for all other cases due to surface chemical reactions. The nitrogen atom loss is again due to surface catalysis, i.e., catalytic recombination of nitrogen atoms to molecules for Cases 2 and 4. The nitrogen atom loss seen for Case 3 is the combined effect of surface catalysis as well as carbon nitridation. The nitrogen atom density for all cases except Case 1 show good agreement with the experimental measurements.

The effect of surface chemistry on the surface properties is also evaluated. The properties analyzed are the surface heat flux and wall temperature. The total heat flux is plotted in Fig. 5.9(a) along with the diffusive heat flux in Fig. 5.9(b).

An increase is seen in the total heat flux for all the cases with surface reactions as compared to the non-catalytic wall. This increase is explained by the contribution from diffusive heat flux for the cases with surface reactions which is zero for a non-catalytic wall. The wall temperature for results from different surface chemistry models is shown in Fig. 5.10. Case 4 with a fully catalytic wall has the highest and

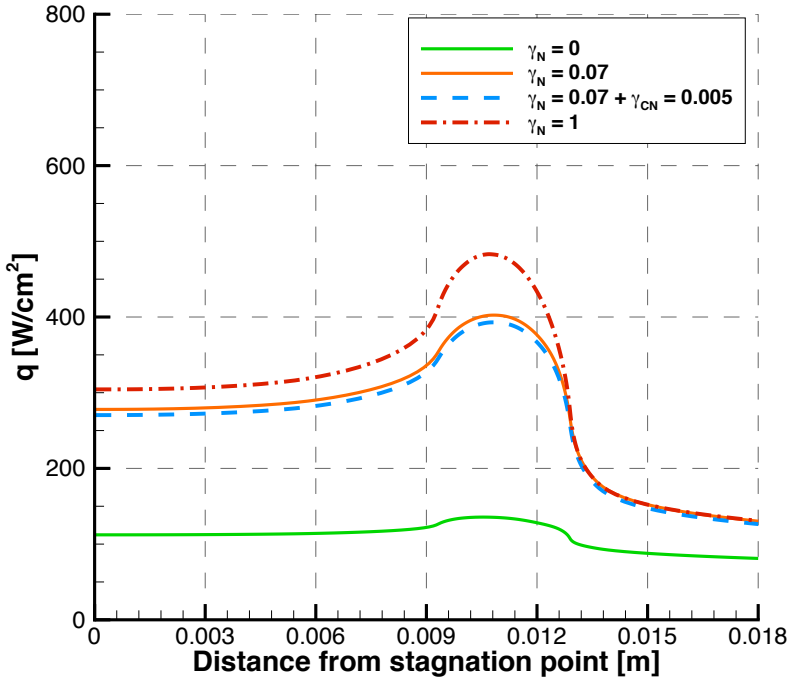

(a) Total heat flux

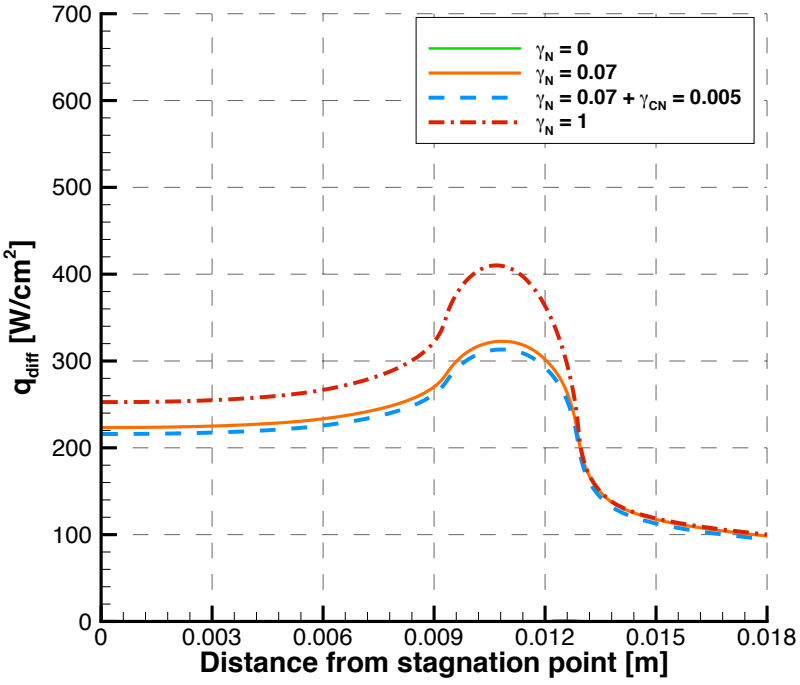

(b) Diffusive heat flux

Figure 5.9: Comparison of wall heat flux between the computational results for configuration 2.

Case 1 with no surface chemistry has the lowest temperature at the surface. The temperature for Cases 2 and 3 lie between those for non-catalytic and fully catalytic walls.

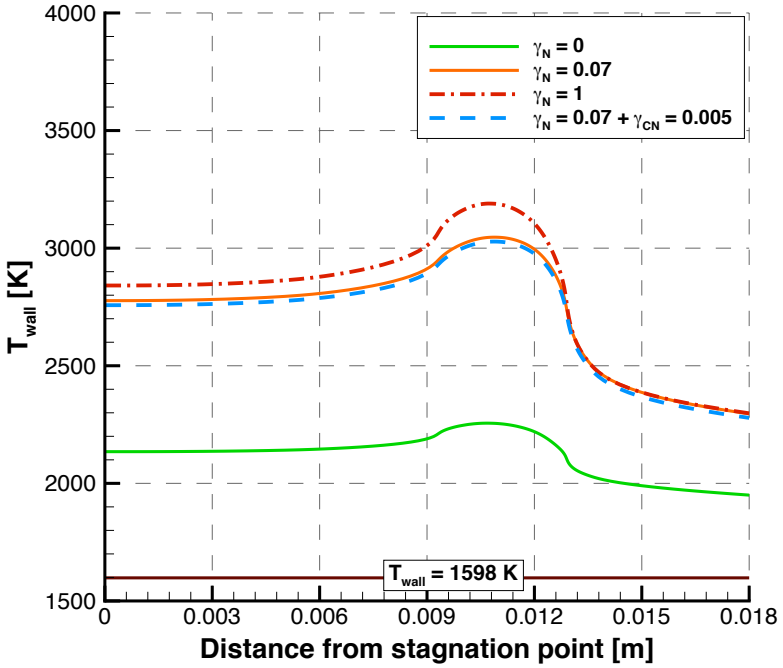

Figure 5.10: Comparison of wall temperature between the computational results for configuration 2.

The carbon mass removal flux ($\dot{m}_b$) as a result of the carbon nitridation reaction for Case 3 is also computed and is shown in Fig. 5.11. The total mass loss rate is calculated from $\dot{m}_b$ as shown in Eq. 5.1.

$$\text{mass loss rate} = \int \dot{m}_b dA \tag{5.1}$$

where $\dot{m}_b$ is the mass removal flux (calculated using Eq. 2.30) for each surface element and dA is the surface area of each element. The stagnation point heat flux is measured experimentally using a slug calorimeter (described in Section 2.2.2.1) for test conditions similar to this case. The heat flux is measured for the case of 0.84 g/s

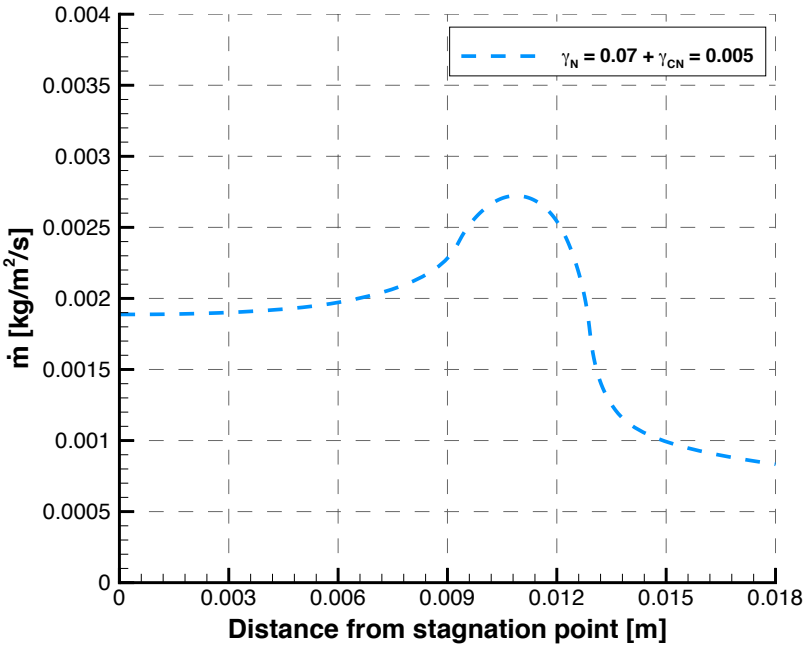

Figure 5.11: Mass removal flux due to carbon nitridation.

mass flow rate and pressure of 21.3 kPa. A comparison between the experimental and computed values for stagnation point heat flux, temperature and mass loss rate for Case 3 is provided in Table 5.2. The stagnation point is the point on the surface where the flow velocity is zero. It is shown in Fig. 4.7.

Table 5.2: The stagnation point values and the mass loss rate.

	$q_{stag}[W/cm^2]$	$T_{stag}[K]$	mass loss rate $[mg/s]$
CEA	270	2757	2.2
Experiment	40 - 80	∼1600	0.2 - 0.6

It can be seen that the computational values are much higher than the experimentally measured values. These higher computed values could be explained by a combined effect of various mechanisms. It could be attributed to a higher degree of nitrogen atom flux to the surface in the calculations. An assumption of chemical equilibrium of the nitrogen gas mixture at the exit of the quartz tube is used in these simulations. The equilibrium gas mixture composition is probably more dissociated than the composition for a chemically reacting flow with finite rate chemistry. There-

fore, the flux to the test sample of dissociated nitrogen atoms available might be less than used in these simulations. The higher mass loss rate computed from the CEA results as compared with the experimental value could be the result of high number of nitrogen atoms reaching the test sample surface and combining with the surface carbon to form gaseous CN. A lower nitrogen atom flux to the surface would result in a lower mass removal rate.

There is a possibility of CN to react further with nitrogen atoms to form nitrogen molecules and increase the consumption of nitrogen atoms in the boundary layer. The species number densities along the stagnation line in the boundary layer for Case 3 are shown in Fig. 5.12. It can be seen that the CN molecule concentration in the boundary layer increases and the nitrogen molecule concentration decreases as they approach the surface. The number density of CN is approximately three orders of magnitude less than that of nitrogen atom concentration. Therefore, the reaction of CN with nitrogen atoms will not significantly affect the loss of nitrogen atoms in the boundary layer.

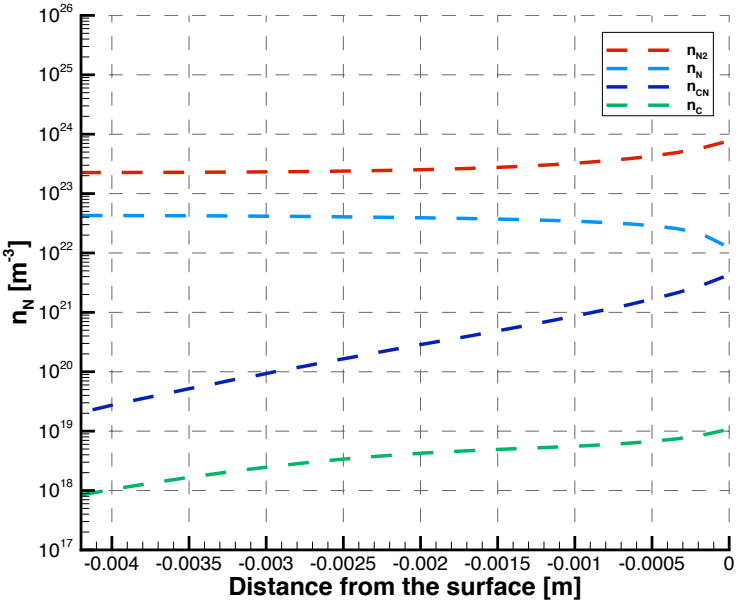

Figure 5.12: Species number density along the stagnation line for Case 3.

A sensitivity analysis is performed on the ICP torch exit chemical composition

to evaluate its effects on the flow parameters in the boundary layer and the surface properties. The results of this analysis are presented in Section 5.3.1. The higher simulated mass removal rate suggests that the carbon nitridation efficiency should perhaps be smaller. Therefore, the effects of a varying carbon nitridation efficiency are analyzed. The computed values of heat flux, wall temperature and mass loss rate could also be affected by the net heat transfer to the surface. A radiative equilibrium boundary condition is used in these simulations where the heat conduction within the sample is not included, which if accounted for, may affect the surface properties. Therefore, a study is performed to determine the effects of conduction within the sample on the surface properties and its results are presented in Section 5.3.3.

5.3.1 Sensitivity to inlet chemical composition

5.3.1.1 Comparison between CEA and Power = 13.8 kW

The power absorbed by the flow in the ICP torch is used to determine the composition of the gas at the test chamber inlet, i.e., the ICP torch exit. The power in the flow is the product of the voltage, current, and an efficiency factor estimated to be 0.56 [72]. For configuration 2, the power supply is 13.8 kW calculated from 10.3 kV voltage and 2.4 A current. The flow power is also given by the product of the mass flow rate $\dot{m}_{flow}$ and specific enthalpy h given by Eq. 5.2. The specific enthalpy is dependent on the composition of the mixture given by mass fraction of the gas

mixture species Y_i and the inlet temperature of the flow T.

$$Power = \dot{m}_{flow}\Delta h \tag{5.2}$$

$$\Delta h = \sum_{i=N,N_2} Y_i \int_{298}^{T} C_{pi}\, dT + \sum_{i=N,N_2} Y_i \Delta \overset{\circ}{h}_{fi}$$

where,

$$Y_i = \frac{M_i}{M_{avg}} X_i \; ; \; M_{avg} = \sum_{i=N,N_2} X_i M_i$$

$$C_{pi} = C_{vi} - R_i$$

$$C_{vi} = C_{vi,t} + C_{vi,r} + C_{vi,vib} + C_{vi,el}$$

$$C_{vi,t} = 1.5R_i$$

For i = N_2,

$$C_{vi,r} = R_i$$

$$C_{vi,vib} = R_i \frac{(\theta_{vib,i}/T_{vib,i})^2 exp(\theta_{vib,i}/T_{vib})}{[exp(\theta_{vib,i}/T_{vib}) - 1]^2}$$

For i = N,

$$C_{vi,r} = 0$$

$$C_{vi,vib} = 0$$

For i = N,N_2

$$C_{vi,el} = R_i \{ \frac{\sum_{j=1}^{\infty} g_{j,i}(\theta_{el,j,i}/T_{el})^2 exp(-\theta_{el,j,i}/T_{el})}{\sum_{j=0}^{\infty} g_{j,i} exp(-\theta_{el,j,i}/T_{el})}$$
$$- \frac{[\sum_{j=1}^{\infty} g_{j,i}\theta_{el,j,i} exp(-\theta_{el,j,i}/T_{el})][\sum_{j=0}^{\infty} g_{j,i}(\theta_{el,j,i}/T_{el}^2) exp(-\theta_{el,j,i}/T_{el})]}{[\sum_{j=0}^{\infty} g_{j,i} exp(-\theta_{el,j,i}/T_{el})]^2} \}$$

where X_i is the species mole fraction, M_i and M_{avg} are the individual species and average gas mixture molecular weight, respectively. C_{pi} is species specific heat at constant pressure, R_i is the species gas constant and $\overset{\circ}{h}_{fi}$ is the species heat of formation. C_{vi} is species specific heat at constant volume. The subscripts $C_{vi,t}$, $C_{vi,r}$, $C_{vi,vib}$ and

$C_{vi,el}$ represent the translational, rotational, vibrational and electronic specific heats at constant volume respectively. $\theta_{vib,i}$ is the species characteristic vibrational temperature. $\theta_{el,j,i}$ and $g_{j,i}$ are the characteristic electronic temperature and the degeneracy of the j-th energy level, respectively [81].

The composition of the gas mixture is calculated for 13.8 kW power using the mass flow rate and inlet temperature for configuration 2 given in Table 3.1. This section presents the comparison performed between the results obtained using the inlet gas composition calculated assuming chemical equilibrium and that obtained for a flow power of 13.8 kW. The chemical equilibrium composition is calculated using CEA and is referred to as "chemical equilibrium" in the legend. The power in the flow for chemical equilibrium composition at inlet and 7000 K inlet temperature corresponds to 30 kW which is 100% higher than the calculated power. The comparison is performed for Case 3 to include the effects of the inlet gas composition on carbon mass removal.

The relation of power with gas mixture composition is shown in Fig. 5.13 where power is plotted against nitrogen atom mole fraction X_N for constant temperature of 7000 K (calculated using Eq. 5.2) along with the constant power of 30 kW in the flow for chemical equilibrium composition at the inlet. It can be seen that the power in the flow is minimum for zero nitrogen atom mole fraction i.e. the flow is not dissociated. The flow power increases with the level of dissociation in the flow and is maximum for fully dissociated flow ($X_N = 1$). The higher the dissociation, the higher the power.

Based on the chemical equilibrium and 13.8 kW inlet compositions, the translational temperature and normalized nitrogen atom number density profiles along the stagnation line in the boundary layer are shown in Figs. 5.14 and 5.15, respectively. The translational temperature in the boundary layer for 13.8 kW power is lower in comparison to the equilibrium inlet composition. The reason for this is that the temperature in the flow decreases with decrease in enthalpy. Enthalpy is directly related

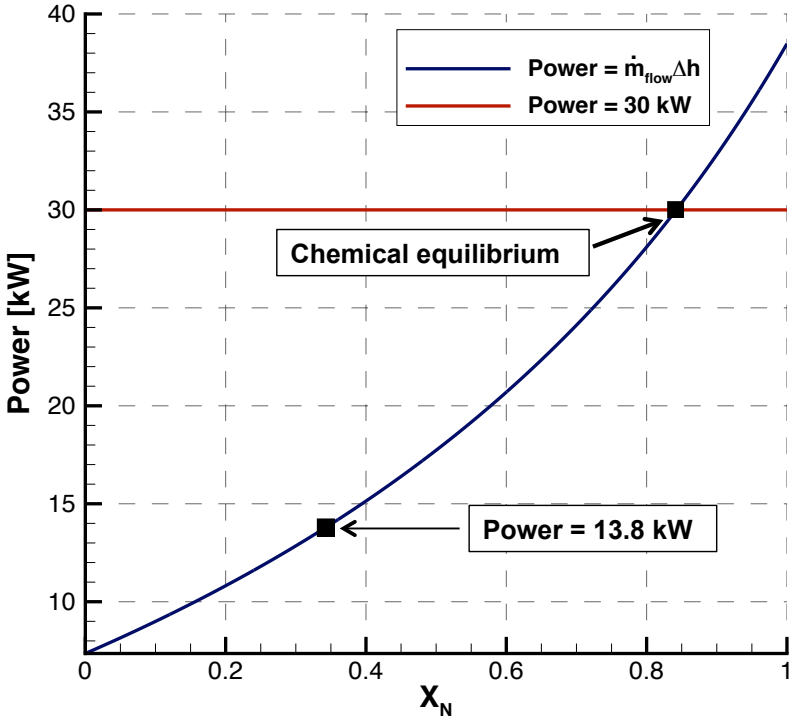

Figure 5.13: Plot of power against nitrogen atom mole fraction.

to power (Eq. 5.2). The root mean square percentage error between the translational temperature for chemical equilibrium inlet composition and the experimental values is 16.1%. The root mean square percentage error between the translational temperature for 13.8 kW power and the experimental values is 16.3%.

The inlet composition calculated using 13.8 kW power shows a better agreement with experimental data for normalized nitrogen atom number density in comparison to the equilibrium inlet composition. The level of dissociation is higher for chemical equilibrium inlet composition as compared to 13.8 kW power inlet composition. Therefore, the nitrogen atom density is higher for the chemical equilibrium case as compared to the 13.8 kW power case.

The total heat flux and temperature at the wall for these cases are shown in Figs. 5.16 and 5.17, respectively. The mass removal flux is shown in Fig. 5.18.

As can be seen, there is a significant reduction in heat flux, the wall temperature and mass loss for 13.8 kW power in comparison to the equilibrium inlet composition.

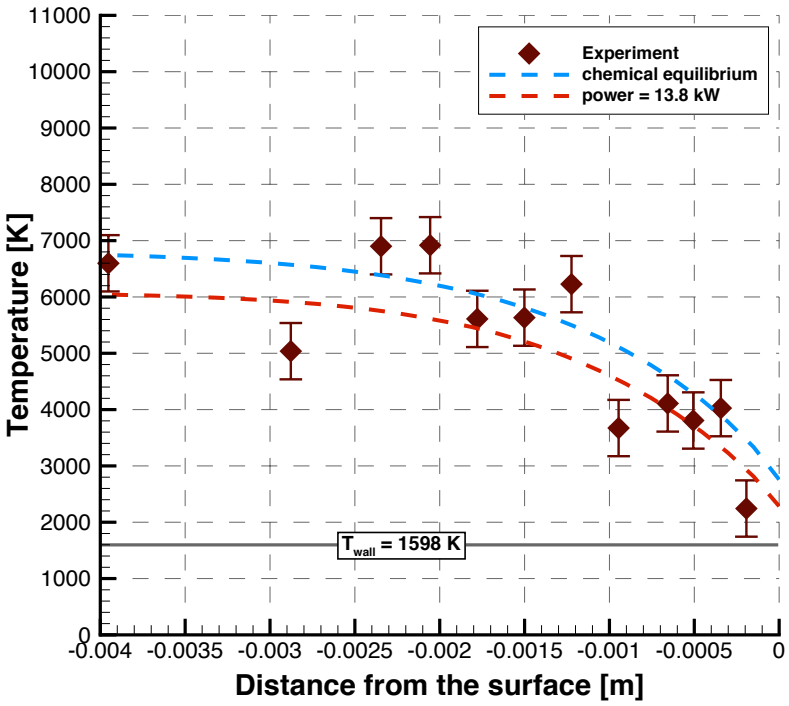

Figure 5.14: Comparison of translational temperature along the stagnation line for different inlet compositions.

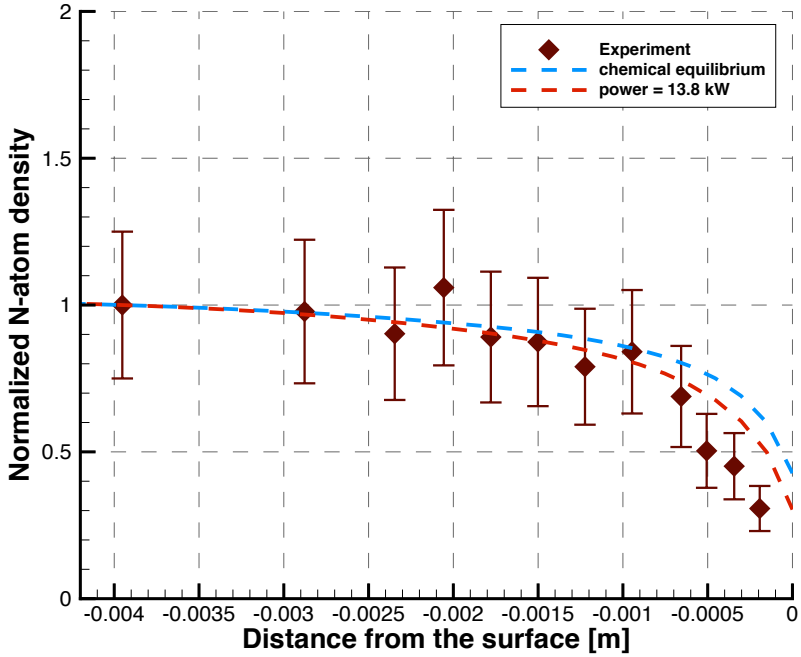

Figure 5.15: Comparison of normalized N-atom density along the stagnation line for different inlet compositions.

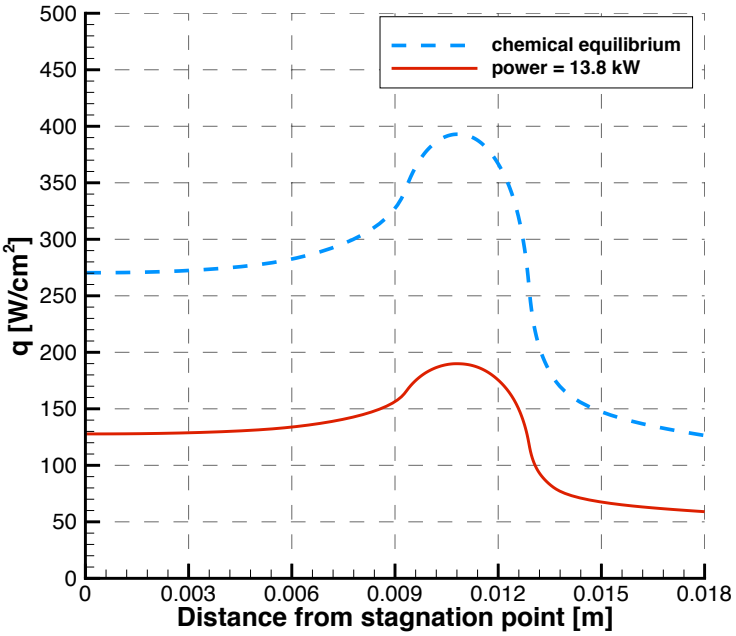

Figure 5.16: Comparison of wall heat flux between the computational results for different inlet compositions.

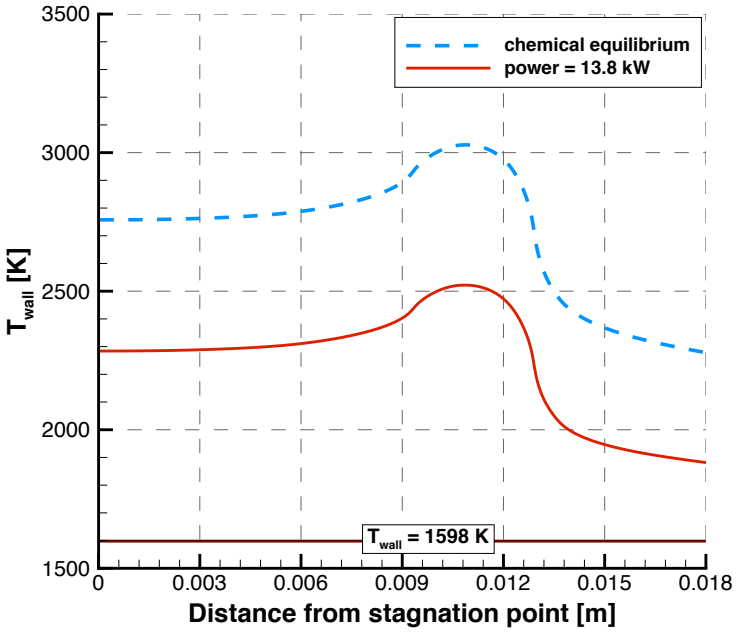

Figure 5.17: Comparison of wall temperature between the computational results for different inlet compositions.

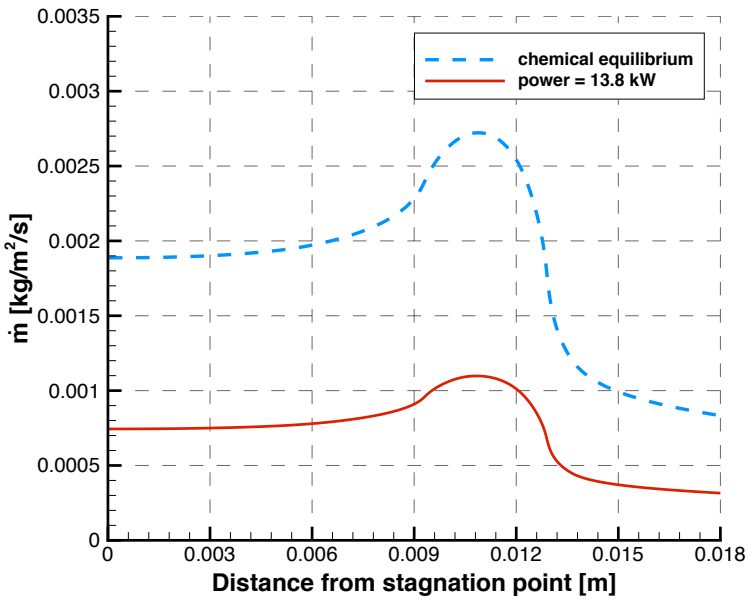

Figure 5.18: Comparison of mass removal flux between chemical composition for equilibrium inlet and 13.8 kW power.

The comparison between the stagnation point values for the two cases along with the experimental data is shown in Table 5.3. There is a 52% reduction in heat flux, 17% reduction in wall temperature, and 60% reduction in mass loss rate for the assumption of 13.8 kW flow power in comparison with the use of equilibrium chemical composition at the inlet. These values are still higher than the experimentally measured data. The losses in the ICP torch are not quantified experimentally and hence are not included in the calculation of power. The comparisons suggest that the power in the flow maybe even less than 13.8 kW. Since the ICP torch exit conditions are not well defined, a sensitivity analysis on the ICP torch exit chemical composition is performed for different values of inlet power and temperature. The results of the analysis for sensitivity to inlet temperature are presented in Section 5.3.1.2 and for inlet power, the results are presented in Section 5.3.1.3.

Table 5.3: The stagnation point values and the mass loss rate.

inlet	T_{inf} [K]	$q_{stag}[W/cm^2]$	$T_{stag}[K]$	mass loss $[mg/s]$
CEA	7000	270	2757	2.2
13.8 kW	7000	128	2284	0.86
Experiment	7000	40 - 80	1600	0.2 - 0.6

5.3.1.2 Sensitivity to Inlet Temperature

The results of the analysis for sensitivity of the flow field and surface parameters to varying inlet temperature for constant input power are presented in this section. Three values of inlet temperature, i.e., 6000 K, 7000 K, and 8000 K, are considered. The chemical composition at the inlet is calculated for 13.8 kW power, mass flow rate for configuration 2, and the respective temperature for each case using Eq. 5.2. All the simulations are performed for Case 3 surface chemistry. The translational temperature and normalized nitrogen atom number density are shown in Figs. 5.19 and 5.20, respectively.

It can be seen that there is negligible effect of varying inlet temperature on the profiles of translational temperature and the nitrogen atom density. The difference between each respective profile both for translational temperature and the nitrogen atom density is less than 1%. This negligible effect is best explained by the profiles for translational temperature and nitrogen atom number density along the entire stagnation line shown in Figs. 5.21 and 5.22, respectively. For the 8000 K case, as the flow progresses towards the sample, the temperature starts decreasing and the nitrogen atom density starts increasing. This is because the flow is chemically reacting and for higher temperature there will be more dissociation. The case for 7000 K inlet temperature shows a similar trend. For the 6000 K case, there is an increase in the temperature and a decrease in nitrogen atom number density along the stagnation line. The reason for this is again the chemically reacting flow and for lower temperature the flow is less dissociated. All three cases tend to reach a similar

mixture composition and temperature as the enthalpy of the flow is constant due to constant power in the flow.

One interesting aspect of the inlet flow composition for these cases is the counter-intuitive inlet composition. The mole fraction in the gas mixture is a maximum for inlet temperature of 6000 K and minimum for 8000 K. For a higher temperature, the flow is more dissociated as opposed to when it is at lower temperature. The mole fraction of nitrogen atoms at the inlet for the simulation cases of 6000 K, 7000 K, and 8000 K is 0.40, 0.34, and 0.28, respectively. The explanation for this trend is the constant inlet power. To maintain constant power of 13.8 kW and respective temperature at the inlet in the flow, enthalpy in the flow is added through the heat of formation of nitrogen atom. It is the second term of Δh in Eq. 5.2. The heat of formation of molecular nitrogen is zero. To maintain constant power, the change in specific enthalpy needs to be constant. The value of the first term of Δh in the Eq. 5.2 decreases for a lower temperature as the change in temperature would be lower. Therefore, the second term of Δh in the Eq. 5.2 increases to compensate. It is achieved by an increase in the nitrogen atoms in the flow at the inlet.

The absolute nitrogen atom number density for varying inlet temperature for constant power is shown in Fig. 5.23. There is an approximately 4% increase in the number density in the boundary layer with every 1000 K increase in temperature for constant power. It is not significantly affected because the power in the flow is constant for all the three cases. Therefore, the enthalpy of the flow is constant for all three cases leading to similar level of dissociation.

The total heat flux and temperature at the wall for these cases are shown in Figs. 5.24 and 5.25, respectively. Both the heat flux and the temperature along the surface increase with increase in temperature when the power is kept constant. The mass removal flux shows a similar trend and is shown in Fig. 5.26. The total heat flux, wall temperature and mass removal flux are highest for the 8000 K case and lowest for

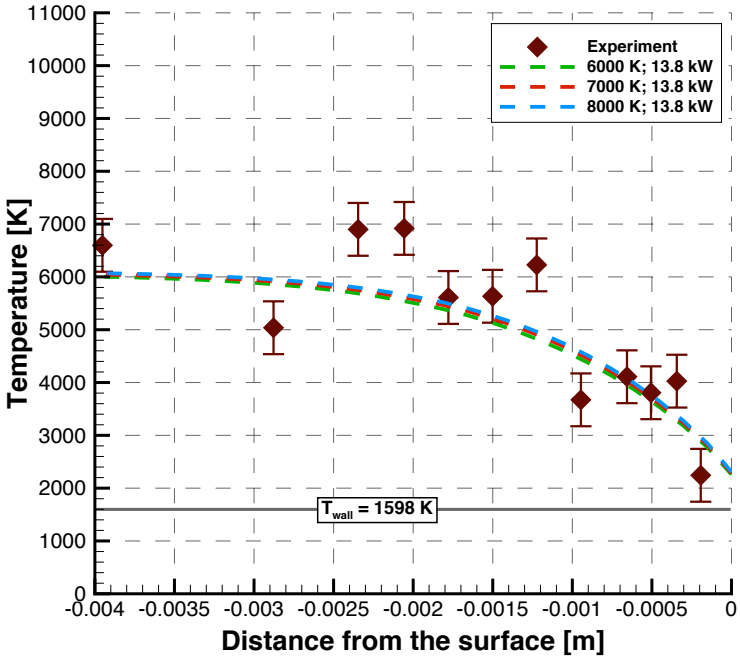

Figure 5.19: Comparison of translational temperature along the stagnation line in the boundary layer for varying temperature.

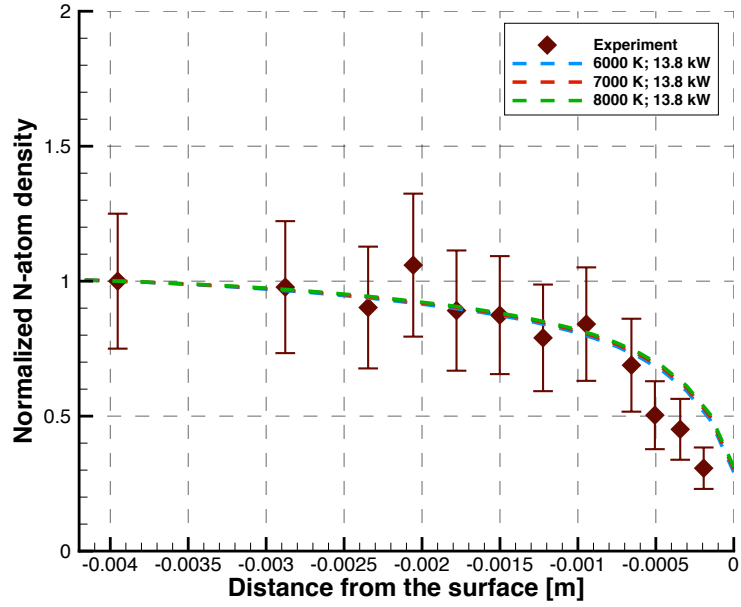

Figure 5.20: Comparison of normalized N-atom density along the stagnation line in the boundary layer for varying temperature.

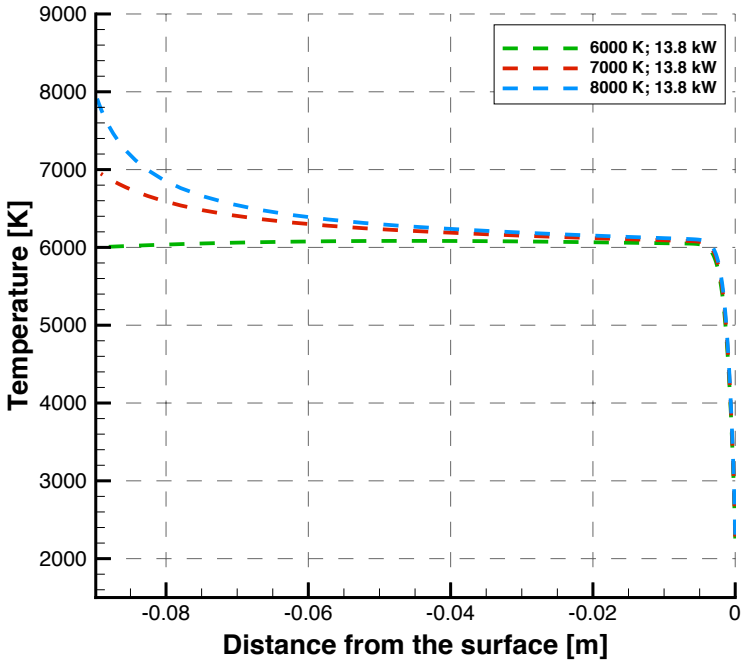

Figure 5.21: Comparison of translational temperature along the stagnation line for varying temperature.

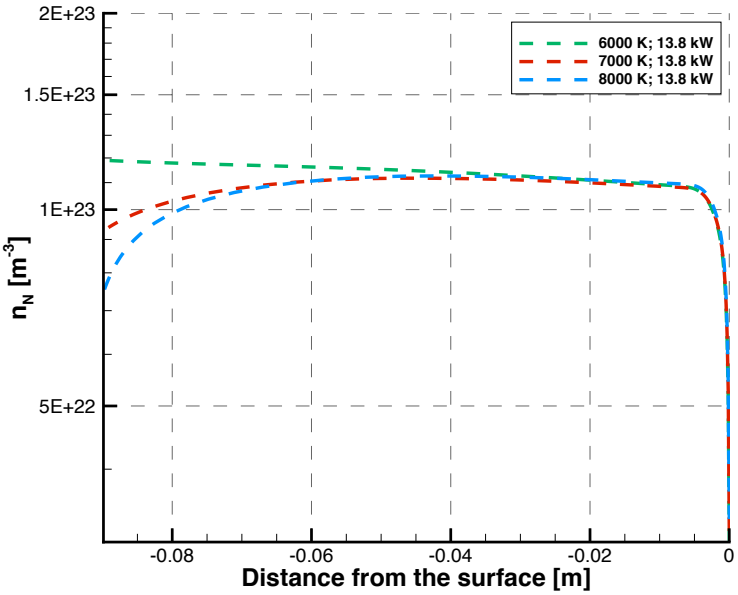

Figure 5.22: Comparison of N-atom number density along the stagnation line for varying temperature.

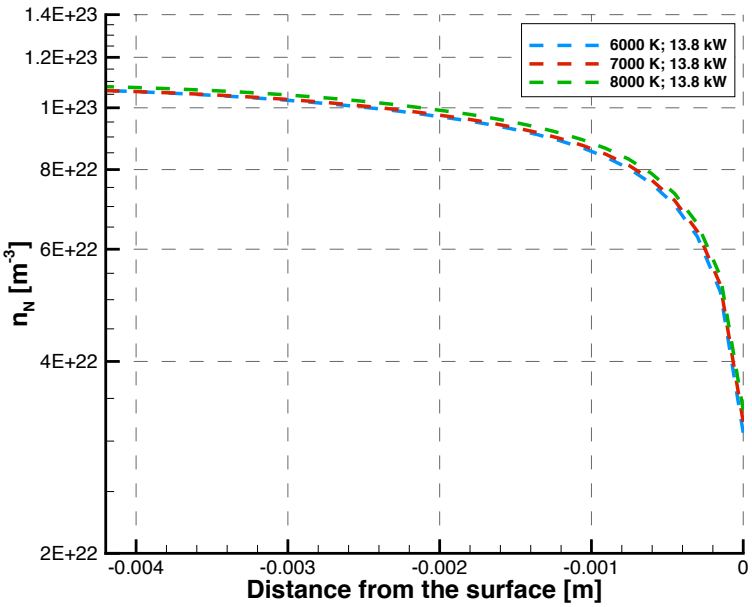

Figure 5.23: Comparison of N-atom number density along the stagnation line for varying inlet temperature.

the 6000 K case. Even though the level of dissociation is lower for higher temperature at the inlet (Fig. 5.22), as the flow progresses towards the test sample the level of dissociation increases due to a higher temperature. A higher number of atoms diffuse to the surface and recombine (both through catalytic activity and carbon nitridation), thus releasing heat of recombination into the surface. This explains the increase in the total heat flux, wall temperature and mass removal flux along the surface with increase in temperature. The comparison between the stagnation point values along with the mass loss rate for these cases is shown in Table 5.4. The respective experimental values are also shown in this table. It can be seen that the heat flux, wall temperature and the mass loss are increased by an increase in inlet temperature. The heat flux is increased by approximately 5%, wall temperature by 1%, and the mass loss by 4% for every 1000 K increase in temperature for constant power. The conclusion of this sensitivity study is that the effect of varying the inlet temperature for constant power on translational temperature and the nitrogen atom density in the boundary layer, surface heat flux, wall temperature and mass loss rate is relatively small and certainly

much smaller than the uncertainties in the measurements.

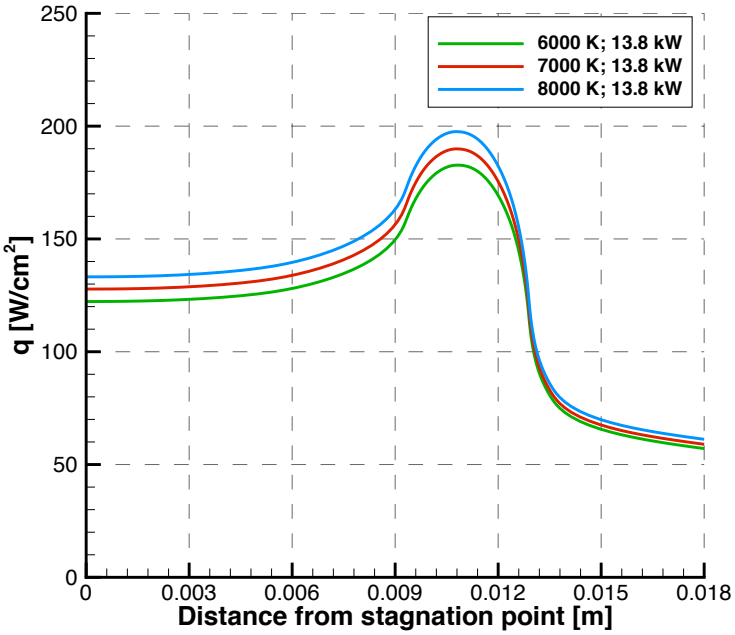

Figure 5.24: Comparison of wall heat flux between the computational results for varying inlet temperature.

Table 5.4: Stagnation point values and mass loss rate for varying temperature.

$Power[kW]$	T_{inf} [K]	$q_{stag}[W/cm^2]$	$T_{stag}[K]$	mass loss $[mg/s]$
13.8	6000	122	2259	0.83
13.8	7000	128	2284	0.86
13.8	8000	133	2308	0.89
Experiment	7000	40 - 80	1600	0.2 - 0.6

5.3.1.3 Sensitivity to Input Power

This section presents the sensitivity of the calculated flow field and surface parameters to varying input power for constant inlet temperature. The inlet temperature is 7000 K for all the cases. This is the experimentally measured value of temperature. Therefore, it is used as the reference temperature to analyze the sensitivity to input power. All the simulations are performed for Case 3 surface chemistry. The power is

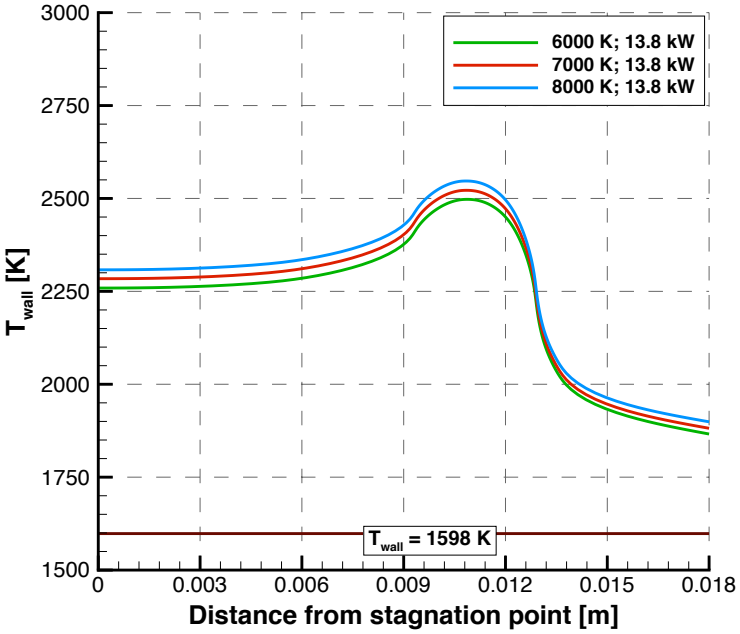

Figure 5.25: Comparison of wall temperature between the computational results for varying inlet temperature.

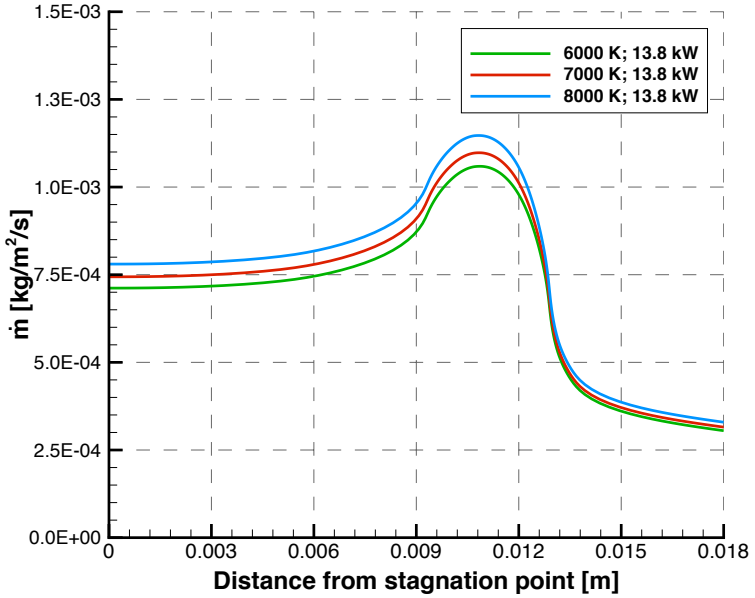

Figure 5.26: Comparison of mass removal flux for varying inlet temperature.

varied by varying the concentration of nitrogen atoms in the plasma mixture exiting the ICP.

The translational temperature profile along the stagnation line in the boundary layer is shown in Fig. 5.27. The respective profiles for 13.8 kW and 30 kW (chemical equilibrium) power are also included in the figure. The difference between the translational temperature profile in the boundary layer is within 1% for a change in power from 7.3 kW to 9.0 kW, 2% for 9.0 kW to 10.8 kW, 5% for 10.8 kW to 13.8 kW, and within 13% for 13.8 kW to 30 kW. This trend shows that the temperature is sensitive to the change in power. The reason for this is that the temperature in the flow increases with increase in enthalpy. Enthalpy is directly related to power (Eq. 5.2).

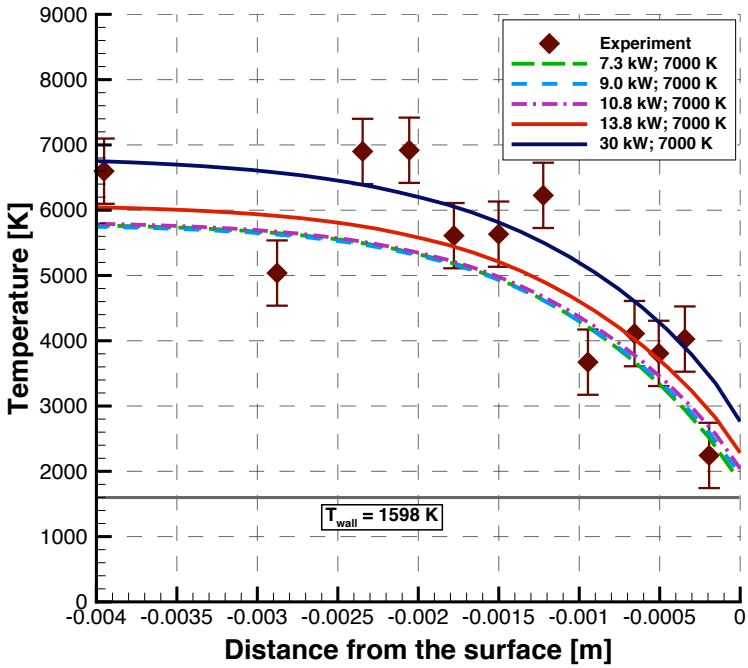

Figure 5.27: Comparison of translational temperature along the stagnation line in the boundary layer for varying power.

The normalized nitrogen atom number density along the stagnation line in the boundary layer is shown in Fig. 5.28. The respective profiles for 13.8 kW and 30 kW (chemical equilibrium) power are also included in the figure. The normalized nitrogen atom density is not significantly affected by power. The reason for this is that these

profiles are self normalized and the trend in the profiles is the same. Also, for all the conditions, the surface chemistry considered is the same. Therefore, the trend in the normalized profile is the same. The case with 30 kW power shows a difference within 10% from the 13.8 kW profile for the region close to the sample. The reason for this is that the 30 kW case is highly dissociated with a mole fraction of 0.85 at the inlet. This case has the same surface chemistry as the other cases. Therefore, a relatively higher density of nitrogen atoms is in the vicinity of the test sample as compared with the cases with lesser power and hence lower dissociation.

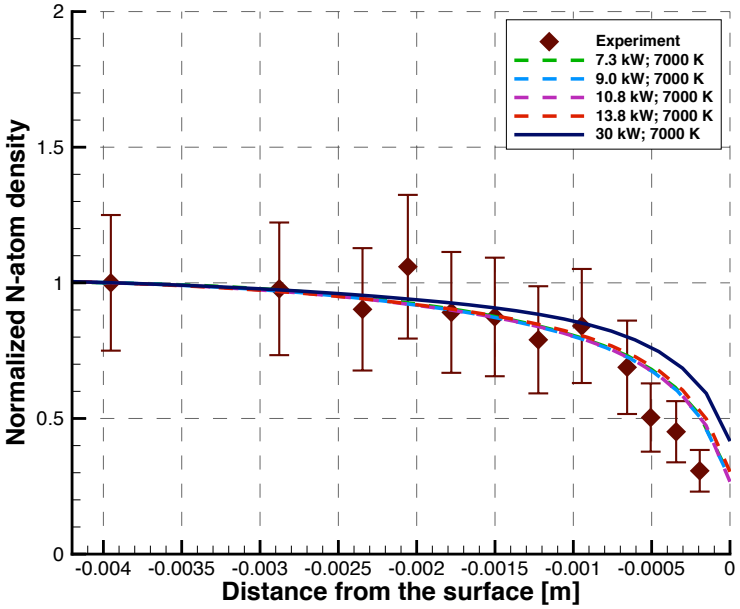

Figure 5.28: Comparison of normalized N-atom density along the stagnation line in the boundary layer for varying power.

Even though the normalized nitrogen atom density is not significantly affected by varying power, the absolute nitrogen atom number density is considerably affected as shown in Fig. 5.29. There is an approximately 117% increase in the atom number density in the boundary layer when the power is increased from 7.3 kW to 9.0 kW and a 48% increase for the variation in power from 9.0 kW to 10.8 kW, a 68% increase for 10.8 kW to 13.8 kW, and a 65% for 13.8 kW to 30 kW. The reason for the increase in the absolute nitrogen atom number density is the increase in enthalpy in the flow

due to increase in power. There is higher energy in the flow that leads to dissociation of nitrogen molecules. The higher the power, the higher the dissociation.

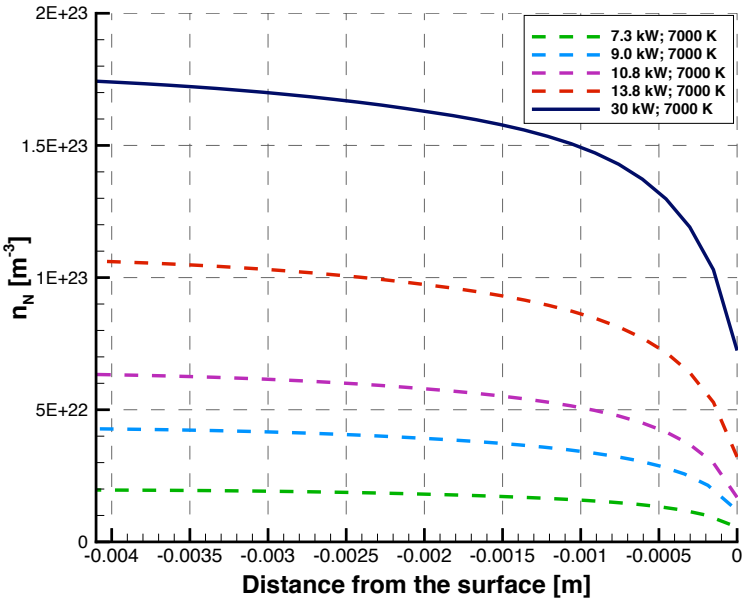

Figure 5.29: Comparison of N-atom number density along the stagnation line for varying inlet power.

This shows that the relative values for different test conditions can have similar profiles but the respective absolute values can vary considerably. It can be concluded from these results that it is very important to obtain absolute measured values for nitrogen atom number densities for validation of computational results with experimental data. The accurate validation of the simulations requires absolute number density measurements.

The translational temperature and nitrogen atom number density along the entire stagnation line for varying power and constant inlet temperature are shown in Figs. 5.30 and 5.31, respectively. The sensitivity to power can be seen in both the profiles. The temperature is the highest along the stagnation line for 30 kW power and is lowest for 7.3 kW power. This increase in temperature is directly attributed to the increase in enthalpy in the flow due to increase in power in the flow. The nitrogen atom number density is highest along the stagnation line for 30 kW power

and is the lowest for 7.3 kW power. The higher energy in the flow causes higher dissociation. Therefore, the dissociation is maximum in the flow for 30 kW power and minimum for 7.3 kW power. The flow is chemically reacting and as it progresses, the temperature starts decreasing as the nitrogen atom number density starts increasing. For example, at 7.3 kW power, the flow has zero nitrogen atom mole fraction, i.e. it is fully molecular. As the flow stream progresses towards the test sample, for a high temperature of 7000 K, the level of dissociation increases and hence the nitrogen atom number density increases.

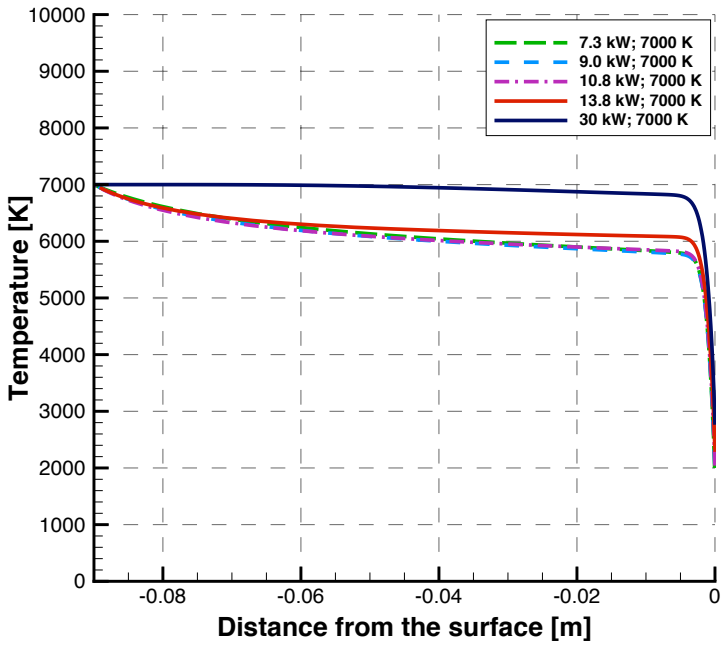

Figure 5.30: Comparison of translational temperature along the stagnation line for varying power.

The total heat flux and temperature at the wall for these cases are shown in Figs. 5.32 and 5.33, respectively. The mass removal flux is shown in Fig. 5.34. The wall heat flux, wall temperature and the mass loss increase with increase in the power. This increase is explained by the higher flux of nitrogen atoms at the test article surface. Therefore, a higher number of atoms recombine at the surface catalytically and release heat of recombination into the surface, thus increasing the heat flux and

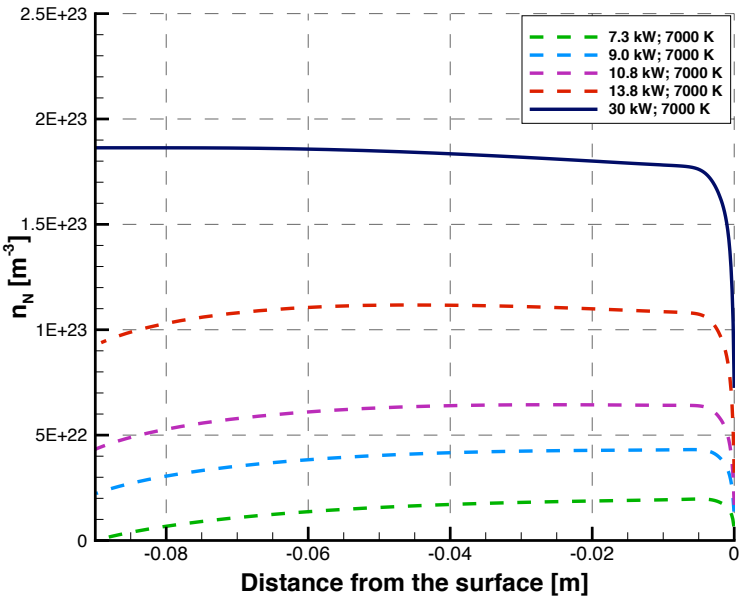

Figure 5.31: Comparison of N-atom number density along the stagnation line for varying power.

wall temperature along the test article surface. The higher flux of nitrogen atoms also causes more carbon nitridation and thus higher mass loss is experienced for higher power.

Table 5.5: Stagnation point values and mass loss rate for varying power.

Power $[kW]$	X_N	T_{inf} [K]	q_{stag} $[W/cm^2]$	T_{stag} $[K]$	mass loss $[mg/s]$
30	0.85	7000	270	2757	2.2
13.8	0.42	7000	128	2284	0.86
10.8	0.2	7000	82	2041	0.42
9.0	0.1	7000	66	1934	0.27
7.3	0	7000	52	1821	0.11
Experiment		7000	40 - 80	1600	0.2 - 0.6

The comparison between the stagnation point values and the mass loss rate for these cases along with the experimentally measured values is shown in Table 5.5. There is an approximately 25% increase in heat flux both for an increase in power from 7.3 kW to 9.0 kW and from 9.0 kW to 10.8 kW. The heat flux increases by approximately 56% when power is changed from 10.8 kW to 13.8 kW and an increase

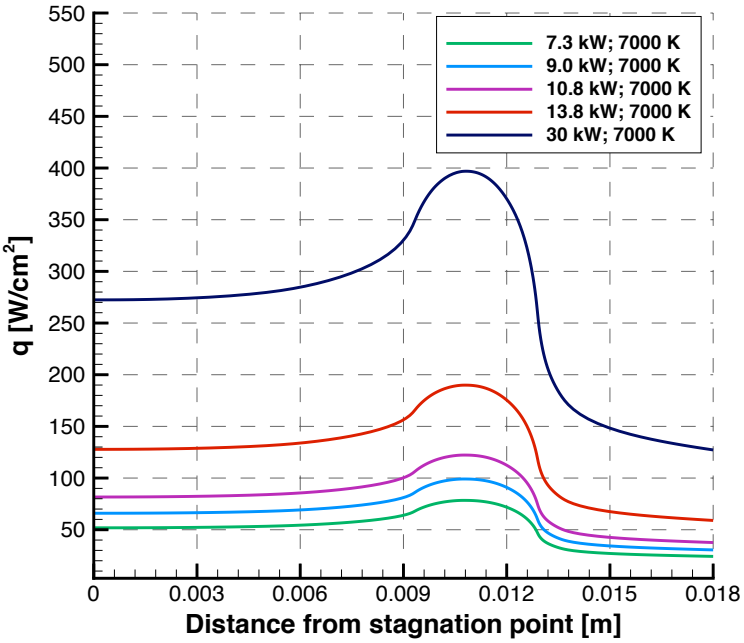

Figure 5.32: Comparison of wall heat flux between the computational results for varying power in the flow.

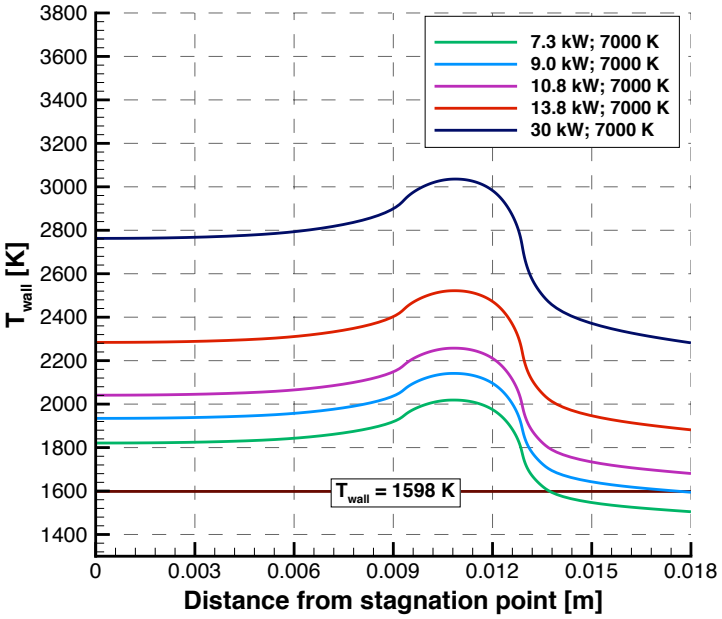

Figure 5.33: Comparison of wall temperature between the computational results for varying power in the flow.

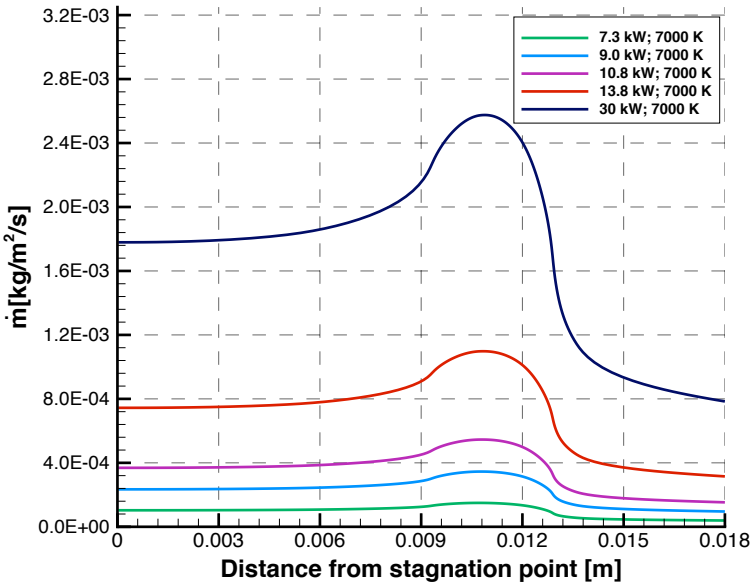

Figure 5.34: Comparison of mass removal flux for varying power.

of about 110% is observed for a change from 13.8 kW to 30 kW. There is a 6% increase in temperature at the wall both for an increase in power from 7.3 kW to 9.0 kW and from 9.0 kW to 10.8 kW. The increase in temperature at the wall is approximately 12% for an increase in power from 10.8 kW to 13.8 kW and an increase of 21% is observed for a change from 13.8 kW to 30 kW.

There is an approximately 145% increase in the mass loss rate when the power is increased from 7.3 kW to 9.0 kW, a 56% increase for the variation in power from 9.0 kW to 10.8 kW, a 105% increase for 10.8 kW to 13.8 kW and an increase of 155% is observed for a change from 13.8 kW to 30 kW.

It can be concluded from these results that the translational temperature and the nitrogen atom density in the boundary layer, surface heat flux, wall temperature and mass removal flux along the test article surface are highly sensitive to power in the flow. Therefore, it is very important to experimentally characterize the power absorbed by the plasma in the ICP torch. The necessity of experimental measurements of absolute atom number densities is again shown by these results. The amount of nitrogen atom flux in the boundary layer directly affects the heat transferred, wall

temperature and mass loss rate. Therefore, the absolute number density is required to draw conclusions about the surface chemistry models as well as the surface reactions involved.

5.3.2 Effect of varying carbon nitridation efficiency

The effects of varying carbon nitridation efficiency on the flow and surface properties are analyzed in this section. The results for Case 3 ($\gamma_{CN} = 0.005$; $\gamma_N = 0.07$) are compared with the results of the simulation for $\gamma_{CN} = 0.3$ and $\gamma_N = 0.07$. The free stream conditions for both the simulations are for 9.0 kW power and 7000 K temperature. The value $\gamma_{CN} = 0.3$ is set based on a value determined by Park and Bogdanoff [74]. It was measured in a shock tube by passing highly dissociated nitrogen over a grid of tungsten wire coated with carbon. The profiles for translational temperature and normalized nitrogen atom number density in the boundary layer are shown in Figs. 5.35 and 5.36, respectively. The results showe that the temperature in the boundary layer is unaffected. The normalized nitrogen atom number density does not show significant differences as well. The reason for this is the use of the same flowfield conditions in both the simulations. However, in the vicinity of the surface, the nitrogen atom density decreases for $\gamma_{CN} = 0.3$ as compared to 0.005. The reason for this is the higher carbon nitridation efficiency. A higher number of nitrogen atoms are consumed to form gaseous CN for $\gamma_{CN} = 0.3$. Therefore, the density of nitrogen atoms decreases.

The total heat flux and temperature at the wall for these cases are shown in Figs. 5.37 and 5.38, respectively. The mass removal flux is shown in Fig. 5.39. It can be seen that there is a decrease in heat flux and wall temperature when there is an increase in carbon nitridation. The reason for this is the lower heat of formation of the CN molecule as compared to the nitrogen molecule. All the surface reactions considered are exothermic. The heat of formation for nitrogen is 940 kJ/mol and for

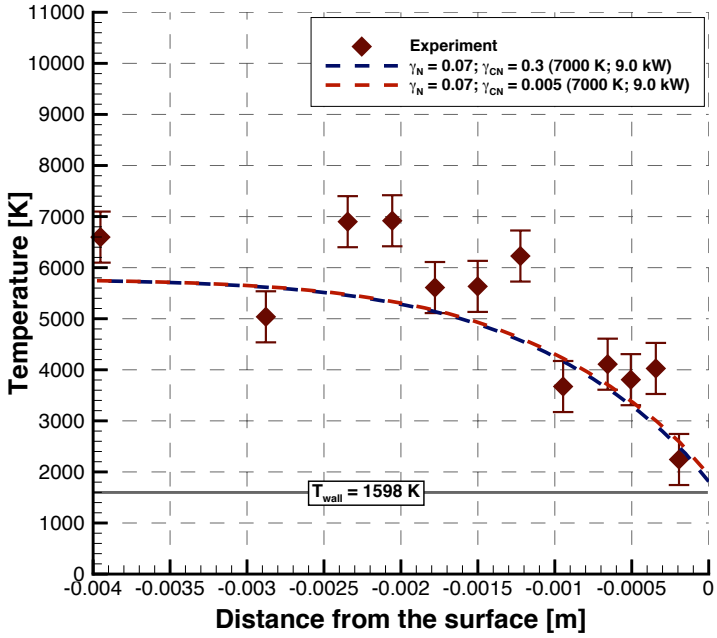

Figure 5.35: Comparison of translational temperature along the stagnation line in the boundary layer for varying carbon nitridation efficiency.

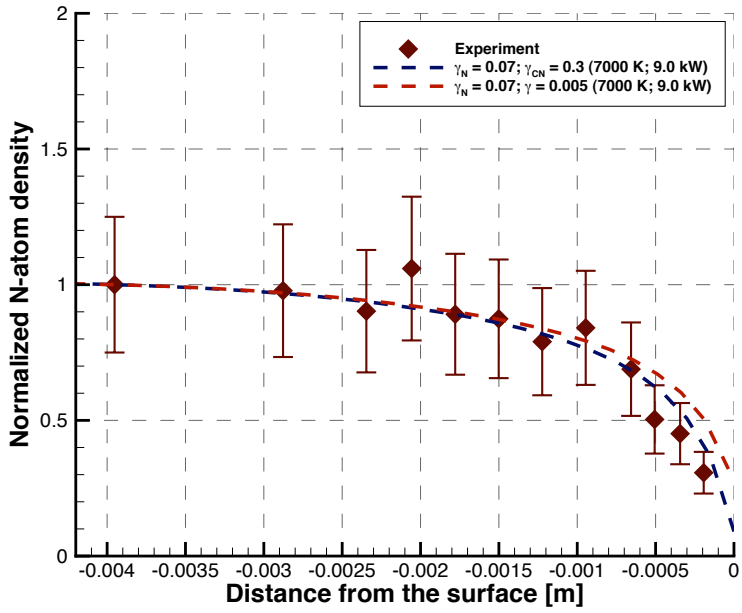

Figure 5.36: Comparison of normalized N-atom density along the stagnation line in the boundary layer for varying carbon nitridation efficiency.

CN, it is 590 kJ/mol. In both the simulations, the surface is exposed to the same nitrogen atom flux due to same free stream conditions. For the same nitrogen catalytic efficiency, more nitrogen atoms react with surface carbon from the available nitrogen atoms for the $\gamma_{CN} = 0.3$ case. Therefore, less energy is released in this process as compared to the $\gamma_{CN} = 0.005$ case. Less energy relates to less heat transferred and that relates to a lower temperature at the surface. As expected, the mass removal flux increases drastically with higher carbon nitridation efficiency. The reason being the higher consumption of nitrogen atoms to form gaseous CN for $\gamma_{CN} = 0.3$ as compared to 0.005 for the same nitrogen atom influx at the surface.

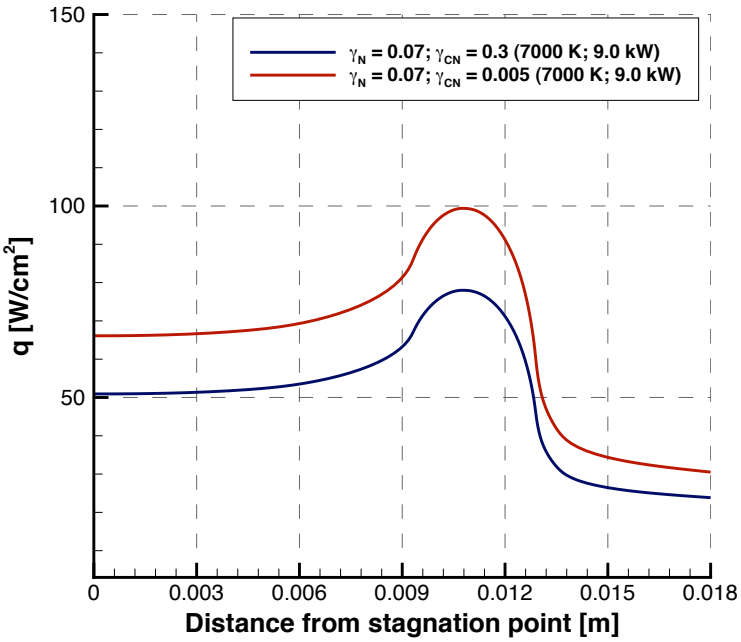

Figure 5.37: Comparison of wall heat flux between the computational results for varying carbon nitridation efficiency.

The comparison between the stagnation point values and the mass loss rate for these cases along with the experimentally measured values is shown in Table 5.6. The stagnation point heat flux is reduced by approximately 29% and the wall temperature by around 7%. The mass removal flux along the test article surface increased for $\gamma_{CN} = 0.3$ as compared to 0.005. The increase in mass loss rate is approximately by a factor of 20. The conclusion drawn from this analysis is that the surface reaction

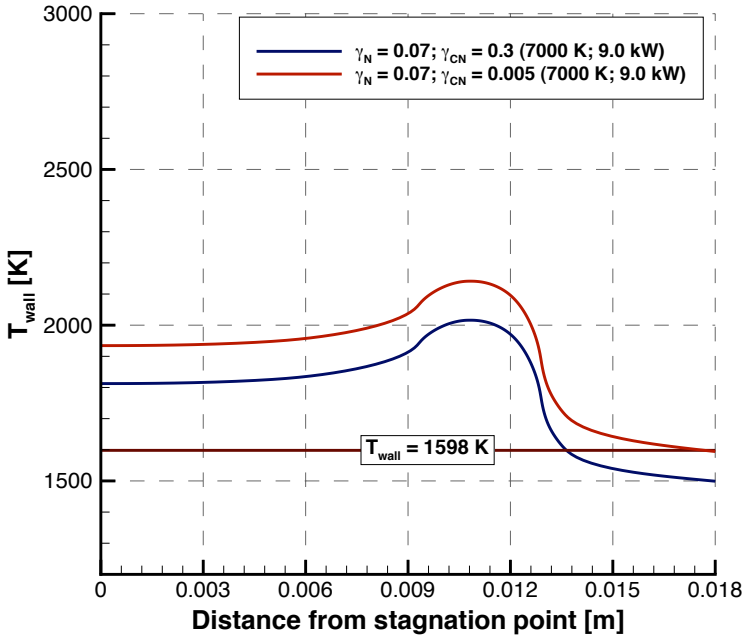

Figure 5.38: Comparison of wall temperature between the computational results for varying carbon nitridation efficiency.

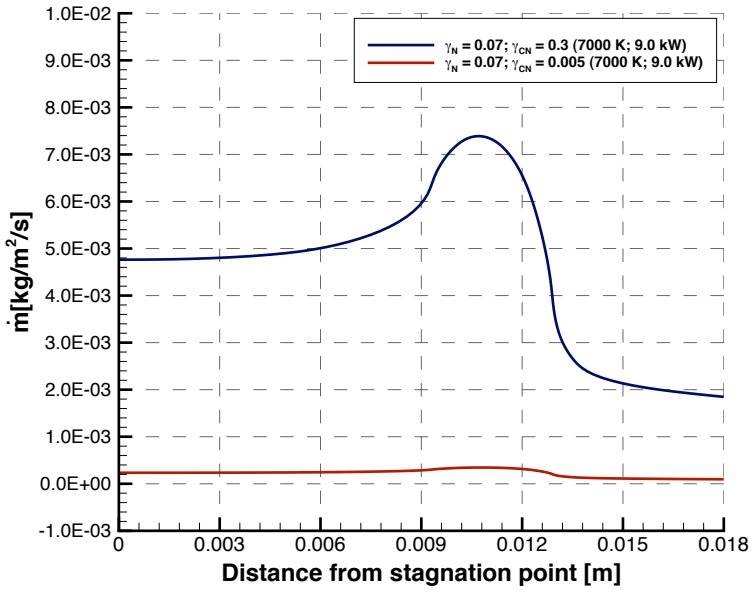

Figure 5.39: Comparison of mass removal flux for varying carbon nitridation efficiency.

efficiency has a very significant effect on the surface properties. Also, the reaction efficiency is of the order of $\gamma_{CN} = 0.005$. $\gamma_{CN} = 0.3$ is very high and leads to incorrect predictions. The wrong value of this parameter can result in incorrect predictions of surface properties.

Table 5.6: Stagnation point values and mass loss rate for varying carbon nitridation efficiency.

Power $[kW]$	X_N	T_{inf} [K]	γ_{CN}	q_{stag} $[W/cm^2]$	T_{stag} $[K]$	mass loss $[mg/s]$
9.0	0.1	7000	0.005	66	1934	0.27
9.0	0.1	7000	0.3	51	1812	5.37
Experiment	$\sim$	7000	$\sim$	40 - 80	1600	0.2 - 0.6

The computed stagnation point heat flux and mass loss for 9.0 kW power are well within the range of the experimental data. The stagnation point temperature for this case is 21% higher than the experimental value. The temperature at the wall is affected by the net heat transfer to the surface. The effects of conduction within the sample are therefore determined and the results are presented in the following section.

5.3.3 Accounting for conduction into the wall

The net heat transfer to the wall is expected to have an impact on the surface properties. The contribution of conductive heat transfer within the sample is determined by using the material response code MOPAR. The coupling of MOPAR with LeMANS is described in Section 2.4.5. The material properties of DFP2 grade POCO Graphite [86] are used in MOPAR. The properties specified are thermal conductivity, specific heat and emissivity of graphite. The case with 9.0 kW power has the best agreement with the experimental data for stagnation heat flux and mass loss. Therefore, this case is used to account for the effects of conduction within the sample. All the simulations are performed for Case 3 surface chemistry. The results from the

simulations for this analysis are presented in this section.

The solid grid used is shown in Fig. 5.40. It is an unstructured grid with 2,100 cells. The boundary of the grid exposed to the flowfield is set as a wall boundary condition calculated by Eq. 2.34. The back wall temperature is set to 350 K based on the measured back temperature of the copper slug [54]. This value is used as the back temperature of the graphite test article as it is not measured experimentally. MOPAR runs for 300 s and and then passes the respective wall temperature value to LeMANS. This time is chosen as the heat flux is measured experimentally after a 300 s exposure time to nitrogen plasma. The equations in LeMANS are solved for 200 iterations. The process is repeated until a converged steady state solution is obtained.

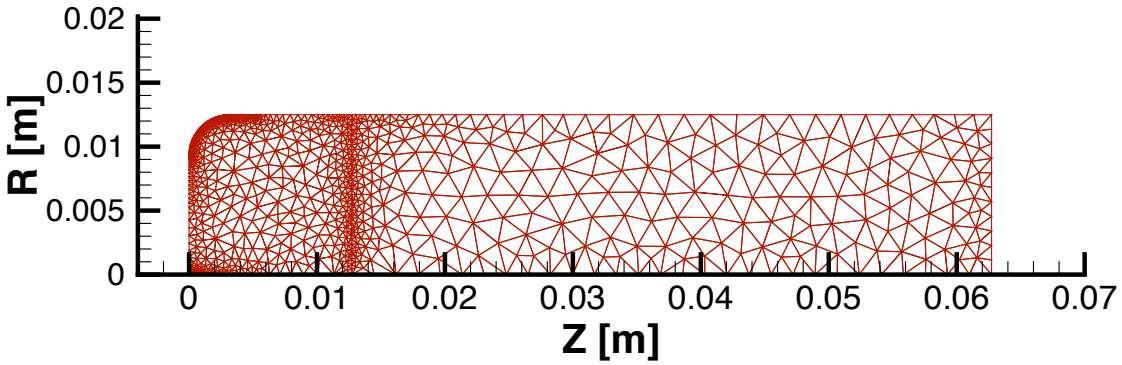

Figure 5.40: Computational grid of the graphite test article for configuration 2.

The results from this simulation are compared with the results for the radiative equilibrium wall boundary condition. The contours for temperature in the flowfield and within the solid test article are shown in Fig. 5.41. In this picture, the legend $T_{flowfield}$ shows the variation of translational temperature in the flowfield and T_{solid} shows the variation of temperature within the solid.

The flow enters from the ICP torch exit on the left and impinges on the graphite sample at the right. The front of the graphite sample is exposed to hot nitrogen plasma. The flow field contours of temperature show the way in which the hot nitro-

gen plasma evolves on exiting the ICP torch. The temperature contours within the graphite sample show the temperature gradient within the sample. The sample is at the highest temperature in the front region that is exposed to hot nitrogen plasma and it is the lowest at the back that is maintained at a 350 K back temperature.

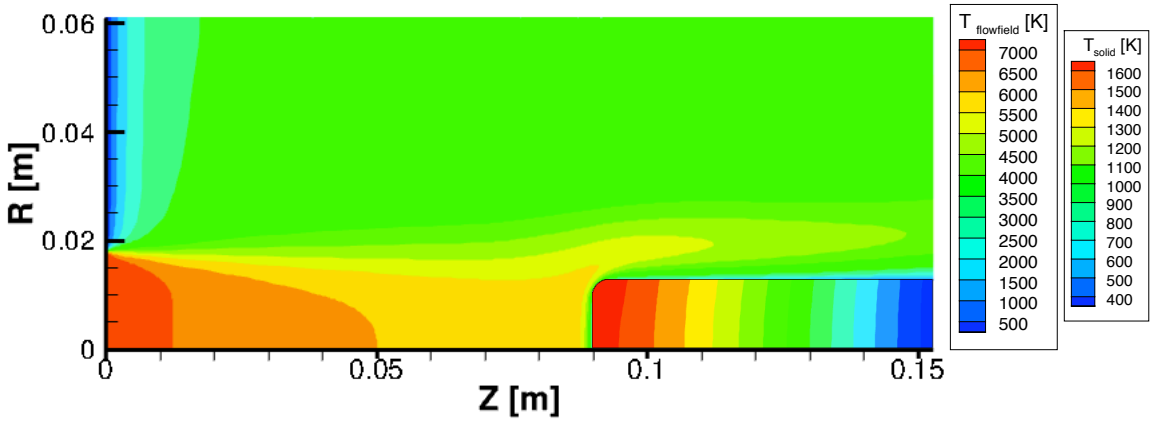

Figure 5.41: Temperature contours for the flowfield and within the solid test article.

The stagnation line profiles for translational temperature and normalized nitrogen atom number density in the boundary layer are shown in Figs. 5.42 and 5.43, respectively. It can be seen that there is no significant change in the temperature and normalized nitrogen atom number density in the boundary layer when conduction within the sample is included in the calculations. The reason for this is the same flowfield conditions are employed in both the simulations. However, in the vicinity of the surface, the temperature drops and nitrogen atom density rises for the case with conduction as compared to the radiative equilibrium case. The reason for this is explained by the surface properties.

The comparison for the total heat flux and temperature at the wall are shown in Figs. 5.44 and 5.45, respectively. There is an approximately 5% increase in heat flux and 17% reduction in temperature when heat is allowed to conduct into the material. The temperature decrease results in an increase in conductive heat flux as the change in temperature at the wall increases. This drop in temperature at the wall reduces

the temperature in the flow in the vicinity of the surface. When the temperature decreases, the density of nitrogen atoms increases to maintain constant pressure in the flow field.

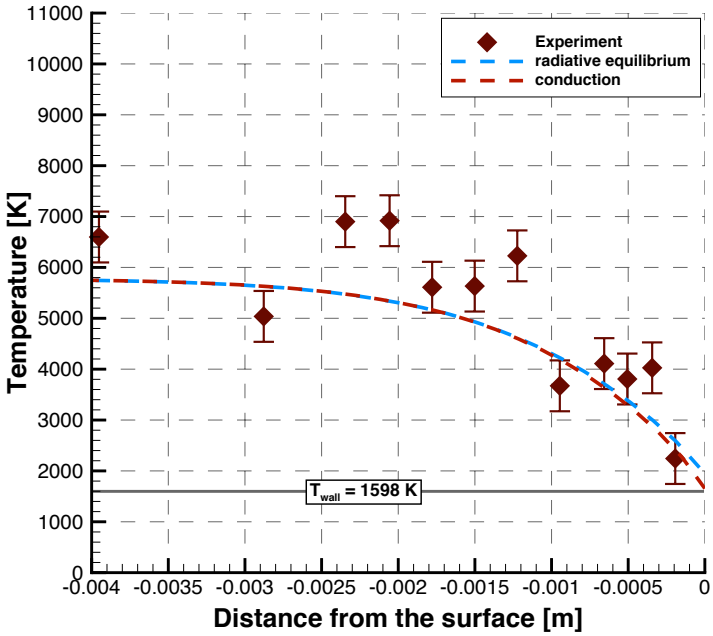

Figure 5.42: Comparison of translational temperature along the stagnation line in the boundary layer for different energy balance conditions at the wall.

The mass removal flux is shown in Fig. 5.46. There is no significant effect of conduction within the sample on mass removal flux. The reason for this is that the mass removal flux depends on the nitrogen atom density and square root of temperature (Eq. 2.30). When conduction is taken into account the wall temperature decreases but the nitrogen atom density increases. For the radiative equilibrium case, the wall temperature increases but the nitrogen atom density decreases. Therefore, no change is observed in the mass removal flux between the two cases.

The comparison between the stagnation point values for these cases along with the experimental data is shown in Table 5.7. There is an approximately 5% increase in stagnation point heat flux when conduction is included. There is an approximately 300 K drop, i.e. 17%, in stagnation point temperature when conduction into the wall is accounted for. The mass removal rate remains unchanged. The stagnation point

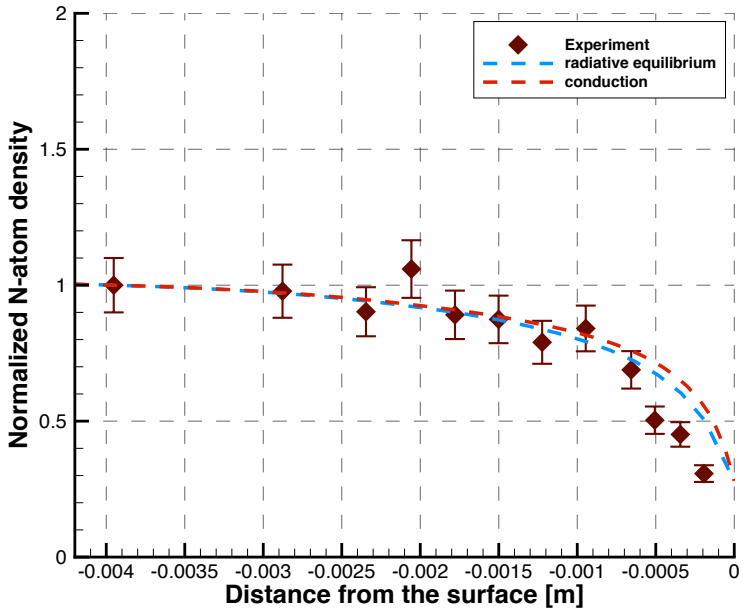

Figure 5.43: Comparison of normalized N-atom density along the stagnation line in the boundary layer for different energy balance conditions at the wall.

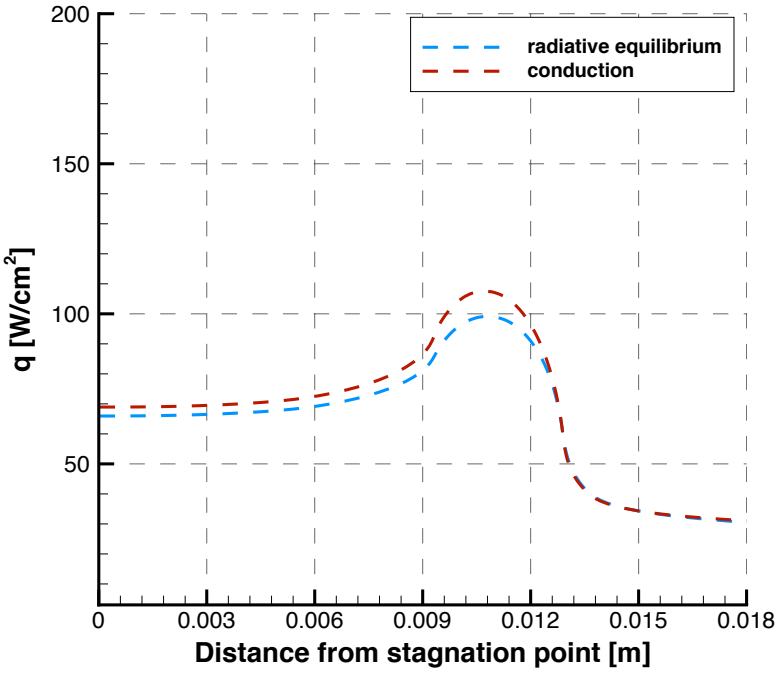

Figure 5.44: Comparison of wall heat flux between the computational results for different energy balance conditions at the wall.

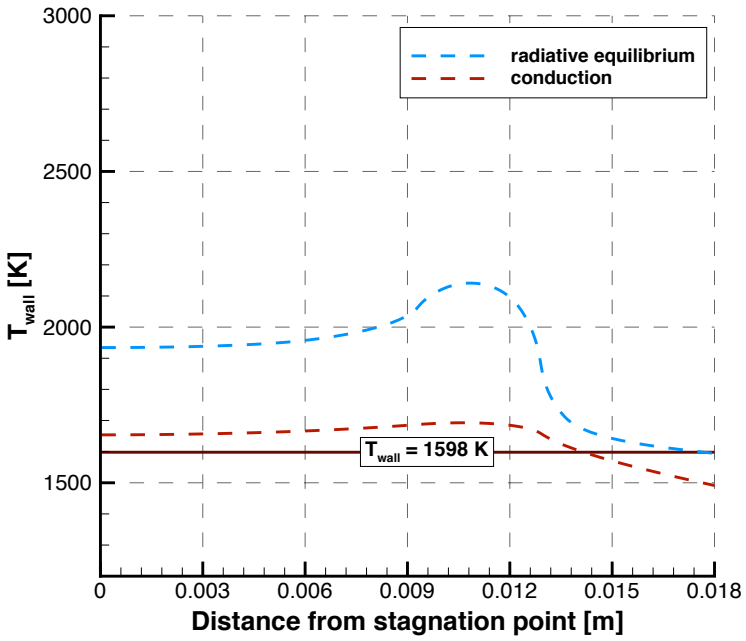

Figure 5.45: Comparison of wall temperature between the computational results for different energy balance conditions at the wall.

heat flux, temperature and mass loss for 9.0 kW power with conductive heat transfer within the sample shows the best agreement with the experimental data. This shows that it is important to include conductive heat transfer within the sample in the energy balance at the wall in such calculations. The results that good agreement of computations with all experimental measurements is obtained if all the flow, surface and material physics are included in the simulations.

It can also be concluded from these results that the power in the flow is much less than the estimated power of 13.8 kW. As mentioned earlier, the back face temperature of the graphite test article is not measured experimentally. Therefore, sensitivity of the surface properties to the back temperature is determined. A simulation is performed for a back face temperature of 400 K for the same flowfield conditions of 9.0 kW. The stagnation point temperature obtained from the simulations for this case is 1670 K that represents a 1% increase for a 50 K increase in the back temperature. No change is observed in the stagnation point heat flux.

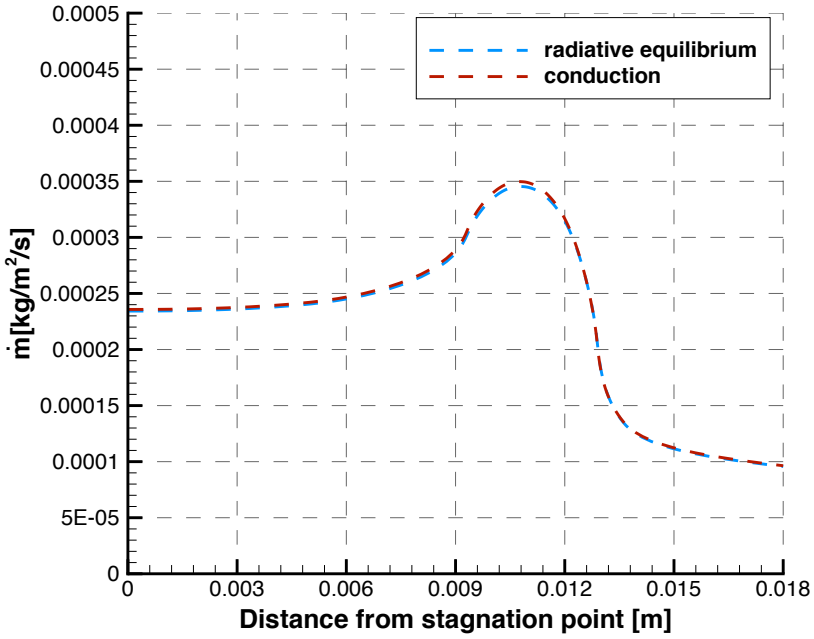

Figure 5.46: Comparison of mass removal flux for different energy balance conditions at the wall.

Table 5.7: Stagnation point values and mass loss rates for different energy balance conditions at the wall.

	Power $[kW]$	T_{inf} $[K]$	q_{stag} $[W/cm^2]$	$T_{stag}[K]$	mass loss $[mg/s]$
Radiative equilibrium	9.0	7000	66	1934	0.27
Conduction	9.0	7000	69	1654	0.27
Experiment	13.8	7000	40 - 80	1600	0.2 - 0.6

Since the stagnation point heat flux is measured experimentally using a copper slug calorimeter, a simulation is performed for a copper test sample exposed to the same flow field conditions as used for the case of 9.0 kW power. The material properties of copper [2] are used in MOPAR. The properties specified are thermal conductivity, specific heat and emissivity of copper. A fully catalytic ($\gamma_N = 1$) boundary condition is used since copper is considered nearly fully catalytic [70]. This means that the heat flux measured for copper will provide the maximum heat flux for the respective flowfield conditions. The stagnation point heat flux obtained from the simulations is 84 W/cm^2 which is higher than the value of 69 W/cm^2 obtained for the graphite test sample. While this value is very close to the upper end of the values measured, it should also be noted that a copper surface frequently becomes oxidized [70] and this could affect the measured heat flux. Copper oxide has a lower catalycity and thus the heat flux measured for oxidized copper surface would be lower than for pure copper exposed to the same flowfield conditions.

5.4 Summary

The results of the numerical simulations of the experimental configuration obtained using the CFD code LeMANS are presented in this chapter. The numerical simulations are performed for Configurations 1 and 2 as described in Chapter III. Assessment of the computations is made using experimental tests that were conducted in the ICP torch facility. The comparisons between the numerical results and experimental measurements are presented for translational temperature and normalized nitrogen atom density in the boundary layer formed in front of the test sample. The test cases are considered to determine the effects of gas-surface interactions by considering different surface chemistry processes. The results from the simulations of both configurations showed that the temperature in the boundary layer is not significantly affected by different surface reactions whereas the nitrogen atom density decreased in

the boundary layer when surface chemistry is included. The nitrogen atom density for all cases except for the case with non-catalytic wall showed good agreement with the experimental measurements. A comparison is also performed between the simple binary catalytic recombination (BCR) model and the complex finite rate surface chemistry (FRSC) model. It is shown that both models produce the same results.

The effect of surface chemistry on surface properties is also determined. The properties analyzed are the surface heat flux and wall temperature. An increase in the total heat flux and wall temperature is observed for all the cases with surface reactions as compared to the non-catalytic wall. The heat flux and wall temperature are highest for a fully catalytic wall and are lowest for a non-catalytic wall providing the upper and lower bound values respectively for the total heat flux transferred and surface temperature. The carbon mass loss rate as a result of the carbon nitridation reaction is also computed and compared to the measured value. In addition, the computed stagnation point values for heat flux and surface temperature are also compared to the experimentally measured values. It is observed that the computational values are much higher than the experimentally measured values. An analysis of the plausible causes of these higher computational values is performed and the results are presented in this chapter.

The ICP torch exit conditions are not well defined and therefore, a sensitivity analysis is performed on the ICP torch exit gas chemical composition to evaluate its effects on the parameters in the boundary layer and the surface properties.

For the first part of the analysis, a comparison is performed between the simulations for chemical composition based on chemical equilibrium and that calculated from the power in the flow. It is shown in the results that there is a 52% reduction in stagnation point heat flux, a 17% reduction in stagnation wall temperature and a 60% reduction in mass loss rate for 13.8 kW power in comparison with equilibrium chemical composition at the inlet.

It was then followed by an evaluation of the effect on flowfield parameters and surface properties of varying inlet temperature for constant input power. The conclusion of this sensitivity study was that the effect of varying the inlet temperature for constant power on translational temperature and the nitrogen atom density in the boundary layer, surface heat flux, wall temperature and mass loss rate is negligible.

A sensitivity study was then performed to evaluate the effect on flowfield parameters and surface properties of varying flow power for constant inlet temperature. Based on these results it was be concluded that the temperature in the boundary layer is sensitive to change in power.

It was shown that the normalized nitrogen atom density is not significantly affected by changes in power. Even though the normalized nitrogen atom density is not significantly affected by varying power, the absolute nitrogen atom number density is considerably affected. There was an approximately 117% increase in the atom number density in the boundary layer when the power is increased from 7.3 kW to 9.0 kW and a 48% increase for the variation in power from 9.0 kW to 10.8 kW, a 68% increase for 10.8 kW to 13.8 kW, and a 65% for 13.8 kW to 30 kW. This showed that the relative values for different test conditions can have similar profile shapes but the respective absolute values can vary considerably. The conclusion drawn from these results is that it is very important to obtain absolute values for nitrogen atom number densities for validation of computational results with experimental data. Therefore, the accurate validation of the simulations requires absolute number density measurements.

It was concluded from this study that the translational temperature and the nitrogen atom density in the boundary layer, surface heat flux, wall temperature and mass removal flux along the test article surface are highly sensitive to power in the flow. Therefore, it is very important to characterize the power absorbed by the plasma in the ICP torch. The necessity of experimental measurements of absolute atom number densities was again shown by these results. The amount of nitrogen atom flux in the

boundary layer directly affects the heat transferred, wall temperature and mass loss rate. Therefore, the absolute number density is required to draw firm conclusions about the surface chemistry models as well as the surface reactions involved.

An analysis of the effect of the magnitude of the carbon nitridation efficiency (γ_{CN}) was also performed. The comparison was performed for γ_{CN} values of 0.005 and 0.3. The catalytic efficiency for nitrogen recombination was 0.07 for both cases. The results showed that the temperature in the boundary layer was unaffected. The normalized nitrogen atom number density did not show significant differences as well. However, the surface heat flux and wall temperature along the surface decreased for $\gamma_{CN} = 0.3$ as compared to 0.005. The stagnation point heat flux reduced by approximately 29% and the wall temperature by around 7%. The mass removal flux along the test article surface increased for $\gamma_{CN} = 0.3$ as compared to 0.005. The increase in mass loss rate was approximately 1900% when $\gamma_{CN} = 0.3$. The conclusion drawn from this analysis is that the surface reaction efficiency has a very significant effect on the surface properties.

Based on the computational results and their comparison with the experimental data, it can be concluded that the loss of nitrogen atoms observed in the experiment is caused by a combined effect of nitrogen recombination due to surface catalysis and the carbon nitridation reaction. In the last part of this chapter, the effects of conduction within the sample wall are included in the calculations and compared with the results from the radiative equilibrium condition. The purpose of this study is to evaluate the impact of heat conduction within the sample on the surface properties. It is shown that there is an approximately 17% drop in stagnation point temperature and a 5% increase in the stagnation point heat flux when conduction within the sample is considered. No significant effect of conduction within the sample on the mass loss rate is observed. It is concluded that it is important to include the conductive heat transfer within the sample in the energy balance at the wall to determine the accurate

surface temperature.

The results from the study in this dissertation show that good agreement of computations with all experimental measurements is obtained if all the flow, surface and material physics are included in the simulations.

CHAPTER VI

Conclusion and Future Directions

6.1 Summary

Atmospheric entry probes and hypersonic vehicles experience heat loads during an entry into the atmosphere of Earth or any other planet. At hypersonic speeds, shock waves form in front of the probe or vehicle that cause high temperatures and enthalpy in the flow. The high heat loads are due to the dissipation of kinetic energy of a high-speed flow that cause very high temperature on the vehicle surface. Therefore, such vehicles use a Thermal Protection System (TPS) for protection from aerodynamic heating. TPS is a single point of failure system as the prolonged exposure to high temperature can cause the TPS materials to fail. The need to design a reliable TPS necessitates good understanding of the physical and chemical processes that determine the aerothermal heating environment.

Depending on the heat load encountered during hypersonic flight, an ablative or non-ablative TPS may be used. Non-ablative or reusable materials (e.g., ceramic tiles used on the Space Shuttle with a peak heating of 60 W/cm^2) are used where the re-entry conditions are relatively mild while ablative TPS materials (e.g., heat shield for the Stardust mission with a peak heating of 942 W/cm^2) are used where relatively high heating rates are generated. There is no change in mass or properties of the non-ablative material whereas ablative TPS materials accommodate high heating

rates and heat loads through phase change and mass loss. Ablative TPS has been used for most planetary entry probes and high velocity Earth atmosphere re-entry vehicles. Most TPS to date are carbon and silicon carbide based. The total heat flux imparted to an ablative TPS surface consists of: (1) convective heating as a result of gas particle collisions and their interactions with the surface, and (2) radiative heating as a result of radiation from excited particles in the flow.

Catalycity of an ablative TPS material and surface-participating reactions that lead to surface recession are key factors that impact the heating of the vehicle surface. Very high temperatures in the boundary layer may cause the molecular species to dissociate. If the heated TPS material acts as a catalyst and dissociated atoms diffuse to the surface, it may cause recombination of these dissociated boundary layer species which increases the convective heating to the surface. Thus, a less catalytic surface is desirable to minimize this additional heating. Also, when the vehicle surface is heated, the surface material may react chemically with the boundary layer gases leading to surface recession as a result of surface material consumption. These chemical reactions can be endothermic (vaporization, sublimation) or exothermic (oxidation, nitration) and will affect the net heating to the surface. Reactions between the gases and an ablative TPS material surface consume the materials and in the process transform the surface as well. Therefore, detailed studies of these interactions that occur between the surface and the atmosphere gas are required for the accurate prediction of aerothermal heating of the vehicle TPS and in characterizing TPS materials.

The major objective of this dissertation was to investigate surface chemistry processes (e.g. catalysis, nitridation) using coupled CFD-surface chemistry models. Another objective was to assess the computations for surface chemistry models using experimental data. The effects of surface chemistry processes of a graphite sample exposed to a subsonic high-enthalpy nitrogen flow were investigated. The numeri-

cal simulations in this work were conducted using the Navier-Stokes computational fluid dynamics (CFD) code LeMANS developed at the University of Michigan. The investigation was performed using a finite rate surface chemistry model (FRSC). It can account for different surface reactions such as particle adsorption/desorption, the recombination of an atom of the gas with an atom adsorbed on the wall [Eley-Rideal (E-R) reaction] as well as reactions leading to surface recession. The FRSC model was developed by Marschall and Maclean [61, 57] and was implemented in LeMANS by Alkandry *et.al* [8].

Computational Fluid Dynamic (CFD) models can be used for simulating environments that cannot be studied in an experimental test facility. These models can be used for predicting the aerothermal environment of the vehicle TPS during entry but these models can be used to perform such analysis only after they have been validated for physical accuracy by comparison with experimental measurements.

Another objective of this dissertation was to assess the computations for surface chemistry models using experimental data. Experimental data for flow and surface properties from tests conducted in the 30 kW Inductively Coupled Plasma (ICP) Torch Facility at the University of Vermont were used for the evaluations of the computations for different surface chemistry (gas-surface interactions) processes. This facility is configured for operation with subsonic flow to simulate post shock conditions of high enthalpy flight for a stagnation point geometry.

The characterization of a TPS material requires it to be tested in an experimental facility that can create conditions similar to real entry flight conditions. The current ground test facilities can not simulate all environmental entry conditions simultaneously. Lack of adequate ground test facilities for the development of new TPS materials is an issue. To accommodate for these limitations, a piecewise certification strategy is used. Each facility has a certain capability of simulating the entry environment conditions. The respective capability of each facility along with

computational modeling is used to combine all the pieces together to develop a TPS design process. Therefore, a partial simulation of the flight conditions that involves post shock subsonic high-enthalpy flow was considered for the purpose of this study.

The experimental and computational techniques that were used to study the gas-surface interactions that occur on a vehicle surface during its entry into a planetary atmosphere were described in Chapter II. The description of the ICP facility at the University of Vermont along with an overview of the experimental techniques employed to obtain flow and surface property measurements was presented in this chapter. The facility is designed to test scaled material samples in high enthalpy gas flows for simulation of planetary entry trajectory heating conditions. Experimental results from graphite samples tested in the nitrogen plasma stream were used. The test articles were constructed from DFP2 grade POCO graphite.

The measured quantities were the surface heat flux, surface temperature, relative nitrogen atom number density and translational temperature in the reacting boundary layer above the graphite surface. The carbon mass loss was also quantified from pre- and post-test mass measurements. The stagnation region heat transfer was measured with a copper slug calorimeter. The surface temperature was measured using a two-color infrared optical pyrometer. The gas-phase flow properties, i.e., the relative nitrogen atom number density and translational temperature in the reacting boundary layer above the test article surface, were measured using a two-photon laser induced fluorescence (LIF) technique.

Next, an overview of the CFD code used in this work along with the description of surface chemistry (gas-surface interaction) models implemented in the code were provided. The numerical simulations in this work were conducted using the computational fluid dynamics (CFD) code LeMANS developed at the University of Michigan. It is a general purpose, parallel, three-dimensional code that solves the laminar Navier Stokes equations including chemical and thermal nonequilibrium effects on unstruc-

tured computational grids. In LeMANS, the inflow and outflow boundary conditions were specified for hypersonic flows. The flow in the case of an ICP torch test facility is subsonic in nature. Therefore, new inflow and outflow boundary conditions were implemented for subsonic flow conditions. Prior to this work, the wall catalycity effects were accounted for in LeMANS by choosing a non-catalytic or a super-catalytic surface as the species boundary condition. A non-catalytic boundary condition implies that there is no recombination of atoms on the surface. A super-catalytic condition means that the atoms that strike the surface recombine to the free stream gas composition. A fully-catalytic condition means that all atoms that strike the surface recombine to form molecules and a partially catalytic wall condition means that some atoms reflect at the surface and some recombine to form molecules.

In addition to surface catalysis, surface participating reactions are required to be included in the analysis for a thorough understanding of gas-surface interactions. Therefore, a simple binary catalytic recombination model and a complex finite rate surface chemistry model (FRSC) were implemented in LeMANS. The catalytic atom recombination model can be used to study the effects of surface catalysis but could only be applied to a binary gaseous mixture of atoms and molecules. The FRSC model can be used to investigate the effects of surface catalysis as well as surface participating reactions and can be applied to multiple gaseous species. The various wall temperature boundary conditions implemented in LeMANS were also discussed. The wall temperature could be set to an isothermal condition, i.e., heat transfer to the wall balances to maintain the prescribed wall temperature. It could be set to a radiative equilibrium boundary condition where the convective and diffusive heat flux balance with the radiative heat flux to determine the wall temperature. It could also be treated using a material response code MOPAR developed at the University of Michigan. MOPAR is coupled to LeMANS and can model heat conduction and pyrolysis processes within the material.

The conditions in the ICP torch test chamber simulated by LeMANS were based on the conditions used in the experiments at the University of Vermont in order to compare the computational results with the experimental measurements. A description of the numerical setup used in this study was presented in Chapter III. The geometry of the test article used in the experiments was provided. The simulations were performed for two sets of experimental conditions and a detailed description of these test conditions was presented in this chapter.

A description of surface reactions investigated to study gas-surface interaction processes was presented along with details on the composition of the gas-mixture considered. The gas-surface interaction processes studied were the recombination of nitrogen atoms to molecules at the surface due to catalysis, and carbon nitridation where nitrogen atoms react with the surface carbon to form gaseous CN. Carbon nitridation was studied as sample mass loss is observed in the experiment. Two sets of surface reactions were taken into account using the FRSC model. The first set was the surface reaction that accounted only for the nitrogen atom recombination on the wall due to surface catalysis. The second set included the nitrogen atom recombination on the wall due to surface catalysis along with the carbon nitridation reaction where the carbon from the surface reacts with the impinging nitrogen atoms. The test cases considered in this study to determine the effects of gas-surface interaction processes were also described.

This chapter provided the derivation of the formulation of the effective reaction efficiency γ for the respective surface reactions. All the test cases were investigated using a constant reaction efficiency $\gamma_{process}$. The effective reaction efficiency for a gas phase reactant consumed in a surface reaction process is the net result of competing finite-rate processes. The competing finite-rate processes studied in this dissertation were catalytic nitrogen recombination and carbon nitridation. The reaction efficiency for catalytic recombination of nitrogen atoms was denoted by γ_N and for carbon

nitridation, it was γ_{CN}. The surface reaction types considered were adsorption and Eley-Rideal (E-R) recombination to emulate a constant reaction efficiency for the surface chemistry processes analyzed.

The numerical simulations are influenced by various factors ranging from the mesh of the flow field to the geometry of the experimental facility. Chapter IV presented an analysis of these factors and their effects on the gas flow parameters and surface properties analyzed in this investigation. In the first section, a grid convergence study was performed to ensure the numerical solution is not affected by the grid of flowfield. The description of the grids used for the simulations of each configuration were also presented. This was followed by an assessment of the sensitivity of the flow around the graphite sample to the area of the test chamber included in the simulations. The entire width of the test chamber was included for one grid whereas only part of the test chamber was considered in another. It was concluded that excluding the side wall from the simulations does not affect the flow parameters and the surface properties for the graphite sample. It was also shown that the simulations were more than 10 times faster for the partial grid as compared to the grid for the entire test chamber.

In order to predict the flow in the test chamber of the ICP torch facility accurately, it is required to simulate flow in the test facility as closely as possible. Therefore, the second section of Chapter IV was focussed on identifying the flow components of the experimental tests that could influence the properties of the parameters in the region of interest. First, the effect of different physics of the flowfield was investigated. The flowfield was investigated for flow in thermal equilibrium, thermal nonequilibrium, and thermochemical nonequilibrium. A detailed description of the meaning of each of these conditions was also included in the discussion. The results showed that the flow studied is in a state of weak thermochemical nonequilibrium.

Next, there followed an analysis of the effect of the nature of the inlet profile on the flowfield and boundary layer parameters. The flow at the inlet of the test chamber,

i.e. the ICP torch exit, is non-uniform and it is difficult to measure the non-uniform inlet flow conditions experimentally. Therefore, the non-uniform inlet flow conditions were calculated at the University of Bologna using an ICP torch simulation code that models the plasma flow in the ICP torch used in the experimental tests. A detailed description of the Bologna simulations was provided in Chapter III. This non-uniform profile was used to obtain the numerical solution and was compared with that computed using the uniform inlet values. The results of the comparison between the two inlet profiles showed that the uniform profile provides better agreement with the experimental measurements of translational temperature whereas the non-uniform inlet profile provides better agreement with the experimental measurements of normalized number density. It was also concluded that the non-uniform inlet profile does not significantly affect the solution.

The results from the numerical simulations of the experimental configuration performed using the CFD code LeMANS were presented in Chapter V. The main calculated parameters analyzed were translational temperature, normalized nitrogen atom density, surface heat flux, surface temperature, and mass removal flux. The comparisons between the numerical results and experimental LIF measurements were presented for translational temperature and normalized nitrogen atom number density in the test sample boundary layer. The computational and experimental data compared for surface properties were stagnation point heat flux, wall temperature, and mass loss rate. The test cases were considered to determine the effects of gas-surface interactions by considering different surface chemistry processes. There were four test cases. The first case was where a wall with no surface chemistry was accounted for and was treated as non-catalytic. Second was the case using a partially catalytic wall where only the recombination of nitrogen atoms to molecules at the surface due to catalysis was included in the calculations. The value of the reaction efficiency for catalytic nitrogen recombination used was 0.07 based on an experimentally deter-

mined value for pure carbon. The third case accounted both for the nitrogen atom recombination on the wall due to surface catalysis and the carbon nitridation reaction where carbon from the surface reacts with the impinging nitrogen atoms. The nitrogen catalytic efficiency used for this case was 0.07. The value of carbon nitridation efficiency used was 0.005 based on a value determined by a comparison between data from arc jet tests performed for Phenolic Impregnated Carbon Ablator (PICA) in nitrogen and results from computational simulations. The fourth case simulated a fully catalytic wall boundary condition where it was assumed that all the nitrogen atoms that impinge on the surface recombine to form nitrogen molecules.

The results from the simulations showed that the temperature in the boundary layer is not significantly affected by different surface reactions whereas the nitrogen atom density decreased in the boundary layer when surface chemistry was included. The nitrogen atom density for all cases except for the case with non-catalytic wall showed good agreement with the experimental measurements.

A comparison was also performed between the simple binary catalytic recombination (BCR) model and the complex finite rate surface chemistry (FRSC) model. It was shown that both the models produce the same results. It can be concluded from these results that the BCR model can be successfully used to quantify the effects of surface catalysis in an investigation involving a binary gaseous mixture consisting of an atomic and molecular species. It can be used as a baseline model in the preliminary investigation of surface catalycity effects for different species on different materials before a rigorous investigation involving competing surface chemical reactions that require the use of the FRSC model.

The effect of surface chemistry on surface properties was also determined. The properties analyzed were the surface heat flux and wall temperature. An increase in the total heat flux and wall temperature was observed for all the cases with surface reactions as compared to the non-catalytic wall. This increase was due to the transfer

of heat of recombination of nitrogen atoms to form nitrogen molecules and carbon nitridation to form gaseous CN. The heat flux and wall temperature were highest for a fully catalytic wall and lowest for a non-catalytic wall providing the upper and lower bound values respectively for the total heat flux transferred and surface temperature. The heat flux transferred to the surface was increased approximately by a factor of 4 when the surface was fully-catalytic as opposed to a non-catalytic surface. The carbon mass loss rate as a result of the carbon nitridation reaction was also computed and compared to the measured value. In addition, the computed stagnation point values for heat flux and surface temperature were also compared to the experimentally measured values. It was observed that the computational values for all three properties were much higher than the experimentally measured values.

The plausible causes of these higher computational values were analyzed. The higher computed values could be a combined effect of various mechanisms. The carbon nitridation efficiency may be smaller and that would lower the mass removal rate. It could be attributed to a higher degree of nitrogen atom flux to the surface in the calculations. An assumption of chemical equilibrium of the nitrogen gas mixture at the exit of the quartz tube was used in these simulations. The equilibrium gas mixture composition is probably more dissociated than the composition for a chemically reacting flow with finite rate chemistry. Therefore, the flux to the test sample of dissociated nitrogen atoms available might be less than that used in these simulations. The higher mass loss rate computed from the CEA results as compared with the experimental value could be the result of a high number of nitrogen atoms reaching the test sample surface and combining with the surface carbon to form gaseous CN. A lower nitrogen atom flux to the surface would result in a lower mass removal rate. Therefore, a sensitivity analysis was performed on the ICP torch exit chemical composition to evaluate its effects on the flow parameters in the boundary layer and the surface properties.

First, comparison was performed between the sensitivity to chemical composition based on chemical equilibrium and that calculated from power in the flow. It was shown in the results that there is a 52% reduction in stagnation point heat flux, a 17% reduction in stagnation wall temperature, and a 60% reduction in mass loss rate for the assumption of 13.8 kW flow power in comparison with the use of equilibrium chemical composition at the inlet. The reason for this reduction is the lower nitrogen atom flux reaching the surface for the 13.8 kW power case as compared to the equilibrium chemical composition at the inlet. The atomic mole fraction in the gas mixture at the inlet for equilibrium chemical composition was 0.85 and for 13.8 kW power, it was 0.42.

Next, there followed an evaluation of the effect on flowfield parameters and surface properties to varying inlet temperature for constant input power. Three values of inlet temperature, i.e., 6000 K, 7000 K and 8000 K, were considered for 13.8 kW power. For every 1000 K, the difference between each respective profile both for translational temperature and the nitrogen atom density in the boundary layer was less than 1%. The surface heat flux was increased by approximately 5%, wall temperature by 1%, and the mass loss by 4% for every 1000 K increase in temperature for constant power. The conclusion of this sensitivity study was that the effect of varying the inlet temperature for constant power on translational temperature and the nitrogen atom density in the boundary layer, surface heat flux, wall temperature and mass loss rate was negligible.

A sensitivity study was then performed to evaluate the effect on flowfield parameters and surface properties to varying flow power for constant inlet temperature. The flow power values considered were 7.3 kW, 9.0 kW, 10.8 kW, 13.8 kW, and 30 kW. The inlet temperature was 7000 K for all the cases. The difference between the translational temperature profile in the boundary layer was within 1% for a change in power from 7.3 kW to 9.0 kW, 2% for 9.0 kW to 10.8 kW, 5% for 10.8 kW to 13.8 kW,

and within 13% for 13.8 kW to 30 kW. Based on these results it was concluded that the temperature in the boundary layer is sensitive to change in power. The difference in respective temperature profiles increases as the power in the flow increases.

It was shown that the normalized nitrogen atom density was not significantly affected by changes in power. Even though the normalized nitrogen atom density was not significantly affected by varying power, the absolute nitrogen atom number density was. There was an approximately 117% increase in the atom number density in the boundary layer when the power was increased from 7.3 kW to 9.0 kW and a 48% increase for the variation in power from 9.0 kW to 10.8 kW, a 68% increase for 10.8 kW to 13.8 kW, and a 65% for 13.8 kW to 30 kW. This showed that the relative values for different test conditions can have similar profiles but the respective absolute values can vary considerably. The conclusion drawn from these results is that it is very important to obtain absolute values for nitrogen atom number densities for validation of computational results with experimental data. Therefore, the accurate validation of the simulations requires absolute number density measurements.

The wall heat flux, wall temperature and the mass removal flux increased with increase in the flow power. There was an approximately 25% increase in heat flux both for an increase in power from 7.3 kW to 9.0 kW and from 9.0 kW to 10.8 kW. The heat flux increased by approximately 56% when power was changed from 10.8 kW to 13.8 kW, and an increase of about 110% was observed for a change from 13.8 kW to 30 kW. There was a 6% increase in temperature at the wall both for an increase in power from 7.3 kW to 9.0 kW and from 9.0 kW to 10.8 kW. The increase in temperature at the wall was approximately 12% for an increase in power from 10.8 kW to 13.8 kW and an increase of 21% was observed for a change from 13.8 kW to 30 kW. There was an approximately 145% increase in the mass loss rate when the power was increased from 7.3 kW to 9.0 kW, a 56% increase for the variation in power from 9.0 kW to 10.8 kW, a 105% increase for 10.8 kW to 13.8 kW, and an increase of 155%

was observed for a change from 13.8 kW to 30 kW.

It was concluded from this study that the translational temperature and the nitrogen atom density in the boundary layer, surface heat flux, wall temperature and mass removal flux along the test article surface are highly sensitive to power in the flow. Therefore, it is very important to characterize the power absorbed by the plasma in the ICP torch. The necessity of experimental measurements of absolute atom number densities was again shown by these results. The amount of nitrogen atom flux in the boundary layer directly affects the heat transferred, the wall temperature, and the mass loss rate. Therefore, the absolute number density is required to draw conclusions about the surface chemistry models as well as the surface reactions involved.

An analysis of the effect of the magnitude of the carbon nitridation efficiency (γ_{CN}) was also performed. The comparison was performed between γ_{CN} values of 0.005 and 0.3. The catalytic efficiency for nitrogen recombination was 0.07 for both cases. The results showed that the temperature in the boundary layer was unaffected. The normalized nitrogen atom number density did not show significant differences as well. However, the surface heat flux and wall temperature along the surface decreased for $\gamma_{CN} = 0.3$ as compared to 0.005. The stagnation point heat flux reduced by approximately 29% and the wall temperature by around 7%. The mass removal flux along the test article surface increased for $\gamma_{CN} = 0.3$ as compared to 0.005. The increase in mass loss rate was approximately 1900% when $\gamma_{CN} = 0.3$. The conclusion drawn from this analysis is that the surface reaction efficiency has a very significant effect on the surface properties. The wrong value of this parameter can result in incorrect predictions of surface properties.

The computed values of heat flux, wall temperature and mass loss rate are affected by the net heat transfer to the surface. A radiative equilibrium boundary condition was used for the test article wall in these simulations where the heat conduction within the sample was not included, which if accounted for, affects the surface properties.

Therefore, the effects of conduction within the sample wall were included in the calculations using the material response code MOPAR and compared with the results from the radiative equilibrium condition.

There was an approximately 5% increase in the stagnation point heat flux when conduction within the sample was considered. The temperature dropped by approximately 17% at the stagnation point when conduction into the wall was accounted for as compared to the radiative equilibrium wall condition. No significant effect of conduction was observed on mass loss rate.

6.1.1 Contributions

The major objective of this dissertation was to investigate surface chemistry processes (e.g. catalysis, nitridation) using coupled CFD-surface chemistry models. Another objective was to assess the computations for surface chemistry models using experimental data. The effects of surface chemistry processes of a graphite sample exposed to a subsonic high-enthalpy nitrogen flow were investigated. The numerical simulations in this work were conducted using the Navier-Stokes computational fluid dynamics (CFD) code LeMANS developed at the University of Michigan. To assess the surface chemistry models, experimental data for flow and surface properties were used from tests conducted at a 30 kW Inductively Coupled Plasma (ICP) Torch Facility at the University of Vermont.

In order to achieve these objectives:

A simplified binary catalytic atom recombination model was successfully implemented. This model was used to quantify the effects of surface catalysis involving a binary gaseous (N_2-N) mixture. A finite rate surface chemistry (FRSC) model was successfully used to investigate the effects of both surface catalysis as well as surface participating reactions (eg. nitridation). The gas-surface interaction processes

studied were the recombination of nitrogen atoms to molecules at the surface due to catalysis, and the carbon nitridation reaction where nitrogen atoms react with the surface carbon to form gaseous CN. An expression was formulated for the effective reaction efficiency γ that takes into account both the effects of nitrogen catalytic efficiency and carbon nitridation. The effects of different surface chemistry processes viz. no surface chemistry, partial catalytic nitrogen recombination, partial catalytic nitrogen recombination along with carbon nitridation and fully catalytic nitrogen recombination were successfully compared. A sensitivity study was successfully performed for flowfield parameters and surface properties to varying inlet temperature for constant input power and varying input power for constant inlet temperature. It was concluded that the effect of varying the inlet temperature for constant power on translational temperature and the nitrogen atom density in the boundary layer, surface heat flux, wall temperature and mass removal flux is negligible. It was concluded that the translational temperature and the nitrogen atom density in the boundary layer, surface heat flux, wall temperature and mass removal flux along the test article surface are highly sensitive to power in the flow. It was concluded that it is very important to obtain absolute values for atom number densities for validation of computational results with experimental data. The effect of the magnitude of the carbon nitridation efficiency on surface properties was analyzed and it was determined that the reaction efficiency has a significant effect on the surface properties. The material response code MOPAR (coupled with LeMANS) was successfully used to evaluate the effects of heat conduction within the graphite test article. It was concluded that the heat flux transferred to the material increased, the surface temperature dropped and the mass removal flux remained unchanged.

In order to simulate the test conditions in the experimental facility accurately, it is required to simulate flow in the test facility as closely as possible. To achieve this objective:

The inflow and outflow boundary conditions were specified for hypersonic flows in LeMANS. The flow in the case of an ICP torch test facility is subsonic in nature. Therefore, new subsonic inflow and outflow boundary conditions were successfully implemented. The flowfield in the test chamber of the ICP facility were successfully investigated for flow in thermal equilibrium, thermal nonequilibrium, and thermochemical nonequilibrium . It was determined that the flow studied is in a state of weak thermochemical nonequilibrium. The effect of non-uniform nature of the inlet of the test chamber on the flow and surface properties was successfully investigated by comparison with uniform inlet flow. It was concluded that the non-uniform inlet profile does not significantly affect the solution.

The major contributions of this work are:

It was shown that a good agreement of computations with all experimental measurements was obtained only if all the flow, surface and material physics are included in the simulations. The values determined experimentally for nitrogen catalytic efficiency of $\gamma_N = 0.07$ [40] and for carbon nitridation efficiency of $\gamma_{CN} = 0.005$[32] were confirmed from comparison between experimental and computational results. It was identified that true validation of surface chemistry models requires absolute number density measurements. It was identified that validation of such simulations also requires better characterization of the power absorbed by the plasma in the ICP torch. It was shown that the effect of varying inlet temperature for constant power on flow properties (translational temperature and the nitrogen atom density in the boundary layer) and surface properties (surface heat flux, wall temperature and mass removal flux) is negligible. It was shown that the effect of varying flow power for constant inlet temperature on flow properties (translational temperature and the nitrogen atom density in the boundary layer) and surface properties (surface heat flux, wall temperature and mass removal flux) is highly significant. It was shown that the effect of reaction efficiency is significant on the surface properties. It was concluded

that it is very important to include the contribution of material response in analyzing the effects of surface chemistry processes.

Several other measurements needed from experiments to allow better validation of modeling were identified. To better model the material response, the back temperature value is critical. An analysis to determine the sensitivity of the surface properties to the back temperature was also performed in this study. It was concluded from this analysis that the surface temperature increased for a higher back face temperature. The test article is water cooled and will affect the temperature measurements on the surface. Therefore, a back temperature measurement will allow for a better estimate of surface properties. Also, measurement of flow temperature and absolute species densities at the inlet of the test chamber will allow for better estimation of inlet conditions. It was seen in all the computational results that the effect of inlet flow composition is very significant on both the flow and surface properties.

6.2 Future Directions

The physical approach taken to define the surface chemistry process in this dissertation is a promising starting point in the study of gas-surface interaction processes. The goal of this study was to understand the fundamental nature, and effects of gas-surface interactions. Therefore, interaction between nitrogen gas and graphite was studied. For future studies, interaction of different gases should be considered in the analysis, particularly oxygen. Oxygen is of importance both for Earth (for air) and Mars (for carbon dioxide).

During an Earth entry, molecular oxygen and nitrogen dissociate. Surface catalyzed and surface participating reactions involving these species should be considered for future studies. Examples of these reactions are catalytic recombination of nitrogen and oxygen atoms, reaction between surface carbon and oxygen and reaction between surface carbon and nitrogen. The knowledge that these reactions occur is in-

sufficient to determine the net heat transferred to the surface. The reaction pathway that these reactions take determines the net heat transferred. The energy released by each mechanism is different and its dominance in the surface reaction process will determine the total heat transferred. The various surface chemistry reactions are competing finite rate processes. The effect of each mechanism should be identified and an effort should be made to isolate the contribution of each mechanism. The finite rate surface chemistry model is capable of simulating different reaction mechanisms such as particle adsorption/desorption, the recombination of an atom of the gas with an atom adsorbed on the wall [Eley-Rideal (E-R) reaction], recombination of two adsorbed atoms at the wall [Langmuir-Hinshelwood (L-H) reaction] and reactions leading to surface recession (e.g. carbon nitridation, oxidation). The effect of various reaction mechanisms on the flow and surface properties should be identified. In this study, for the subsonic outlet boundary condition, a constant pressure boundary condition is implemented in which static pressure is specified at the outlet. The specified outlet pressure is used to compute the temperature variable using the equation of state. This boundary condition can reflect pressure disturbances back into the computational domain [78] and can delay convergence to steady state. To account for this, a characteristic boundary condition solved using Riemann invariants should be implemented for the subsonic outlet boundary condition.

Oxygen is highly reactive and should lead to a higher ablation rate (from carbon oxidation) as compared to nitrogen (from carbon nitridation). The shape of the test sample changes as the mass is removed. The changing shape of the sample is not accounted for in this dissertation due to the negligible ablation rate from carbon nitridation. The material response code MOPAR coupled to LeMANS can simulate the change in shape of the test sample. The effect of the shape change of the sample on the flow and surface properties should be analyzed.

Based on this fundamental frame work, LeMANS coupled with the finite rate

surface chemistry model along with the coupled material response code could be used for more complex surface chemistry studies for both charring and non-charring ablative thermal protection materials. The test sample material used in the analysis in this dissertation was graphite that is a non-charring material and it does not produce pyrolysis gases. A charring material could be considered in future studies and effects of pyrolysis gases could be identified. Also, after the computational surface chemistry models are validated with experimental results, they could be used to investigate the surface chemistry processes for particular entry trajectory conditions.

BIBLIOGRAPHY

BIBLIOGRAPHY

[1] http://aries.ucsd.edu/lib/props/panos/cu.html.

[2] http://www.goodreads.com.

[3] *An integrated strategy for the planetary sciences: 1995 - 2010*. Number NAS 1.26:195004; NASA-CR-195004. NASA, January 1994.

[4] *Introduction to Physical Gas Dynamics*. Krieger Pub Co., June 1975.

[5] *Hypersonic and High-Temperature Gas Dynamics*. AIAA; 2 edition, November 1, 2006.

[6] Hicham Alkandry. *Aerodynamic Interactions of Propulsive Deceleration and Reaction Control System Jets on Mars-Entry Aeroshells*. PhD thesis, University of Michigan, Ann Arbor, Michigan, 2012.

[7] Hicham Alkandry, Iain D. Boyd, and Alexandre Martin. Coupled flow field simulations of charring ablators with nonequilibrium surface chemistry. In *44th AIAA Thermophysics Conference*, number AIAA 2013-2634, San Diego, CA, June 24-27 2013.

[8] Hicham Alkandry, Erin D. Farbar, and Iain D. Boyd. Evaluation of finite-rate surface chemistry models for simulation of the stardust reentry capsule. In *AIAA Paper 2012-2874*, June 2012.

[9] A. J. Amar. Modeling of one-dimensional ablation with porous flow using finite control volume procedure. Master's thesis, North Carolina State University, 2006.

[10] R. Wernitz ans M. Fertig, G. Herdrich, S. Löhle, M. Winter, and H.P. Röser. Assessment of pwt conditions for the stardust post-flight evaluation. In *Sixth International Planetary Probe Workshop*, 2008.

[11] B. S. Baldwin and H. Lomax. Thin layer approximation and algebraic model for separated turbulent flows. In *AIAA Paper 78-257*, January 1978.

[12] Robin Beck. Ablative thermal protection systems fundamentals. In *International Planetary Probe Workshop 10*, San Jose, California, June 15-16 2013.

[13] D. Bernardi, V. Colombo, E. Ghedini, and A. Mentrelli. Three-dimensional modelling of inductively coupled plasma torches. *The Europen Physical Journal D*, 22(1):119–125, 2003.

[14] Daniele Bianchi. *Modeling of ablation phenomena in space applications*. PhD thesis, Universit'a degli Studi di Roma, 2006/2007.

[15] Bernard Bienstock, David Atkinson, Kevin Baines, Paul Mahaffy, Paul Steffes, Sushil Atreya, Alan Stern, Michael Wright, Harvey Willenberg, David Smith, Robert Frampton, Steve Sichi, Leora Peltz, James Masciarelli, and Jeffrey Van Cleve. Neptune polar orbiter with probes. In *2nd INTERNATIONAL PLANETARY PROBE WORKSHOP*, USA, August 2004.

[16] N. J. Bisek. *Numerical Study of Plasma-Assisted Aerodynamic Control for Hypersonic Vehicles*. PhD thesis, University of Michigan, Ann Arbor, Michigan,, 2010.

[17] B. Blackwell and R. Hogan. Numerical solution of axisymmetric heat conduction problems using finite control volume technique. In *Journal of Thermophysics and Heat Transfer*, volume 7, No. 3, pages 462–471, 1993.

[18] F. G. Blottner, M. Johnson, and M. Ellis. Chemically reacting viscous flow program for multi-component gas mixtures. In *Sc-rr-70-754*, Albuquerque, New Mexico, 1971. Sandia Laboratories.

[19] Deepak Bose and Michael Wright. Uncertainty analysis of laminar aeroheating predictions for mars entries. In *AIAA Paper 2005-4682*, June 2005.

[20] A. Bourdon and A. Bultel. Numerical simulation of stagnation line nonequilibrium airflows for reentry applications. *Journal of Thermophysics and Heat Transfer*, 22(2):168–177, April-June 2008.

[21] Iain D. Boyd. Rotational–translational energy transfer in rarefied nonequilibrium flows. In *The Physics of Fluids*, volume 2 (3), March 1990.

[22] F.M. Cheatwood and P.A. Gnoffo. *Users Manual for the Langley Aerothermal Upwind Relaxation Algorithm (LAURA)*. NASA TM-4674, April 1996.

[23] R.K. Clark, J. Cunnington, G. R., and K.E. Wiedemann. Determination of the recombination efficiency of thermal control coatings for hypersonic vehicles. *Journal of Spacecraft and Rockets*, 32(1):89–96, 1995.

[24] V. Colombo, E. Ghedini, and P. Sanibondi. Two-temperature thermodynamic and transport properties of argon-hydrogen and nitrogen-hydrogen plasmas. *J. Phys. D: Appl. Phys.*, 42, 2009, 055213.

[25] V. Colombo, E. Ghedini, and P. Sanibondi. A three-dimensional investigation of the effects of excitation frequency and sheath gas mixing in an atmospheric-pressure inductively-coupled plasma system. *J. Phys. D: Appl. Phys.*, 43, 2010, 105202.

[26] Vittorio Colombo. *personal communication.* Mechanical Engineering, University of Bologna, Bologna, Italy.

[27] Joseph L. Conley and Keith Hoppe Peterson. What are the origins of thermal protection systems? Oral/Visual Presentation ARC-E-DAA-TN3383, 2011.

[28] Gerard Degrez, David Vanden Abeele, Paolo Barbante, and Benot Bottin. Numerical simulation of inductively coupled plasma flows under chemical nonequilibrium. *International Journal of Numerical Methods for Heat and Fluid Flow*, 14(4):538–558, 2004.

[29] Prasun N. Desai, Dan T. Lyons, Jeff Tooley, and Julie Kangas. Entry, descent, and landing operations analysis for the stardust re-entry capsule. In *AIAA-2006-6410*, 2006.

[30] T. R. Deschenes. *Extension of a Modular Particle-Continuum Method for Nonequilibrium, Hypersonic Flows.* PhD thesis, University of Michigan, Ann Arbor, Michigan, 2011.

[31] O. Deutschmann, U. Riedel, and J. Warnatz. Modeling of nitrogen and oxygen recombination on partial catalytic surfaces. *Journal of Heat Transfer*, 117, May 1995.

[32] David M. Driver and Mathew MacLean. Improved predictions of pica recession in arc jet shear tests. In *AIAA Paper 2011-141*, January 2011.

[33] David M. Driver, Michael W. Olson, Michael D. Barnhardt, and Matthew MacLean. Understanding high recession rates of carbon ablators seen in shear tests in an arc jet. In *48th AIAA Aerospace Sciences Meeting*, AIAA 2010-1177, 4-7 January 2010.

[34] Karl T. Edquist, Artem A. Dyakonov, Michael J. Wright, and Chun Y. Tang. Aerothermodynamic environments definition for the mars science laboratory entry capsule. In *AIAA 2007-1206*, Reno, Nevada, January 2007.

[35] F De Filippis, A Del Vecchio, A Martucci, and et al. 70mw plasma wind tunnel up-grades for esa aurora tps testing. In *4th International Planetary Probe Workshop*, Pasadena, California, USA, June 2006.

[36] Douglas G. Fletcher. Measurement requirements for improved modeling of arcjet facility flows. In *RTO AVT Course on "Measurement Techniques for High Enthalpy and Plasma Flows"*, Belgium, October 25-29 1999.

[37] Peter A. Gnoffo. Planetary-entry gas dynamics. volume 31, pages 459–94, 1999.

[38] Peter A. Gnoffo, K. James Weilmuenster, H. Harris Hamilton, David R. Olynick, and Ethiraj Venkatapathy. Computational aerothermodynamic design issues for hypersonic vehicles. In *AIAA Paper 97-2473*, 1997.

[39] C. Godart, M. V. Salvetti, and J. A. Désidéri. Computation of catalycity effects in hypersonic non-equilibrium flows, 2007.

[40] A. N. Gordeev, A. F. Kolesnikov, and M. I. Yakushin. Effect of surface catalytic activity on nonequilibrium heat transfer in a subsonic jet of dissociated nitrogen. *Fluid Dynamics*, 20:478–484, 1985.

[41] Michael D. Griffin and James R. French. *Space Vehicle Design*. Number ISBN-13: 978-1563475399. AIAA Education Series, 2 edition.

[42] Jay H. Grinstead, David A. Stewart, , and Charles A. Smith. High enthalpy test methodologies for thermal protection systems development at nasa ames research center. In *AIAA 2005-3326*, 2005.

[43] Ali Gülhan. Heat flux measurements in high enthalpy flows. In *RTO EN-8*, Belgium, October 1999.

[44] R.N. Gupta, J.M. Yos, R.A. Thompson, and K.P. Lee. A review of reaction rates and thermodynamic and transport properties for an 11-species air model for chemical and thermal nonequilibrium calculations to 30,000k. volume NASA-RP-1232, 1990.

[45] Gale A. Harvey. *SIMULATED REENTRY HEATING BY TORCHING*. NASA Langley Research Center.

[46] Sylvia M. Johnson. Approach to tps development for hypersonic applications at nasa ames research center. In *Proceedings 5th European Workshop on Thermal Protection Systems and Hot Structures*, Noordwijk, The Netherlands, 17 - 19 May 2006 2006.

[47] M. Kardell. Boeing lcat facility arc-jet testing of materials for hypersonic and space applications. In *Arc-Jet Technology Workshop*. Rice University, July 16-20 2007.

[48] G. Karypis and V. Kumar. Metis: A software package for partitioning unstructured graphs, partitioning meshes, and computing fill-reducing orderings of sparse matrices. *University of Minnesota*, 1998.

[49] A. F. Kolesnikov. Extrapolation from high enthalpy tests to flight based on the concept of local heat transfer simulation. pages 8B/1–14, Neuilly-sur-Seine Cedex, France, 1999. NATO RTO EN-8.

[50] B. Laub and E. Venkatapathy. Thermal protection system technology and facility needs for demanding future planetary missions. In *International Workshop on Planetary Probe Atmospheric Entry and Descent Trajectory Analysis and Science*, October 2003.

[51] A. Lutz, J. Meyers, W. Owens, S. Smith, and D. G. Fletcher. Experimental analysis of carbon nitridation and oxidation efficiency with laser-induced fluorescence. In *51st AIAA Aerospace Sciences Meeting*, number AIAA 2013-0924, Grapevine, Texas, 07-10 January 2013.

[52] A. Lutz, W. Owens, J. Meyers, D.G. Fletcher, and J. Marschall. Investigation of cn production from carbon materials in nitrogen plasmas. In *AIAA Paper 2011-901*, January 2011.

[53] A. Lutz, W. Owens, J. Meyers, D.G. Fletcher, and J. Marschall. Investigation of cn production from carbon materials in nitrogen plasmas. In *AIAA Paper 2011-901*, January 2011.

[54] Andrew J. Lutz. *personal communication*. Mechanical Engineering, University of Vermont, Burlington,VT.

[55] Andrew J. Lutz. Investigation of cn production from carbon materials in nitrogen plasmas. Master's thesis, The University of Vermont, October 2011.

[56] R.W. MacCormack and G.V. Candler. The solution of the navier-stokes equations using gauss-siedel line relaxation. In *Computers and Fluids*, volume 17, pages 135–150, 1989.

[57] Matthew MacLean, Jochen Marschall, and D. M. Driver. Finite-rate surface chemistry model, ii: Coupling to viscous navier-stokes code. In *AIAA Paper 2011-3784*, June 2011.

[58] C. Madden and R Lewis. Jsc arc-jet capabilities envelopes. In *Arc-Jet Technology Workshop*. Rice University, July 2007.

[59] J. Marschall, R.A. Copeland, H.H. Hwang, and M.J. Wright. Surface catalysis experiments on metal surfaces in oxygen and carbon monoxide mixtures. In *AIAA Paper 2006-181*, January 2006.

[60] Jochen Marschall and Douglas G. Fletcher. High-enthalpy test environments, flow modeling and in situ diagnostics for characterizing ultra-high temperature ceramics. *Journal of the European Ceramic Society*, 30(11):2323–2336, 2010.

[61] Jochen Marschall and Matthew MacLean. Finite-rate surface chemistry model, i: Formulation and reaction system examples. In *AIAA Paper 2011-3783*, June 2011.

[62] A. Martin and I. D. Boyd. Implicit implementation of material response and moving meshes for hypersonic re-entry ablation. In *AIAA Paper 2009-670*, January 2009.

[63] A. Martin and I. D. Boyd. Strongly coupled computation of material response and nonequilibrium flow for hyper- sonic ablation. In *AIAA Paper 2009-3597*, June 2009.

[64] A. Martin and I. D. Boyd. Cfd implementation of a novel carbon-phenolic-in-air chemistry model for atmospheric re-entry. In *AIAA Paper 2011-143*, January 2011.

[65] A. Martin, L.C. Scalabrin, and I.D. Boyd. High performance modeling of atmospheric re-entry vehicles. *Journal of Physics: Conference Series*, 341, 2012, Article 012002.

[66] Bonnie J. McBride and Sanford Gordon. Chemical equilibrium with applications (cea). [http://www.grc.nasa.gov/WWW/CEAWeb/], accessed in 2011.

[67] Frank S. Milos and Daniel J. Rasky. Review of numerical procedures for computational surface thermochemistry. *JOURNAL OF THERMOPHYSICS AND HEAT TRANSFER*, 8(1), January-March 1994.

[68] R.A Mitcheltree. Computational aerothermodynamics for mars pathfinder including turbulence. In *AIAA Paper No. 95-3493*, August 1995.

[69] R. Motion. Returning from space: Re-entry.

[70] Anuscheh Nawaz, David Driver, and Imelda Terrazas Salinas. Surface catalysis and oxidation on stagnation point heat flux measurements in high enthalpy arc jets. In *AIAA Thermophysics Conference*, San Diego, CA, 24-27 Jun 2013.

[71] W. P. Owens, J. Uhl, M. Dougherty, A. Lutz, Jason Meyers, and D. G. Fletcher. Development of a 30kw inductively coupled plasma torch for aerospace material testing. In *AIAA Paper 2010-4322*, June 2010.

[72] Walt Owens. *personal communication*. Mechanical Engineering, University of Vermont, Burlington,VT.

[73] Walten Owens. Development of a 30kw inductively-coupled plasma torch for high temperature aerospace material testing at uvm. Master's thesis, The University of Vermont, 2011.

[74] Chul Park and David W. Bogdanoff. Shock-tube measurement of nitridation coefficient of solid carbon. *Journal of Thermophysics and Heat Transfer*, 20(3), July-September 2006.

[75] J. G. Parker. Rotational and vibrational relaxation in diatomic gases. In *The Physics of Fluids*, volume 2 (4), pages 449–462, July-August 1959.

[76] J.V. Rakich, D.A. Stewart, , and M.J. Lanfranco. Results of a flight experiment on the catalytic efficiency of the space shuttle heat shield. In *AIAA Paper 82-0944*, 1982.

[77] J. William Rich, Sergey O. Macheret, and Igor V. Adamovich. Aerothermodynamics of vibrationally nonequilibrium gases. In *Experimental Thermal and Fluid Science*, volume 13, 1996.

[78] David H. Rudy and John C. Strikwerda. Boundary conditions for subsonic compressible navier-stokes calculations. *Computers and Fluids*, 9:327–338, 1981.

[79] John M. Sankovic and Francis M. Curran. Arcjet thermal characteristics. In *AIAA- 91 -2456*, Sacramento, CA, June 24-27 1991.

[80] G.S.R. Sarma. Physio-chemical modelling in hypersonic flow simulation. *Progress in Aerospace Sciences*, 36:281–349, 2000.

[81] L. C. Scalabrin. *Numerical Simulation of Weakly Ionized Hypersonic Flow over Reentry Capsules*. PhD thesis, University of Michigan, Ann Arbor, Michigan, 2007.

[82] L. C. Scalabrin and I. D. Boyd. Numerical simulation of weakly ionized hypersonic flow for reentry configurations. In *AIAA Paper 2006-3773*, June 2006.

[83] L. C. Scalabrin and I. D. Boyd. Numerical simulations of the fire-ii convective and radiative heating rates. In *AIAA Paper 2007-4044*, June 2007.

[84] C. D. Scott. Wall catalytic recombination and boundary conditions in nonequilibrium hypersonic flow - with applications. In *The Third Joint Europe/US Short Course in Hypersonic Flow*, October 1990.

[85] S. Sepka, Y. K. Chen, J. Marschall, and R.A. Copeland. Experimental investigation of surface reactions in carbon monoxide and oxygen mixtures. *Journal of Thermophysics and Heat Transfer*, 14(1):45–52, 2000.

[86] R. G. Sheppard, D. M. Mathes, and D. J. Bray. *Properties and Characteristics of Graphite*. Poco Graphite, Inc., November 2001.

[87] D.M. Smith. Aedc arc jet facility capabilities and test environments. In *Arc-Jet Technology Workshop*. Rice University, July 26-28 2005.

[88] R. Smith, D. Wagner, and James Cunningham. A survey of current and future plasma arc-heated test facilities for aerospace and commercial applications. In *AIAA Paper No. 98-0146*, 1998.

[89] D.A. Stewart. Determination of surface catalytic efficiency for thermal protection materials - room temperature to their upper use limit. In *AIAA Paper 96-1863*, June 1996.

[90] D.A. Stewart. Surface catalytic efficiency of advanced carbon carbon candidate thermal protection materials for ssto vehicles. In *NASA TM-110383*, February 1996.

[91] D.A. Stewart. Surface catalysis and characterization of proposed candidate tps for access-to-space vehicles. In *NASA TM-112206*, July 1997.

[92] D.A. Stewart, Y. K. Chen, D.J. Bamford, and A.B Romanovsky. Predicting material surface catalytic efficiency using arc-jet tests. In *AIAA Paper 1995-2013*, June 1995.

[93] D.A. Stewart, J.V. Rakich, and Y.K. Chen. Flight experiment demonstrating the effect of surface catalysis on the heating distribution over the space shuttle heat shield. In *NASA CP-3248, NASA CP 3248*, Williamsburg, VA, 1995.

[94] K. Sutton and P.A.Gnoffo. Multi component diffusion with application to computational aerothermodynamics. *AIAA Paper 1998-2575*, 1998.

[95] Toshiyuki Suzuki and Kazuhisa Fujita. Experimental study of graphite ablation in nitrogen flow. *JOURNAL OF THERMOPHYSICS AND HEAT TRANSFER*, 22(3), July-September 2008.

[96] Toshiyuki Suzuki and Kazuhisa Fujita. Experimental study of graphite ablation in nitrogen flow, part ii: Further numerical analysis. *JOURNAL OF THERMOPHYSICS AND HEAT TRANSFER*, 24(3), July-September 2010.

[97] Toshiyuki Suzuki and Kazuhisa Fujita. Graphite nitridation in lower surface temperature regime. *JOURNAL OF THERMOPHYSICS AND HEAT TRANSFER*, 24(1), January-March 2010.

[98] T.D.Holman and I.D.Boyd. Numerical investigation of the effects of continuum breakdown on hypersonic vehicle surface properties. In *AIAA Paper 2008-3928*, June 2008.

[99] I. Terrazas-Salinas and C. Cornelison. Test planning guide for asf facilities. In *NASA/ARC Thermophysics Facilities Branch, A029-9701-XM3 Rev B*, March 1999.

[100] Kerry A. Trumble, Ioana Cozmuta, Steve Sepka, Peter Jenniskens, and Michael Winter. Postflight aerothermal analysis of stardust sample return capsule. *JOURNAL OF SPACECRAFT AND ROCKETS*, 47(5), September–October 2010.

[101] E. Venkatapathy, B. Laub, G.J. Hartman, J.O. Arnold, M.J. Wright, and G.A. Allen Jr. Thermal protection system development, testing, and qualification for atmospheric probes and sample return missions examples for saturn, titan and stardust-type sample return. *Advances in Space Research*, 44:138–150, 2009.

[102] Ethiraj Venkatapathy. Modern advances in ablative tps. In *International Planetary Probe Workshop 10*, San Jose, California, June 15-16 2013.

[103] W. G. Vincenti and C. H. Kruger. *Introduction to Physical Gas Dynamics.* Krieger Publishing Company, 2002.

[104] F. M. White. *Viscous Fluid Flow, McGraw-Hill, 3rd ed., 2006.*

[105] Jonathan E. Wiebenga and Iain D. Boyd. Computation of multi-dimensional material response coupled to hypersonic flow. In *43rd AIAA Thermophysics Conference*, number AIAA 2012-2873, New Orleans, Louisiana, 25 - 28 June 2012 2012.

[106] C. R. Wilke. A viscosity equation for gas mixtures, 1950.

[107] Michael J. Wright, Jay H. Grinstead, and Deepak Bose. A risk-based approach for aerothermal/ tps analysis and testing. In *Experiment, Experiment, Modeling and Simulation of Gas-Surface Interactions for Reactive Flows in Hypersonic Flights*, volume RTO-EN-AVT-142, 2007.

[108] Michael J. Wright, Chun Y. Tang, Karl T. Edquist, Brian R. Hollis, Paul Krasa, and Charles A. Campbell. A review of aerothermal modeling for mars entry missions. In *AIAA 2010-443*, 2010.

[109] M.J. Wright, G.V. Candler, , and D. Bose. Data-parallel line relaxation method for the navier-stokes equations. *AIAA Journal*, 36(9):1603–1609., 1998.